Modelling of Flowability Measurement of Cohesive Powders Using Small Quantities

By

Massih Pasha

Submitted in accordance with the requirements for the degree of

Doctor of Philosophy

The University of Leeds

School of Process, Environmental and Materials Engineering

February 2013

The candidate confirms that the work submitted is his own, except where work which has formed part of jointly authored publications has been included. The contribution of the candidate and the other authors to this work has been explicitly indicated below. The candidate confirms that appropriate credit has been given within the thesis where reference has been made to the work of others.

This copy has been supplied on the understanding that it is copyright material and that no quotation from the thesis may be published without proper acknowledgment.

© 2013 The University of Leeds and Massih Pasha

Chapter 5 of this thesis has already been published in Powder Technology (Pasha *et al.* 2013). The analyses, discussions and conclusions were all done by Massih Pasha. Other authors of this publication provided feedback and guidance.

M. Pasha, C. Hare, A. Hassanpour, and M. Ghadiri, "Analysis of ball indentation on cohesive powder beds using distinct element modelling", Powder Technology, vol. 233, pp. 80-90, 2013.

Acknowledgments

While working on this work I have benefited from the support and help of many people, few of whom I would like to thank here.

First and foremost I should express my highest degree of appreciation to my project supervisors Professor Mojtaba Ghadiri and Dr Ali Hassanpour whose insights, enthusiasm and constant unconditional support were key to my success.

The financial support from the Engineering and Physical Science Research Council (EPSRC), National Nuclear Laboratory (NNL) and Sellafield Ltd is gratefully appreciated. I would like to acknowledge the support and constructive comments from Dr Terry Semeraz of NNL and Dr Robert Stephen of Sellafield Ltd. I am also thankful to Mr Umair Zafar and Dr Colin Hare for sharing thoughts and invaluable assistance. Dr Colin Hare's effort and time on proof reading this thesis are greatly appreciated. I would like to convey thanks to Dr Afsheen Zarrebini for sharing 9 years of student life with me and introducing me to the research group. I also would like to thank my colleagues and friends, Dr Hossein Ahmadian, Dr Graham Calvert, Mr Selasi Dogbe and Miss Nadia Haerizadeh-Yazdi for their support and encouragement.

Last but by no means least, I would like to convey an immeasurable amount of gratitude to my dearest parents, Mrs Alam Zarrehbini and Mr Ahmadgholi Pasha, and to my sister and brother, Miss Leila Pasha and Mr Mehrdad Pasha, for their unconditional love and support throughout the numerous ups and downs of my life.

To My Dear Parents

Abstract

The characterisation of cohesive powders for flowability is often required for reliable design and consistent operation of powder processes. This is commonly achieved by the unconfined compression test or shear test, but these techniques require a relatively large amount of powder and are limited to large pre-consolidation loads. There are a number of industrial cases where these tests are not applicable because small amounts of powders have to be handled and processed, such as filling and dosing of small quantities of powder in capsules and dispersion in dry powder inhalers. In other cases, the availability of testing powders could be a limiting issue. It has been shown by Hassanpour and Ghadiri (2007) that under certain circumstances, indentation on a cohesive powder bed by a blunt indenter can give a measure of the resistance to powder flow, which is related to flowability. However, the specification of the operation window in terms of sample size, penetration depth, indenter properties and strain rate has yet to be fully analysed. In the present work, the ball indentation process is analysed by numerical simulations using the Distinct Element Method (DEM). The flow resistance of the assembly, commonly termed hardness, is evaluated for a range of sample quantities and operation variables. It is shown that a minimum bed height of 20 particle diameters is required in order to achieve reliable measurements of hardness. A sensitivity analysis of indenter size reveals that small indenters with diameters less than 16 times the particle diameter exhibit fluctuations in powder flow stress measurements, which do not represent shear deformation. The penetration depth should be sufficiently large to cause notable bed shear deformation. It is found that this minimum penetration depth is approximately equal to 10% of the indenter radius. The hardness measurements are found to be independent of indenter stiffness within the wide range investigated.

The friction between the indenter and the particles slightly increases the hardness, although its influence on the internal stresses is negligible. Cubic and cylindrical indenters measure significantly larger hardness value compared to the spherical indenter. Increasing the inter-particle friction and cohesion results in higher hardness values and internal stresses, due to the increase in resistance to shear deformation. Simulations at a range of indenter velocities confirm that the ball indentation technique can be used to analyse powder flowability over a wide range of shear rates.

Contents

List of Figures

List of Tables

Nomenclature

Latin Characters

A	Contact radius	m
α_0	Plastic contact deformation	m
a_c	Contact radius at JKR pull-off force	m
a_e	Elastic component of contact radius	m
a_{ep}	Elasto-plastic contact radius	m
a_p	Plastic component of contact radius	m
A_p	Plastic deformation contact area	m
A_R	Hamaker constant	J
a_y	Contact radius at yielding	m
C	ratio of effective Young's modulus to contact yield pressure, Cohesion	-, Pa
C_a	Fitted parameter in Vu-Quoc and Zhang model	m/N
d	Indenter diameter, Separation distance	m
d_b	Bed diameter	m
d_p	Mean particle diameter	m
e	Coefficient of restitution	-
E^*	Equivalent Young's modulus	Pa
E_i	Impact kinetic energy	J

E_r	Rebound kinetic energy	J
f_c	Pull-off force	N
f_{ce}	Elastic JKR pull-off force	N
f_{cp}	Pull-off force after plastic deformation	N
F_c	Contact force	N
ff_c	Flow function	-
F_g	Gravitational force	nN
F_{Hertz}	Hertz elastic force	N
F_{LB}	Liquid bridge force	N
F_{max}	Maximum contact force, maximum indentation load	N
$F_{\max}^{*}$	JKR equivalent maximum contact force	N
F_n	Normal contact force	N
F_{nc}	Non-contact force	N
F_s	Shear force	N
F_{s_pre}	Previous shear force	N
ff_ρ	Density-weighed flowability	-
F_t	Tangential contact force	N
f_{t0}	previous tangential force	N
f_t^{TP}	Tangential force at the turning point	N
f_t^{TTP}	Tangential force at the second turning point	N
F_{tc}	Critical tangential force	N

F_{t_elec}	Coulomb force	N
F_{van}	Van der Waals force	N
F_y	Yield force	N
g	Gravitational acceleration	m/s^2
G	Shear modulus	Pa
G^*	Equivalent shear modulus	Pa
h	Penetration depth	m
h_b	Bed height	m
h_d	Dimensionless penetration	-
I	Moment of inertia	$kg.m^2$
K_c	Fitted parameter in Vu-Quoc and Zhang model	N^{-1}
k_c	Cohesive stiffness	N/m
k_{cp}	Plastic-cohesive stiffness	N/m
k^*_{crit}	Largest equivalent stiffness in the system	N/m
k_e	elastic stiffness	N/m
$\hat{k}_e$	maximum value of the elastic stiffness	N/m
k_n	Normal contact stiffness	N/m
k_p	plastic stiffness	N/m
k_s	Shear contact stiffness	N/m
k_t	Tangential contact stiffness	N/m
k_{tM}	tangential stiffness of Mindlin no-slip model	N/m

m	Mass	kg
M	Torque	N.m
m^*	Equivalent mass	kg
M_i	Mass of indentation	kg
N_p	Number of particles	-
N_c	Number of contacts	-
n_i	normal vector from a particle centroid to its contact	-
p_{vdW}	van der Waals pressure	Pa
p_y	yield pressure	Pa
Q	Electric charge	C
Q_m	Mass flow rate	kg/s
Q_v	Volume flow rate	m^3/s
r	Indenter radius	m
R	Particle radius	m
R^*	Equivalent radius	m
r_b	Radius of the projected area of impression	m
R_p^*	Equivalent radius after permanent deformation	m
t_{crit}	Critical time-step for a mass-spring system	s
T_R	Rayleigh time-step	s
V	Velocity	m/s
v_a	Vibration acceleration	m/s^2

v_i	Impact velocity	m/s
V_i	Volume of the impression	m^3
v_r	Rebound velocity	m/s
W_e	Elastic work	J
W_p	Plastic work	J
W_{lt}	Loading tensile work	J
W_{ut}	Unloading tensile work	J
x_i^p	*i*-components of particle centre	m
x_i^c	*i*-components of contact location	m
z_0	equilibrium separation	m

Greek Characters

α^*	plastic flow limit overlap	m
α_0	Overlap at zero contact force	m
α_{cp}	Overlap at pull-off force after plastic deformation	m
α_f	Contact breakage overlap of JKR model	m
α_{fluid}	stress-free fluid overlap	m
α_{fe}	Elastic contact detachment overlap	m
α_{fp}	Plastic contact detachment overlap	m
α_n	Normal contact overlap	m

α_p	Plastic deformation overlap	m
α_{pd}	Plastic deformation	m
α_s	Tangential contact overlap	m
α_t	Tangential contact overlap	m
α_y	Yield normal overlap	m
β	Viscous damping coefficient	N.s/m
γ	Surface tension of liquid, Strain rate	N/m
γ^*	Dimensionless strain rate	-
Γ	Interface energy	J/m^2
ΔF_s	Increment of tangential force	m
Δp	Pressure drop	Pa
ΔV	Potential difference	V
ε_0	Permittivity of vacuum	F/m
κ	elastic-plastic contact consolidation coefficient	-
κ_A	elastic-plastic contact area coefficient	-
κ_p	plastic repulsion coefficient	-
μ	coefficient of sliding friction	-
ρ	Density	kg/m^3
ρ_b	Bulk density	kg/m^3
σ_1	Major principal stress	Pa
σ_2	Minor principal stress	Pa

σ_c	Unconfined stress	Pa
σ_{ij}	*ij*-component of stress tensor	Pa
σ_H	Horizontal stress	Pa
σ_{hyd}	Hydrostatic stress	Pa
σ_{pre}	Pre-consolidation stress, pre-shear stress	Pa
σ_T	Uniaxial tensile strength	Pa
σ_V	Vertical stress	Pa
τ_D	Deviatoric stress	Pa
τ_{pre}	Pre-shear stress	Pa
υ	Poisson's ratio	-
υ_r	Normal relative velocity of two particles in contact	m/s
ϕ_f	dimensionless plasticity depth	-
ω	Angular velocity	rad/s

CHAPTER 1 Introduction

1.1 Powder flowability

In industrial processes such as blending, transfer, storage, feeding, compaction and fluidisation the reliable flow of powder plays an important role, since it can affect the quality of the final product or production rate. Poor flow leads to wastage, machinery maintenance problems and downtime, with associated costs. In discharge of cohesive powders from a storage silo, an arch or rathole may form which will result in blockage or non-uniform discharge of powders. In the case of fine powders, this may lead to uncontrollable flooding and fluidisation of powders in air. In blending of cohesive powders, the powder bed may not be dilated which in turn does not allow powders to migrate through the dilated bed and reduces the mixing efficiency and quality of the final product. This is contrary to free flowing blends which segregate easily during subsequent handling processes [1].

Powder flow is a complex and multidimensional behaviour which depends on many powder characteristics [2]. There are a number of test methods for evaluation of flow behaviour of powders, most of which require a relatively large amount of powder. Furthermore, the most common test method, i.e. the shear cell, measures flow properties of bulk powder at relatively large consolidation stresses. There are a number of industrial cases where small amounts of loosely compacted powders are handled and processed, such as filling and dosing of small quantities of powder in capsules and dispersion in dry powder inhalers. In other cases, the availability of testing powders

could be an issue. For instance, in nuclear and pharmaceutical industries, the amount of powder available for testing is limited due to ionising radiation risks for the former and cost of drug in its early development stage for the latter. Moreover, studies of bulk behaviour at high compression levels may not be representative of loosely compacted powders at a small scale [3]. This exposes the need for a testing method of flowability, which makes use of small amounts of testing material. Hassanpour and Ghadiri [4] proposed a testing method based on ball indentation on a powder bed which can be performed on small amounts of loosely compacted powders. The preliminary results correlated well with common test methods, such as the unconfined compression and shear cell testing, where a linear relationship between the hardness (flow stress) measured by ball indentation and the unconfined yield stress prevailed. However it was found that the ratio of hardness to unconfined yield stress, commonly defined as the constraint factor, depended on the material. In continuum mechanics, the constraint factor is well understood for solid materials such as metals, glasses and polymers. In their work, Hassanpour and Ghadiri [4] considered a constraint factor of 3 for all their testing materials as a first attempt, but this was later found not to be appropriate [5]. The extent of constraining depends on powder properties, such as adhesion, friction, shape, roughness, stiffness and hardness. However, the constraining of deformation in the indentation process in powder beds is complicated due to the discrete nature and degree of freedom of movement of the particles.

In a bed of particles under compression the particles are not uniformly loaded; this makes it difficult to determine internal stresses analytically. Moreover, measurement of

internal stresses and structure is not possible experimentally. The most appropriate approach for this purpose is the use of computer simulation by the Distinct Element Method (DEM).

In the present work, an attempt is made to investigate the criteria which define the minimum required sample quantity, the suitable indenter size range and strain rate dependency for the ball indentation test. To this end, sensitivity analyses have been performed by DEM simulation of the indentation process in order to study the localised stress/strain behaviour of powder around the indenter.

1.2 **Objectives and structure of the thesis**

The overall aim of this PhD is to further the understanding of the ball indentation method using numerical analysis by DEM. This work is part of an Engineering and Physical Sciences Research Council (EPSRC) project [6] which is summarised in Figure 1.1.

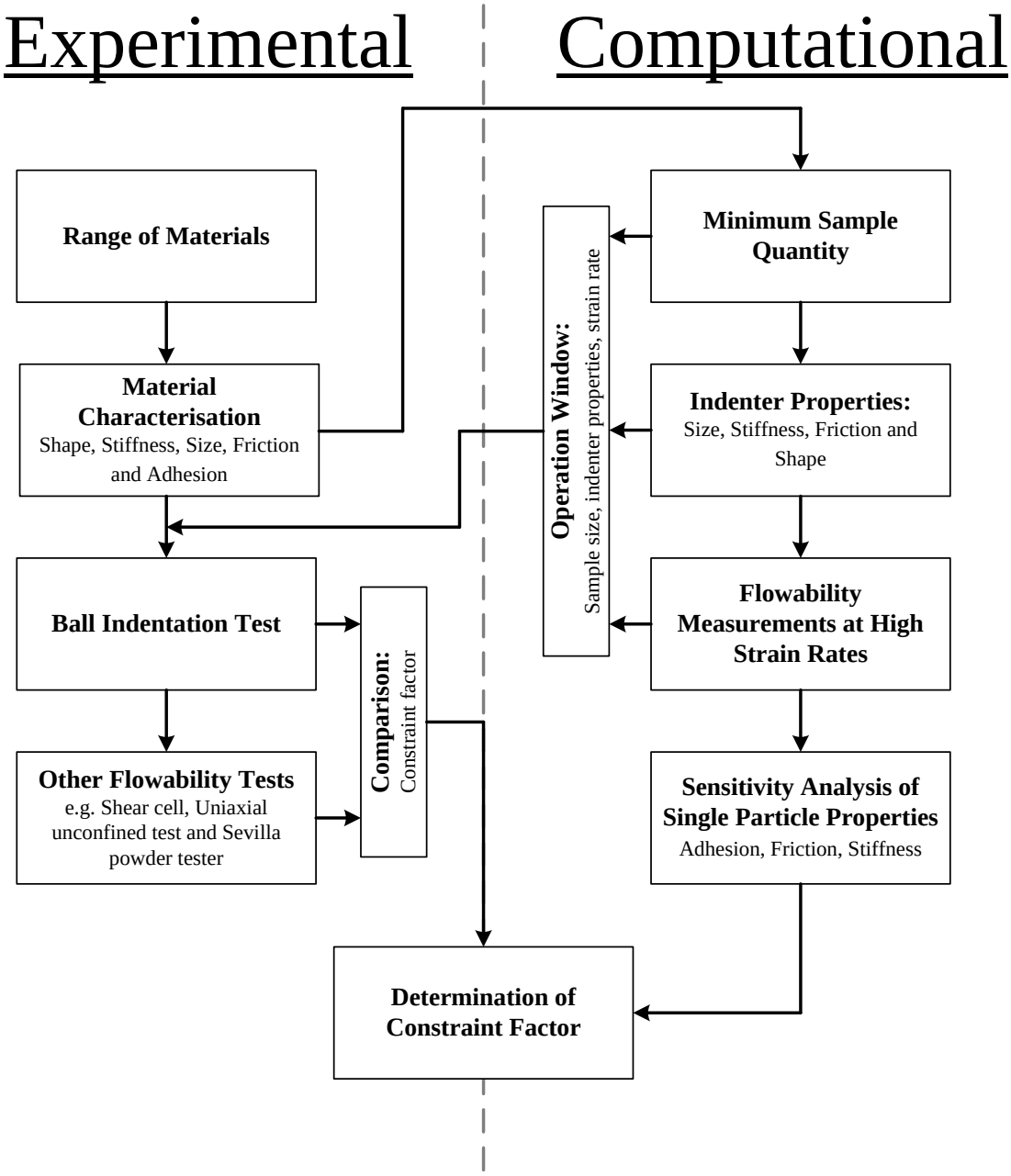

Figure 1.1: Schematic diagram of the project plan

The project consists of experimental and computational works. The experimental findings will be reported in Mr Umair Zafar's PhD thesis [7]. The DEM simulations that constitute this thesis investigate the operational window of the ball indentation method in terms of minimum required sample size, indenter properties (e.g. friction, shape,

stiffness and size) and the sensitivity of the measurements with strain rate, with an aim of determining the criteria to be followed for the experimental procedures. A wide range of materials are characterised and their flowability is determined by the ball indentation and other measurement methods. The findings of the various measurement methods are compared, with the intention of determining the constraint factor for various materials. Sensitivity of hardness and internal stresses during the indentation process with the single particle properties are also investigated by the DEM simulations, which is subsequently compared to the findings of the experimental work in order to develop the understanding of the indentation process and the constraint factor.

Chapter 2 briefly compares various commonly-used flowability measurement techniques. The concept of DEM is outlined in Chapter 3 with a focus on the contact models and incorporation of shape in the DEM simulations. Description of a new linear contact model, which was developed for DEM simulations of elasto-plastic and adhesive spheres, is given in Chapter 4. Chapters 5 and 6 investigate the operational window in the ball indentation method in terms of minimum sample size, penetration depth and indenter properties (such as size, shape, friction and stiffness) using DEM. The sensitivity of the ball indentation process to strain rate is investigated in Chapter 7. Finally a summary of the findings of the thesis, concluding remarks and possible future work is presented in Chapter 8.

CHAPTER 2 Flowability Measurement Techniques

A wide range of techniques are available for evaluating bulk powder flow. There are fundamental differences between various techniques and devices which may lead to a variation in the measured powder behaviour. There are a number of reviews available in the literature which compare various techniques [3, 8]. This chapter outlines briefly the commonly used and recently developed techniques for evaluation of flowability of powders. A comparison of the techniques is also given.

2.1 Uniaxial compression test

In uniaxial compression test, a hollow cylinder with a known cross-sectional area is filled with the test powder. Internal wall of the hollow cylinder is made of low friction material in order to reduce the effects of wall friction. The bulk solids are compressed vertically by an applied force, resulting in the consolidation stress σ_1. The more the volume of the bulk solid is reduced, the more compressible it is. Compressibility of powders can be a measure of their flow behaviour. With easy-flowing, dry and relatively large particles, the decrease in the volume of the bulk on compression is not very large and the bulk density will increase only slightly. With fine and moist bulk solid one will observe a clear increase in bulk density [3]. After unloading the hollow cylinder is removed. Subsequently, the consolidated cylindrical bulk solids specimen is loaded with an increasing vertical compressive stress until it fails. This failure stress is

called the compressive strength, cohesive strength, or unconfined yield strength and is denoted as σ_c. The uniaxial compression test procedure is shown in Figure 2.1.

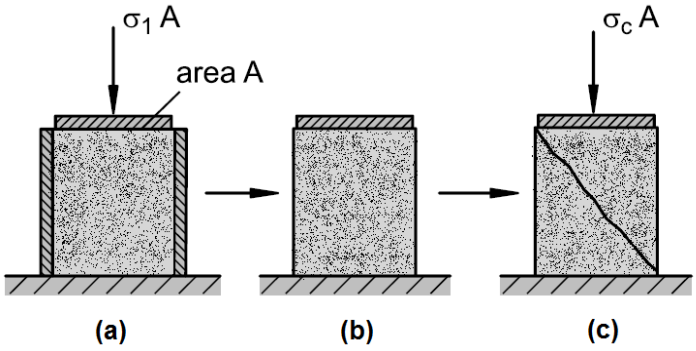

Figure 2.1: Uniaxial compression test procedure: (a) Consolidation; (b) Removal of walls and compression stress; (c) Failure of the bulk

Since the bulk solids fail only at a sufficiently large vertical stress there must be a material specific yield limit for the bulk solids. The yield limit of bulk solids is strongly dependent on its stress history i.e. previous consolidation. Generally for greater consolidation stresses, the bulk density and unconfined yield strength increase [8].

2.1.1 **Representation of stresses using Mohr's stress circles**

If the force of gravity acting on the bulk solids specimen is negligible and if no friction is acting between the wall of the hollow cylinder and the bulk solids, both vertical and horizontal stresses are constant within the entire bulk solid specimen [3]. The principal stresses are the normal stresses at the planes where there are no shear stresses acting. In the cases of zero wall friction, the vertical, σ_V, and horizontal, σ_H, stresses are the major and minor principal stresses, respectively, from which the Mohr circle for the consolidation can be drawn (Figure 2.2).

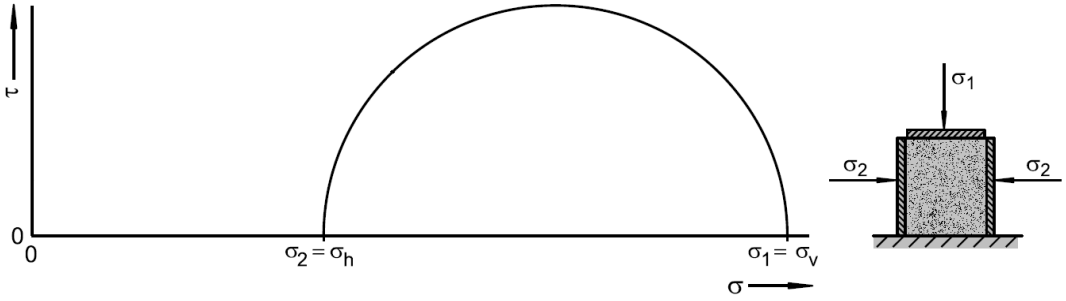

Figure 2.2: Mohr circle representation of consolidation process of uniaxial compression test

During unconfined compression, the minor principal stress (i.e. horizontal stress) is equal to zero due to the fact that the lateral surface of the specimen is unrestrained and not loaded. When the bulk fails, the unconfined yield strength acts vertically which is the major principal stress. The failure Mohr circle is shown in Figure 2.3.

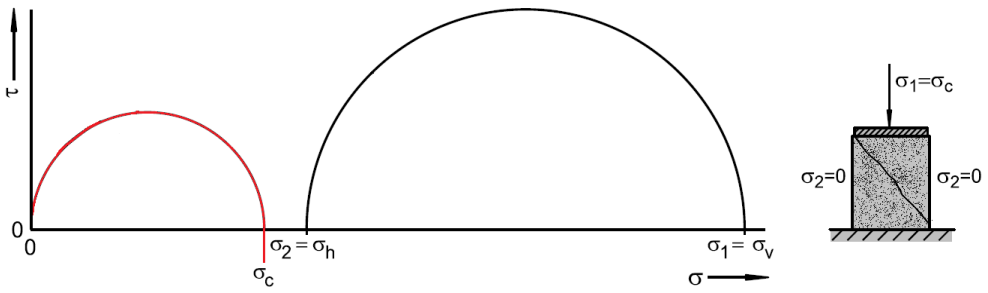

Figure 2.3: Mohr circle representation of uniaxial compression test

If a horizontal stress greater than zero ($\sigma_2 > 0$) was to be applied on the specimen (in addition to the vertical stress), the bulk powder would fail at a vertical stress which is larger than the one in the case of unconfined compression. The minor principal stress in

this case will be the constant horizontal stress. The Mohr circle representation of this case is shown in Figure 2.4.

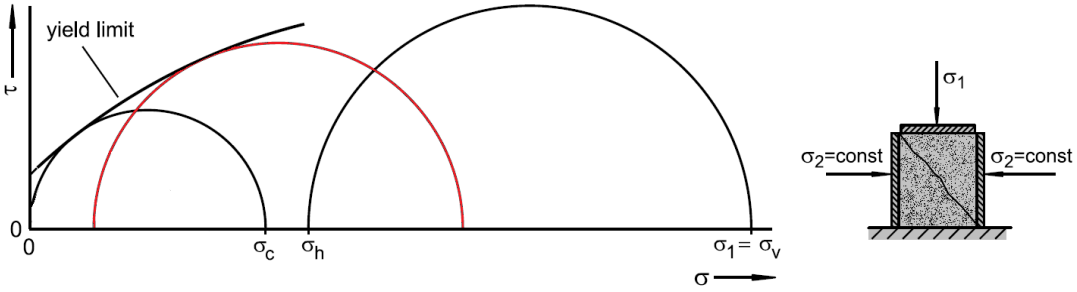

Figure 2.4: Mohr circle representation of biaxial compression test

The testing methods by which both the vertical and horizontal stresses are controllable are known as biaxial testers. The tangent line to all the possible failure Mohr circles for the same consolidation stress is known as the yield locus. This line gives a shear stress that is necessary to initiate flow for every normal stress. Stresses which lead to circles below the yield locus only cause an elastic deformation of the bulk solid specimen. Stress circles above the yield limit are not possible as the specimen would already be flowing when the Mohr stress circle reaches the yield limit. This failure continues without applying any larger load on the specimen [3].

2.1.2 **Classification of powders based on their flow behaviour**

Jenike [9] introduced a semi-empirical classification for flowability of bulk powders by means of a parameter called flow function, which is given by,

$$ff_c = \frac{\sigma_1}{\sigma_c} \tag{2.1}$$

where ff_c is the flow function, σ_1 is major principal stress and σ_c is the yield stress. Generally the larger the flow function is, the better a bulk solid flows. Jenike classified bulk solids flowability based on the value of ff_c. This classification is given in Table 2.1.

Table 2.1: Jenike's classification of powder flowability

ff_c	**Classification**
< 1	Not flowing
1-2	Very cohesive
2-4	Cohesive
4-10	Easy flowing
> 10	Free flowing

Flowability is the ratio of major principal stress corresponding to the applied load to unconfined yield strength, and this ratio becomes greater with increasing consolidation stress for most bulk solids. Therefore the consolidation stress at which the flowability is measured must also be given besides the value of ff_c. The consolidation stress selected for testing should reflect, as much as possible, the actual process conditions in which the flow problem occurs. For example in design of a hopper, it is important to consider the low consolidation stress ranges that are representative of the regions close to hopper apex, since arching mostly occurs around this region [8]. In many applications where the bulk solids flows by gravity such as storage bins or silos, two bulk solids with the same flowability value but a different bulk density will flow differently because a larger gravitational force acts on the bulk solids with the larger bulk density. In such cases that bulk density and gravitational forces affect the flow, the flowability value can be evaluated by Equation (2.2).

$$ff_\rho = ff_c \cdot \frac{\rho_b}{\rho_w} \tag{2.2}$$

where ff_ρ is called density-weighed flowability, ρ_b is the bulk density and ρ_w is the density of liquid water at 0℃ 1 bar. The bulk density is divided by the density of liquid water in order to obtain a dimensionless term [3].

2.2 **Shear testing**

The use of the uniaxial compression test may be problematic since very small unconfined yield strength values cannot be measured by this method. Moreover, preparation of the die to obtain low friction walls is a time-consuming and expensive procedure [3].

In shear testers (Figure 2.5), the bulk solids specimen of a known cross section area is subjected to a normal stress. Subsequently the top part of the tester is moved horizontally relative to the bottom which is fixed.

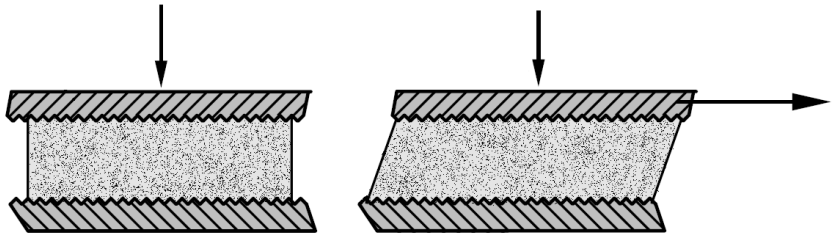

Figure 2.5: Schematic diagram of shear test procedure

Due to inter-particle and particle-wall friction, a shear stress is acting in the bulk solids which is transferred to the top and measured. Since the particles are relatively loosely packed at the beginning of shearing, particles can move against each other and rotate.

Inter-particle frictional forces will be small and thus the shear stress will be small at the beginning. With increasing shear deformation the bulk solids become increasingly compact, leading to increased frictional forces and bulk density. Finally the frictional forces between the particles are fully mobilised which causes plastic deformation of the bulk (known as steady-state flow). The steady-state flow transfers the bulk solids into a well-defined, reproducible state of bulk density and strength. The process of consolidation and shear to steady-state flow is called preshear and the shear stress at this point is called the preshear stress, τ_{pre}. The bulk density and the shear stress at the steady-state flow are characteristic for the applied normal stress. The preshear procedure corresponds to the consolidation step in the uniaxial compression test, however the required consolidation stress at preshear is precisely controlled, contrary to the uniaxial compression test in which the total vertical stress on the specimen is assumed to be equal to the consolidation stress. Moreover, in the case of inhomogeneous bulk solids specimens (e.g. when local voids or region with low bulk density exist throughout the specimen), the consolidation state of the bulk in the uniaxial compression test may not be representative of the whole bulk, especially at low consolidation stresses. This problem is avoided in a shear test; during preshear the inhomogeneities are compensated by the relatively large shear deformation [3].

After preshear, the normal stress acting on the specimen is reduced to a value less than the preshear normal stress. If the consolidated specimen is sheared (under the normal stress $\sigma_{sh} < \sigma_{pre}$), it will start to flow when a sufficiently large shear stress is achieved. At the failure of the specimen, the bulk density and shear resistance decrease which leads to a reducing shear stress. Therefore at the start of failure, a maximum shear stress

is achieved which characterises the incipient flow. The corresponding pair values of shear and normal stresses at the failure produce a point on shear vs. normal stress plot, which is known as a shear point. The process of preshear to steady-state flow and shear to failure is repeated for the same preshear stress but different normal stresses in the shear process. This results in a number of shear points on the shear vs. normal stress plot. A line containing all the possible shear points for a specific preshear stress is known as the yield locus, which is shown in Figure 2.6.

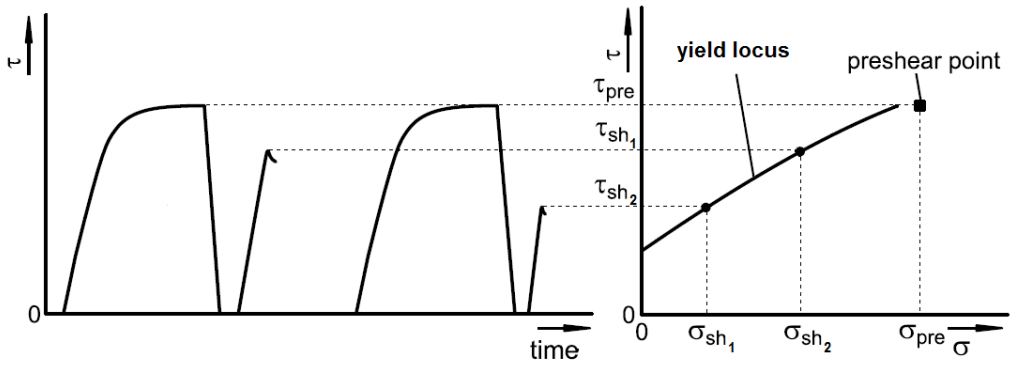

Figure 2.6: Determination of yield locus in a shear test

2.2.1 **Representation of stresses using Mohr's stress circles**

In order to evaluate the flowability of a bulk using a shear test, the major principal stress and unconfined yield strength must be determined. The major principal stress can be evaluated by drawing a Mohr's circle of steady-state flow. This Mohr's circle includes the preshear point and tangent to the yield locus. Considering the fact that the centre of the circle is on the σ-axis, the circle can be drawn (see Figure 2.7). The major principal stress is the largest of all normal stresses acting during steady-state flow in all possible

planes of the specimen (intercept of the circle with σ-axis). This stress is comparable to the consolidation stress of the uniaxial compression test (where σ_1 is also the largest normal stress) provided the walls are frictionless in the latter. The unconfined yield strength cannot be measured directly with a shear test and must be determined from the yield locus. At the failure, a normal stress and no shear stress act on the top of the specimen, and neither normal nor shear stresses act on the lateral surface of the specimen. The Mohr's circle representing the failure therefore has its minor principal stress at zero. Considering the fact that the centre of the circle is on the σ-axis, and that the circle is tangent to the yield locus, it can be drawn as shown in Figure 2.7. The unconfined yield stress is the intercept of this circle with σ–axis.

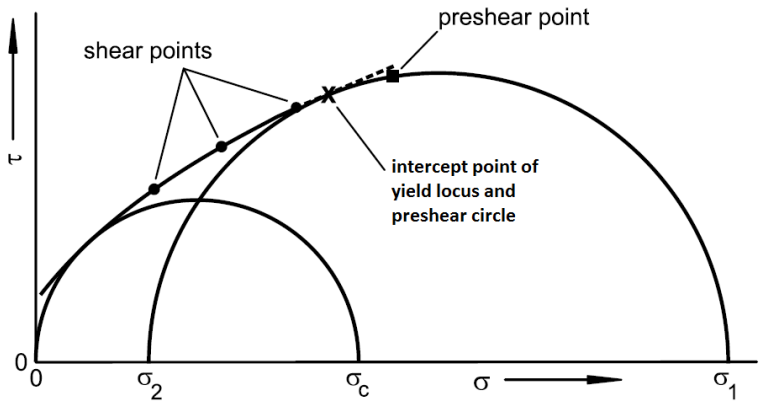

Figure 2.7: Mohr's circle representation of shear test

2.3 Flowability measurements at low consolidation stresses and tensile regimes

At low consolidation stresses as well as the region where the normal forces are tensile, it is important to determine two parameters, cohesion and uniaxial tensile strength (denoted as C and σ_T respectively). Cohesion is the value of shear stress where the yield locus intersects with the τ-axis, i.e. where normal stress is zero. Uniaxial tensile strength is the value of negative normal stress at which shear stress is zero, i.e. the left end of the yield locus.

2.3.1 Shear testers

With most shear testers it is not possible to measure shear points at very small or negative stresses because such stresses cannot easily be applied. In this case cohesion and tensile strength can be determined only by extrapolating the yield locus towards small and negative normal stresses [8]. Linearity is usually assumed for determination of yield loci for very small normal stresses. Mostly yield loci are increasingly curved towards small stresses, hence the value of the cohesion and tensile strength cannot be determined with confidence in this way. With a few shear testers such as Schulze shear ring tester [10] normal stresses of a few hundred Pascal can be measured. In this case, the extrapolated value of cohesion can be close to the actual value.

Once the cohesion is determined, the tensile strength can be evaluated based on the Warren Spring non-linear model [11], which is a predictive model for determination of

yield locus. The shear stress, τ, corresponding to the normal stress, σ, is calculated based on the following equation,

$$\left(\frac{\tau}{C}\right)^n = \frac{\sigma}{\sigma_T} + 1 \tag{2.3}$$

where C is the cohesion, σ_T is the tensile strength of the material and n is called the shear index of the bulk. Shear index is a material dependent parameter and varies between 1 and 2. It was found that shear index is not dependant on bulk density or consolidation stress of the bulk [11].

2.3.2 **Sevilla powder tester**

This apparatus requires a small volume of powder and measures the uniaxial tensile strength of the powder by applying a tensile force to a powder bed due to the pressure drop of a percolating gas. A general schematic diagram of this tester is shown in Figure 2.8.

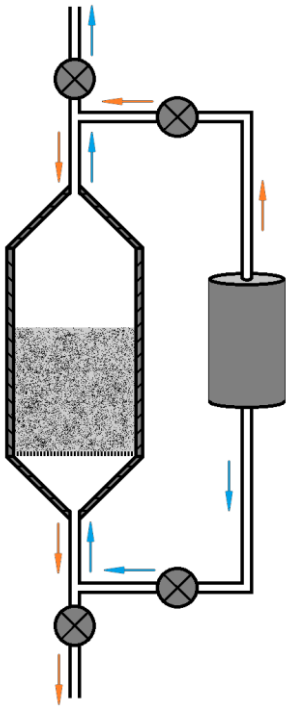

Figure 2.8: Sevilla powder tester

A bulk solids specimen is located inside a vertical cylindrical vessel and is supported on a porous plate which has pore sizes smaller than the particle size. A controlled flow of dry gas is introduced from the bottom of the specimen through the pores. The gas flow is increased until the powder bed is fluidised into a “freely bubbling regime”, through which the powder bulk looses its memory of stress history [12]. Once the specimen reaches a steady state, the gas flow is stopped and then reversed in order to apply a compressive load. This process corresponds to the preshear stage of a shear test and gives a reproducible starting condition for the bulk solid. In order to measure uniaxial tensile yield stress, the gas flow is yet again reversed to an upward-directed flow that is slowly increased to put the bed under increasing tension. The consolidation stress at the bottom of the bed is assumed to be the total weight of the sample divided by the cross-section area of the bed;

$$\sigma_c = \frac{m.g}{A} \tag{2.4}$$

where m is the total mass of the sample, g is the gravitational acceleration and A is the cross-section area of the bed. When the gas is passed through the particles, it exerts a drag force on the particles, causing a pressure drop and hence a tensile stress. Close observations reveal that fracture of the bed always starts at the bottom of the bed [12]. On increasing the gas flow rate, the tensile stress is increased until the point at which the bed fails. Therefore the normal stress acting on the particles at the bottom of the vessel can be calculated as follows,

$$\sigma_n = \frac{m.g}{A} - \Delta p \tag{2.5}$$

where Δp is pressure drop of the gas across the bed. With a constant and smooth increase of the gas flow rate, the pressure drop is increased linearly. With free flowing powders where there is no cohesion and yield locus originates from the origin (i.e. zero tensile strength and cohesion values), only gravitational forces should be overcome in order to initiate the incipient flow of the powders. The response of the pressure drop against increasing the gas flow for free flowing powders is shown schematically in Figure 2.9.

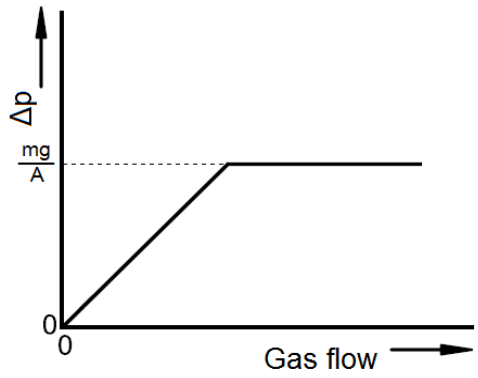

Figure 2.9: Schematic response of pressure drop against increasing gas flow for free flowing powders in Sevilla powder tester

In the case of cohesive powders, inter-particle adhesive forces need to be overcome in addition to the gravitational forces to initiate the incipient flow. Therefore a pressure drop larger than that corresponding to the weight of the bed (i.e. the free flowing case) is needed. The response of pressure of drop for cohesive powders is shown in Figure 2.10.

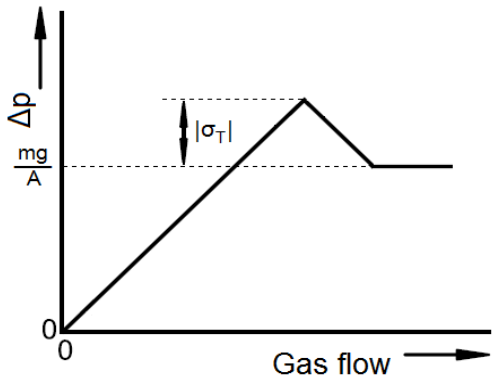

Figure 2.10: Schematic response of pressure drop against increasing gas flow for cohesive powders in the Sevilla powder tester

The overshoot of pressure drop beyond the bed weight per unit area when the powder fails gives a quantitative measure of the uniaxial tensile yield stress. In order to measure the tensile strength for different consolidation stresses, the powder is compressed by application of a downward-directed gas flow after the steady state of the powder is achieved (red arrows in Figure 2.8).

2.3.3 **Angle of repose**

In the angle of repose test, bulk solids are poured through a funnel which is located above a plate, forming a conical pile of loose and uncompacted bulk. In order to avoid the influence of the surface of the bottom plate, it is provided with a lip to retain a layer of bulk solid. The angle of repose is defined as the slope of the conical pile (Figure 2.11).

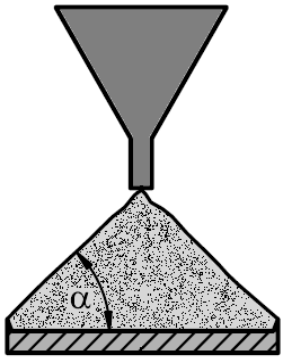

Figure 2.11: Angle of Repose

Carr [13] provided a classification of flow behaviour of powders based on their value of angle of repose. This classification is summarised in Table 2.2.

Table 2.2: Classification of powder flowability based on angle of repose

Angle of repose	Classification
< 30˚	Easy flowing
30˚- 45˚	Cohesive
45˚- 55˚	Very cohesive
> 55˚	Not flowing

Since bulk solids are falling from a height, the dynamics of the process may affect the results. There is no control on the consolidation stresses. With cohesive powders, heaps with a peaked tip can be observed which makes it difficult to determine the slope of the pile.

2.3.4 **Vibrating capillary method**

The apparatus [14] designed for this technique is illustrated in Figure 2.12. It consists of two tubes: a larger (in diameter) glass tube followed by a smaller (in diameter) capillary tube. The powder sample is fed to the glass tube by a hopper on the top which is kept full with powder during the measurements. The capillary tube is vibrated in the horizontal direction with a frequency and amplitude-controlled vibrator. The mass of particles discharged from the capillary for a given test is measured by a balance. The capillary tube diameter is small enough to prevent powder flow in the absence of vibration. The vibration amplitude is increased and the profile of mass flow rate as a function of vibration acceleration, which is called the flowability profile, is recorded.

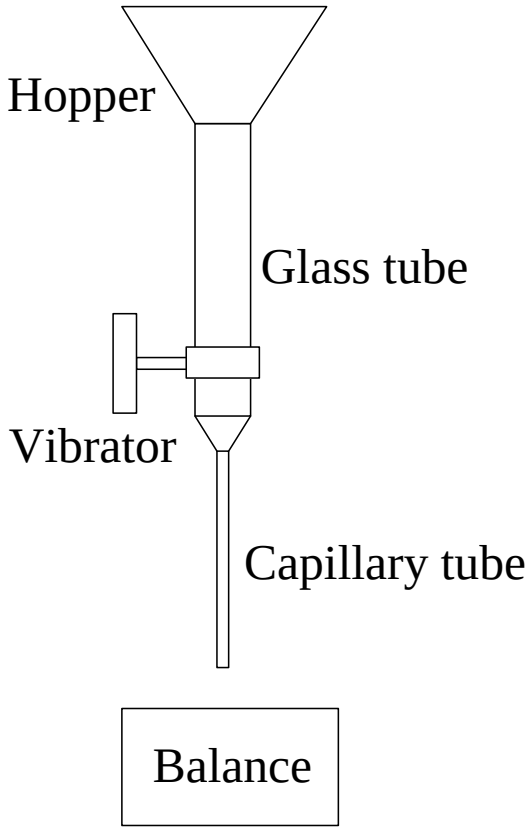

Figure 2.12: Schematic diagram of the apparatus for vibrating capillary method

The vibration acceleration, v_a, is given by Equation (2.6),

$$v_a = a(2\pi f)^2 \tag{2.6}$$

where v_a is the vibration acceleration, a is the vibration amplitude and f is the vibration frequency. A typical flowability profile is shown in Figure 2.13.

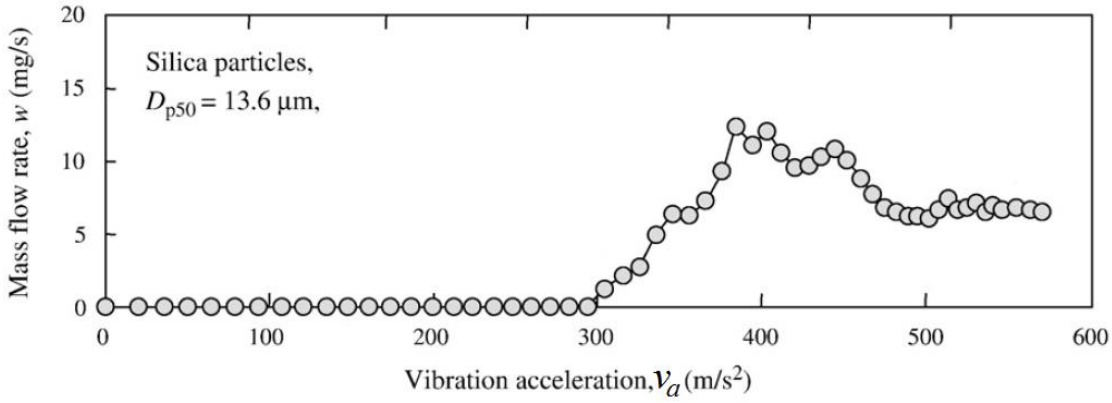

Figure 2.13: Typical flowability profile obtained by vibration capillary method [14]

As it can be seen, there is a critical vibration acceleration at which the particles start flowing out of the capillary tube. Beyond this critical acceleration, the mass flow rate initially increases, although eventually reaches an asymptote. Jiang *et al.* [14] considered this critical vibration acceleration to be characteristic of the flow behaviour of the bulk and compared this with the results obtained by an angle of repose test for different grades of polymethylmethacrylate particles (see Figure 2.14).

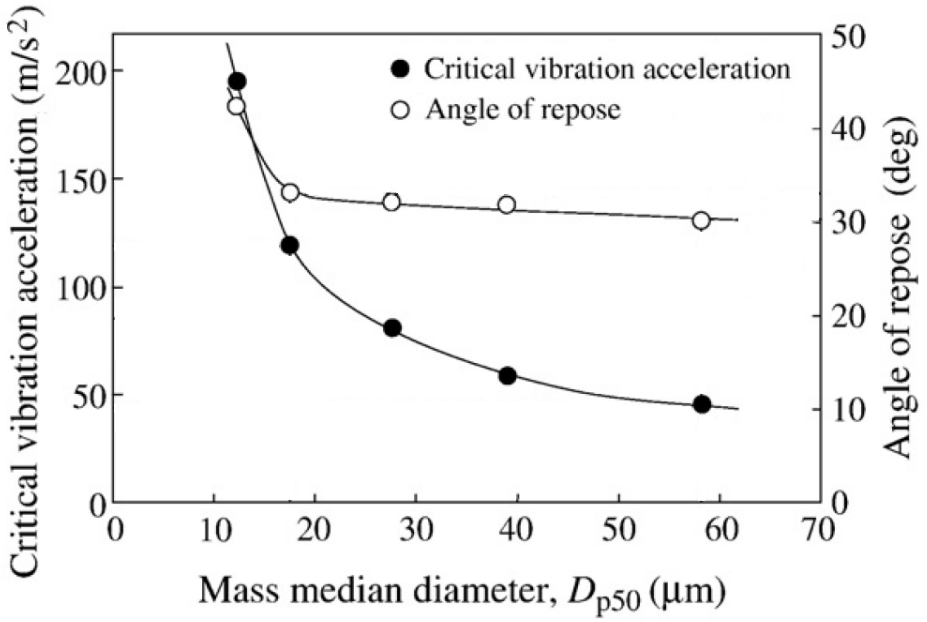

Figure 2.14: Comparison of critical vibration acceleration in vibrating capillary method and angle of repose for different grades of polymethylmethacrylate particles [14]

Qualitatively there is good agreement between the results obtained by the vibration capillary method and those obtained by angle of repose test.

2.3.5 **Ball indentation**

Different samples of powders are pre-consolidated into a cylindrical die to various low pressures. The die must be made of low friction materials (e.g. PTFE) in order to reduce the effects of wall friction. The surface is then indented using a spherical indenter and the "depth/load" cycle is recorded. The loading speed is chosen so that the indentation process is within the quasi-static regime. From the recorded depth/load cycle, the hardness of the consolidated bulk is determined.

Histroically indentation has been used to determine the hardness of continuum materials. Hardness represents the resistance of a material to plastic deformation which is an important factor in processes such as comminution, tableting, polishing and attrition since it defines the mode and pattern of mechanical failure [15]. Hardness is affected by anisotropy in the structure of the material, yield stress, coefficient of friction and the geometry of the deformed region. There are a number of indentation test methods for solid materials using different geometries of indenter such as sphere, pyramid and cone [16]. The hardness number for these cases is calculated from the applied force, the projected area of the impression and shape of the indenter. Spheres tend to be better options for indentation of bulk powders, since they do not include sharp edges which may be comparable in size with individual particle size. Moreover it is important to avoid further consolidation of the sample during the indentation process. If the specimen is consolidated during indentation the hardness value that is measured afterwards may not be representative of the pre-consolidation stress of interest. The curvature of a sphere results in a smoother transition from elastic to plastic behaviour and allows the powder to be sheared rather than consolidated. During loading, the load is increased at a specified rate until a desired maximum load is reached. Then the load is decreased during unloading back to zero at the same rate. During unloading, the elastic deformation of the sample will recover. This is schematically shown in Figure 2.15.

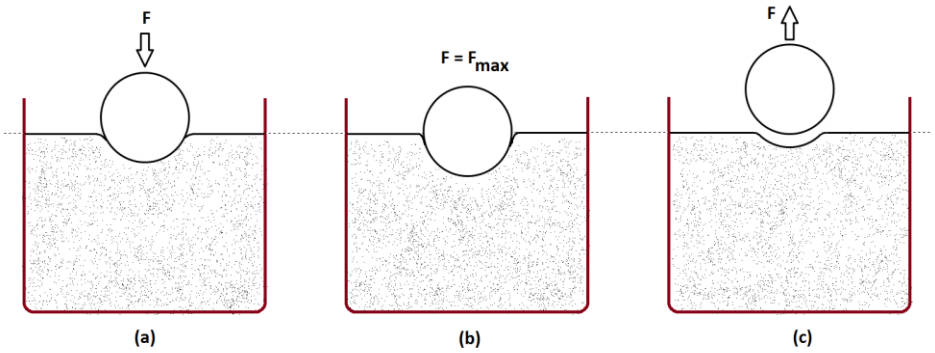

Figure 2.15: Schematic diagram of indentation during (a) loading, (b) maximum loading and (c) unloading

In the indentation test, a continuous recording of the applied force and the penetration depth is made. A typical load/depth curve is shown in Figure 2.16.

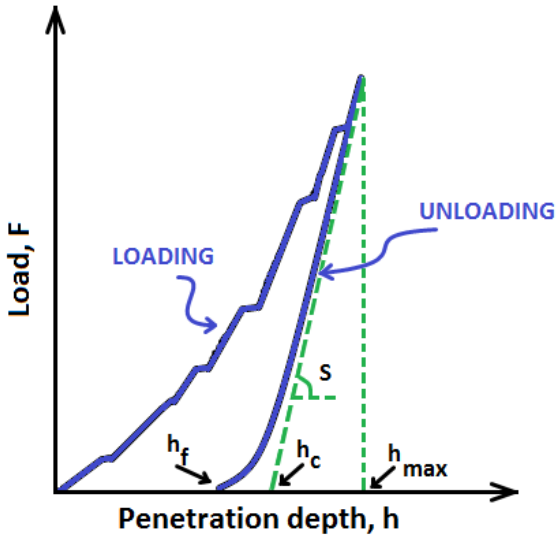

Figure 2.16: Typical indentation load/depth curve

It is noticeable that the unloading curve is not vertical, which shows recovery of the elastic deformation during unloading. The maximum depth, the maximum load and the

characteristics of the unloading curve are used to calculate the hardness. Hardness is given by the ratio of maximum indentation load to projected area of the impression,

$$H = \frac{F_{\max}}{A} \tag{2.7}$$

where A is the area of the base of the spherical cap that is formed by the impression. The relationship between a sphere and its spherical cap is given by [17],

$$r = \frac{(h^2 + r_b^{\,2})}{2h} \tag{2.8}$$

where r is the radius of the spherical indenter, r_b is the radius of the base of the cap and h is the height of the cap. By rearranging Equation (2.8) the projected area can be expressed in terms of size of the indenter and depth of impression,

$$A = \pi r_b^{\,2} = \pi(dh - h^2) \tag{2.9}$$

where d is the diameter of the indenter and h is the depth of the impression. The depth of the impression can be evaluated from the load/depth curve i.e. the intercept point of unloading cycle and penetration depth axis (h_f). As it can be seen from Figure 2.16 there is a change in the height of the powder bed at the end of the unloading cycle. This behaviour is the result of interactions between the indenter and the powder bed. For instance, in the case of cohesive powders, the adhesive force between the indenter and powder bed results in a slight surface lift at the end of unloading. In order to disregard the effects of such interactions in hardness calculations, an extrapolated depth (h_c), which is representative of the initial elastic unloading, is used in Equation (2.9). h_c can be calculated by estimating the tangent to the initial elastic part of the unloading curve. The slope of the tangential line determines the location of h_c on the penetration depth axis. In the indentation test, during formation of the local plasticity zones around the

indenter, the volume of the powder bed present in a yield condition is surrounded by an elastically deformable region. This implies that the hardness is larger than the plastic yield stress. This effect is called the plastic constraint [18], and is defined as the ratio of hardness over yield stress,

$$C = \frac{H}{Y} \tag{2.10}$$

where C is the constraint factor, H is the hardness and Y is the yield stress. This factor is usually greater than unity due to the increase in the local yield strength that is caused by the elastically deforming region around the indent. In order to define the flow function it is essential to relate hardness to yield strength. Wang *et al.* [5] have concluded that indentation hardness and unconfined yield stress have a linear relationship with pre-consolidation pressure for a number of materials. This corroborates the linear relationship between yield stress and hardness observed for continuum solids, therefore indicating a constant constraint factor for a given material. Figure 2.17 shows the comparison between the indentation hardness and unconfined yield stress of Avicel.

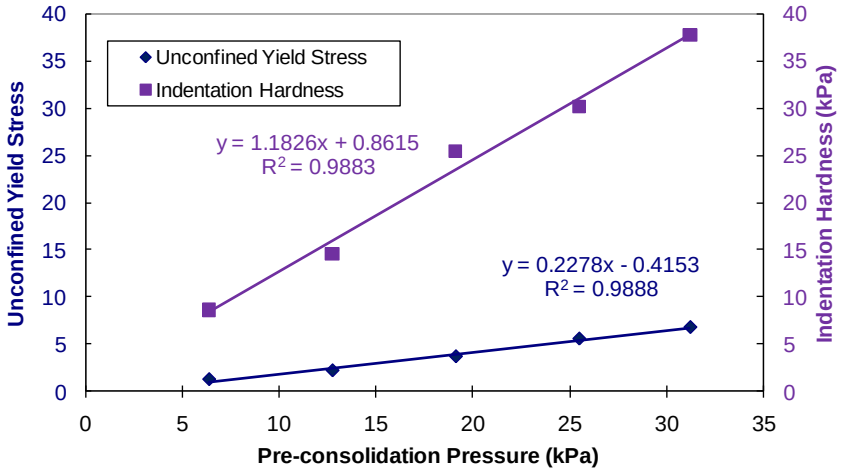

Figure 2.17: The comparison between the indentation hardness and unconfined yield stress as a function of pre-consolidation pressure for Avicel [5].

Hassanpour and Ghadiri [4] considered a constraint factor of 3 in order to evaluate the yield strength of α-lactose, magnesium carbonate and salinised glass beads. These results were compared to yield strengths measured by uniaxial compression test. A good correlation between the indentation hardness and unconfined yield stress was found for α-lactose and magnesium carbonate. However, the yield stresses obtained from ball indentation and unconfined compression for salinised glass beads did not follow the same trend. This can be ascribed to the difference in constraint factor for salinized glass beads. Subsequently Wang *et al.* [5] evaluated the constraint factor for Avicel, starch and lactose monohydrate by comparing the results of indentation and uniaxial compression. The results are shown in Figure 2.18.

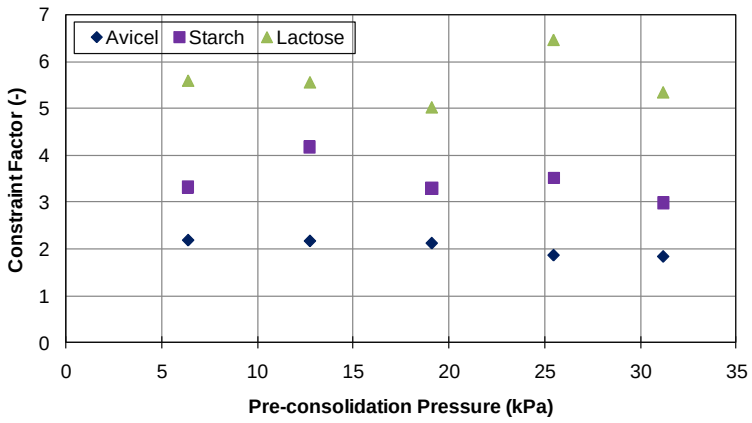

Figure 2.18: The relationship between constraint factor and pre-consolidation pressure for Avicel, Starch and Lactose [5]

It can be concluded that the constraint factor is independent of the pre-consolidation pressure and it is material dependant. The constraint factor for various types of continuum solid materials has been reported in the literature. Hill [19] showed that only for rigid-perfectly plastic materials, can the constraint factor be estimated as 3. Tabor [16] stated that the constraint factor of 3 is only applicable for ductile metals. Johnson [20] proposed the following relationship between the indentation hardness and yield stress for elastic-perfectly materials, which cover a wide range of continuum solids,

$$\frac{H}{Y} = \frac{2}{3}\left[1 + \ln\left(\frac{Ea}{3YR}\right)\right] \tag{2.11}$$

where E is Young's modulus, a is the radius of the impression and R is the indenter radius. Equation (2.11) is applicable to continuous solids, and may not be valid for discrete particulate systems. For particle assemblies there is no reported work in the literature and the constraint factor depends on single particle properties such as particle shape, stiffness and inter-particle friction. It was suggested by Wang *et al.* [5] to

investigate the effects of single particle properties on the constraint factor using DEM analysis.

Zatloukal and Sklubalova [21] studied dynamic indentation of powders using spherical indenter. In their work, the spherical indenter was released from a height above the unconsolidated bulk solids and the depth of the impression was measured experimentally. Using bulk density of the powder and the volume of impression, the "mass of indentation" was calculated using the following equation,

$$M_i = V_i \times \rho_b \tag{2.12}$$

where M_i is the mass of indentation, ρ_b is the bulk density and V_i is volume of the impression which is calculated based on the depth of impression (h) and indenter radius (R) as follow,

$$V_i = \frac{1}{3}\pi h^2 \left(3R - h\right) \tag{2.13}$$

In order to evaluate the flowability, mass flow rate, Q_m, of the testing powders was measured and correlated to the indentation mass. Sodium citrate, potassium citrate, sorbitol, and boric acid with three size fractions in the range of 0.315 – 0.630 mm were used in the experiments. The correlation is shown in Figure 2.19.

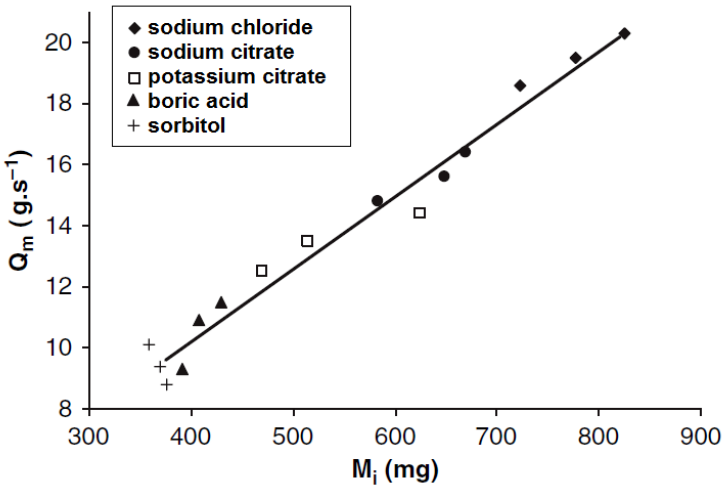

Figure 2.19: Linear correlation of mass flow rate and indentation mass [21]

The mass flow rate was found to have a linear correlation with indentation mass for all the materials except sorbitol. They ascribed this exception to cohesivity of the sorbitol powders which leads to agglomeration of the particles. A similar behaviour was found for correlation of volume flow rate, Q_v, and indentation volume, v_i (Figure 2.20).

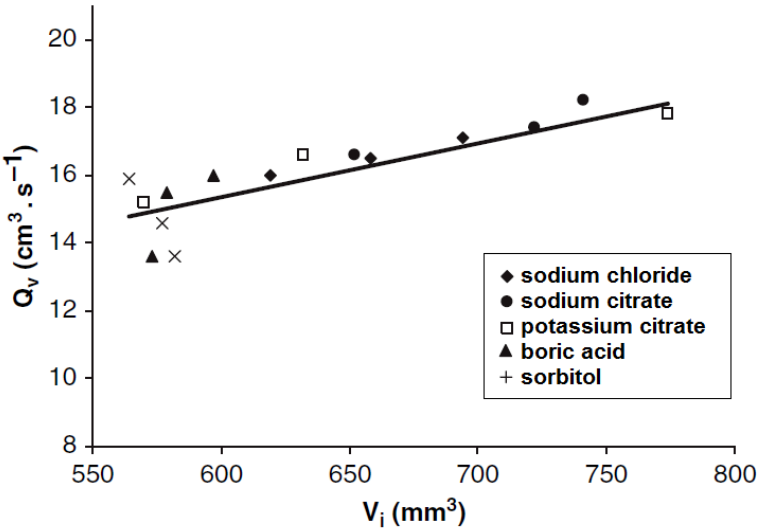

Figure 2.20: Linear correlation of volume flow rate and indentation mass [21]

It was concluded that this method of indentation can be considered as a simple method for qualitative measurement of flowability of powders. The results were found to be comparable to compressibility tests and Carr index. This technique needs to be developed further by investigating more materials for a range of indentation rate. In this method, effects of the dynamics of the indenter must also be investigated since the indenter is dropped onto the surface of the bulk at relatively high velocities. This is discussed in the next section.

2.4 Comparison of flowability measurement techniques

As discussed previously, in order to obtain a quantitative statement regarding flowability of bulk solids it is essential to measure strength of the bulk for a given consolidation state, i.e. consolidation stress (σ_1) and yield strength (σ_c). This eliminates the effects of powder testers on the measurements which in turn enables a comparison of flow properties of bulk solids measured by different testing apparatuses. Schulze [3] suggested seven criteria that a test apparatus should have in order for a powder tester to provide quantitative and reliable results:

1. consolidation procedure with subsequent measurement of strength;
2. consolidation of the bulk solids test specimen until steady state flow has been reached;
3. not too much difference in directions of loading and testing application i.e. similar orientations of the major principal stresses during consolidation and measurement of strength;

4. reproducible load application of the bulk solids specimen for consolidation (4a) and for measuring strength (4b);
5. known average stresses in the measuring plane with possibly the most uniform stress distribution for consolidation (5a) and for measuring strength (5b);
6. possibility for varying consolidation stresses (adjustment to application of test results);
7. possibility for measuring increase of strength with time (time consolidation if required for the application).

During the consolidation procedure of the uniaxial compression test there is a chance that the consolidated bulk is non-homogenous. Moreover, friction between the solids and cylindrical wall may result in a severe underestimation of the yield strength [8]. Nevertheless simplicity of testing procedure in uniaxial compression test is the reason behind common usage. In contrast to the uniaxial compression test, shear testers are more complex and the measurement are more time consuming. However, the preshear process of a shear tester transfers the bulk solid into a fairly reproducible consolidation state and hence the results are more reliable and reproducible compared to the uniaxial test. With the Sevilla powder tester, the tensile strength of bulk solids is measured which makes it applicable for cases where bulk solids are under tension instead of compression or very low applied loads. Although bulk solids can be consolidated to a reproducible steady state flow condition, it has been suggested by Schwedes [8] that results from this novel technique should be compared with common tensile strength testers such as uniaxial tensile tests in order to assess its reliability. It should also be noted that the stress history can be removed and that the reproducible steady state flow

can be achieved if the bulk specimen can be fluidised [3]. Moreover, the consolidation level of the reproducible state is limited; powder bed height and density defines the state of consolidation.

Angle of repose is a very limited but simple testing technique. There is no control on the consolidation state of the bulk solids and therefore no quantitative statement regarding flowability of the powder can be possible. However this simple and cost-effective technique gives a good qualitative evaluation of the flow behaviour for a range of powders. The vibrating capillary method also provides qualitative measurement of the powder flow, although the flow function cannot be determined since the consolidation state of the bulk is not controllable. The ball indentation method has the potential to become a commonly used technique due to its ability to measure flowability at low compression stresses using very small quantities of powders. However further developments are required regarding determination of the constraint factor. In addition to Schulze criteria for flowability measurement apparatuses, three additional criteria can be outlined as follows,

8. Possibility for measuring small consolidation stresses.
9. Requirement of relatively small quantities of testing powder.
10. Quantifying variation of strength across the sample.

A comparison of the potential capability of the common powder flowability measurement techniques based on Schulze and the three additional criteria is summarised in Table 2.3.

Table 2.3: Comparison of the common powder flowability measurement techniques based on Schulze and three additional criteria.

Criteria →	1	2	3	4	5	6	7	8	9	10	Comments
Uniaxial test	✓	×	✓	✓	✓	✓	✓	×	×	×	Simple, but a powder is not conditioned to a reproducible state. The sample size must be large enough to avoid influence of the confining walls.
Biaxial test	✓	✓	✓	✓	✓	✓	✓	×	×	×	Similar to uniaxial test, but the yield locus can be measured confidently by comparison of multiple points.
Shear test	✓	✓	✓	✓	✓	✓	✓	×	×	×	Time-consuming, but the powder is presheared to achieve a well-defined and reproducible state. The major principal and unconfined stresses are determined confidently.
Sevilla powder tester	✓	✓	✓	✓	✓	✓	×	✓	×	×	Tensile strength of the bulk can be measured, but the process is rather time-consuming. The powder can be pre-conditioned only if it is fluidisable. Loosely compacted samples can be used.
Angle of repose	×	×	×	×	×	×	×	×	×	×	Very simple. Gives qualitative results. The unconfined yield stress cannot be determined. The consolidation state of the bulk is not controlled.
Vibration capillary test	×	×	×	×	×	×	×	×	×	×	Gives qualitative results. The unconfined yield stress cannot be determined. The consolidation state of the bulk is not controlled.
Ball indentation	✓	×	✓	✓	×	✓	✓	✓	✓	✓	Multiple tests can be performed on the same sample to determine the distribution of strength. Very small quantities are required. It can be performed on loosely compacted samples but a powder is not conditioned to a reproducible state. The unconfined yield stress is not directly measured.

CHAPTER 3 Distinct Element Method (DEM)

The macroscopic bulk behaviour of powders is governed by the microscopic activity of the individual particles in an assembly. This implies that in order to gain a better understanding of particulate systems and their functioning, the particle interactions at the microscopic level must be analysed. It is currently very difficult to investigate the behaviour of individual particles within a bulk assembly experimentally. Therefore it is helpful to model the behaviour of particles by the use of numerical simulations. Furthermore the use of computer simulations provides a cost effective method as an alternative to experiments since no physical material or process equipment is required, provided that the simulation results are validated. Simulations are invaluable for cases for which actual experiments are hazardous such as process handling of radioactive powders. For particulate solids, the most appropriate approach for this purpose is the use of computer simulation by the Distinct Element Method (DEM). The principal of DEM was first introduced by Cundall and Strack [22]. In this technique, Newton's laws of motion is applied to describe particle motion and to describe the particle interactions with its neighbours, contact mechanics is applied. Under the assumption that within a time-interval the velocity of the elements is unchanged and particle interactions do not go beyond its neighbour, the position of the elements is updated. A complete review of the methodology of the DEM and its applications are presented elsewhere [23, 24]. In this chapter a brief summary of the methodology is provided. A detailed review of contact models, which have been proposed for DEM, is given since this aspect has not been reviewed adequately in the literature. Different approaches of incorporation of particle shape in DEM simulations are also reviewed.

3.1 **Time-step**

Particulate systems are composed of distinct particles which displace independently from one another and interact only at contact points [22]. Movement of a particle within a granular flow is affected not only by the forces and torques originated from contacts with its immediate neighbouring particles, but also by disturbance propagations from particles far away. In order to avoid evaluation of effects of disturbance waves in DEM, the particle displacement calculations are performed after a time-step, within which the disturbance cannot propagate from each particle further than its immediate neighbouring particles [22].The speed of disturbance waves is approximated by Rayleigh surface wave propagation based on physical properties of the discrete medium. The time must be sufficiently smaller than Rayleigh time-step in order to ensure realistic force transmission rates in the assembly and to prevent numerical instability [25]. The Rayleigh time-step is given by Equation (3.1).

$$T_R = \frac{\pi R\left(\frac{\rho}{G}\right)^{1/2}}{0.1631\upsilon + 0.8766} \tag{3.1}$$

where R is the particle radius, ρ is the density, G is the shear modulus and υ is the Poisson's ratio of the particle. In practice, a fraction of this maximum value is used for the integration time-step. For dense systems with high coordination numbers (4 and above) a typical time-step of $0.2T_R$ has been shown to be appropriate. For lower coordination numbers $0.4T_R$ is more suitable [26]. Since the time-step varies with different particle materials, for an assembly consisting of different material type particles, the critical time-step should be the smallest among those determined for different material properties [25].

3.2 Motion calculations

Each particle within a granular flow can have two types of motion: translational and rotational. Newton's second law of motion is used to calculate the translational and rotational accelerations. By integrating the accelerations over a time-step, particle velocities and positions are updated. The rotational motion is calculated based on Equation (3.2).

$$I\frac{d\omega}{dt} = M \tag{3.2}$$

where I is the moment of inertia, ω is the angular velocity, M is the resultant contact torque acting on the particle and t is time. The translational motion is calculated based on Equation (3.3).

$$m\frac{dV}{dt} = F_g + F_c + F_{nc} \tag{3.3}$$

where V is the translational velocity of the particle, m is the mass of the particle, F_g is the resultant gravitational force acting on the particle and F_c and F_{nc} are the resultant contact and non-contact forces between the particle and surrounding particles or walls. Figure 3.1 is a schematic representation of these forces.

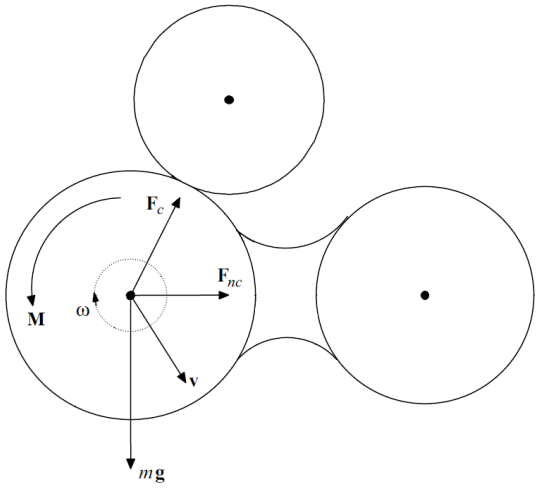

Figure 3.1: Schematic representation of the forces acting on a particle

3.3 Contact and non-contact forces

Particle interactions are not just due to particle collisions and inter-particle contacts. Particles may interact with each other while they are apart from each other, e.g. in the case of charged particles, attractive or repulsive forces may influence the particles motion. The following section is a brief review of common non-contact forces which may be present in particulate systems.

3.3.1 Van der Waals forces

Van der Waals force is a result of dipole interactions between molecules. Different electronic configurations of molecules give them a dipolar character which may result in attractions. Van der Waals force operates both in gaseous and liquid environments, although it is substantially reduced in liquid environments [27]. Hamaker [28] calculated the interaction force between a sphere and a semi-infinite body, by summarising all the possible individual molecular interactions, as follows [29],

$$F_{van} = \frac{A_H R}{12 d^2} \tag{3.4}$$

where A_H is the Hamaker coefficient which is a material property related to the molecular properties of the particle with radius of R, and d is the separation distance between the two bodies. The van der Waals forces become noticeable when particles can come sufficiently close together, that is at separation distances of the order of the size of a molecule (i.e. 0.2 to 1nm). Moreover, the magnitude of van der Waals forces becomes negligible compared with that of the gravitational force when the particle size exceeds a few microns. This is due to the fact that the gravitational force is proportional to the cube of the particle diameter, but the van der Waals force is proportional to the diameter. Once the particles are in contact, the overall van der Waals attraction is increased significantly due to increase in the contact area. This situation is enhanced when plastic deformation takes place [27].

3.3.2 **Liquid bridges**

In humid systems (with a relative humidity of > 60%) capillary condensation of the fluid in the gap between the particles in close contact may take place resulting in an attraction. The maximum attraction is achieved for two smooth spherical particles if the liquid covers the particle surfaces completely. For this case, the liquid bridge attraction force, F_{LB}, can be calculated as follow [27],

$$F_{LB} = 2\pi\gamma R \tag{3.5}$$

where γ is the surface tension of the liquid and R is the radius of the two particles.

3.3.3 **Electrostatics**

Electrostatic forces can form as a result of tribo-electric charging or formation of a potential difference between particles. In the latter case, charged particles attract adjacent uncharged particles due to their own image charge. The attraction force can be evaluated by the classical Coulomb equation [27],

$$F_{t\_elec} = \frac{Q^2\left(1-\frac{d}{\sqrt{R^2+d^2}}\right)}{16\pi\varepsilon_0 d^2} \tag{3.6}$$

where Q and R are the charge and radius of the charged particle, d is the separation distance between the two bodies, and ε_0 is the permittivity of the vacuum. In the former case i.e. potential difference, particles with a different work-function can form a potential difference when they are brought together. This results in an attraction force which can be calculated as follows [27],

$$F_{V\_elec} = \frac{\pi\varepsilon_0 R}{d}\left(\Delta V\right)^2 \tag{3.7}$$

where ΔV is the potential difference formed by the contact. It should be noted that in humid environments the Coulomb attraction is reduced to zero due to the fact that particle surfaces are covered by the liquid, which mostly is a conductor resulting in charge leakage and discharging.

3.4 **Contact Force Models**

In order to consider particle interactions in the calculations, the resulting forces from particle collisions and contacts are modelled. There exist a number of force models which mostly allow particles to have deformation. The deformation is modelled as an overlap between particles. In the general case of an assembly of many particles, the

contact force model is applied at each contact and the vectorial sum of these contact forces is determined to yield the resultant contact force acting on that particle [22]. There has been extensive work in the literature in order to develop accurate and/or computationally efficient models based on theories of contact mechanics to be employed in DEM simulations. Mostly these models are developed for spherical contacts based on Hertz theory. Following is a brief review of the most commonly used contact models. Four categories are considered for contact models: elastic, elasto-plastic, elastic-adhesive and elasto-plastic-adhesive models. For each category normal and tangential contact models are described.

3.4.1 **Elastic contacts**

3.4.1.1 Linear spring contact model

In this simple model [22] the contact force between two perfectly elastic spheres is resolved into normal and shear components with respect to the contact plane,

$$F = \vec{F}_n + \vec{F}_s \tag{3.8}$$

where F is the contact force, and F_n and F_s are the normal and shear components of the contact force. The normal contact force is calculated from the overlap of the particles in contact,

$$F_n = k_n \alpha_n \tag{3.9}$$

where α_n is the normal overlap and k_n is the normal stiffness at the contact which can be calculated as follow,

$$k_n = \frac{k_n^1 k_n^2}{k_n^1 + k_n^2} \tag{3.10}$$

where k_n^1 and k_n^2 are the normal stiffness for the particles in contact. Figure 3.2 shows a schematic force-overlap response of linear-spring model.

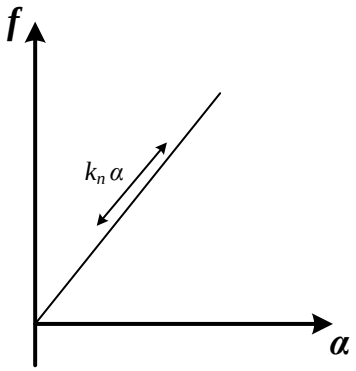

Figure 3.2: Schematic of force-overlap response of linear-spring model

The increment of shear force in this model is calculated from,

$$\Delta F_s = -k_s \Delta \alpha_s \tag{3.11}$$

where $\Delta\alpha_s$ is the increment of shear displacement of the contact and k_s is the shear contact stiffness which can be calculated as follow,

$$k_s = \frac{k_s^1 k_s^2}{k_s^1 + k_s^2} \tag{3.12}$$

where k_s^1 and k_s^2 are the shear stiffness for the particles in contact. The total shear force is found by summing up the previous shear force with the increment of shear force,

$$F_s = F_s^{'} + \Delta F_s \tag{3.13}$$

where $F_s^{'}$ is the previous shear force [22].

3.4.1.2 Hertz normal contact model

Based on this model [30], the normal contact force between two perfectly-elastic spheres in contact is given by [31],

$$F_n = \frac{4}{3} E^* R^{*1/2} \alpha^{3/2} \tag{3.14}$$

where E^* and R^* are the equivalent Young's modulus and radius which are given by Equations (3.15) and (3.16), respectively, and α is the normal overlap.

$$E^* = \left(\frac{1-\upsilon_1^2}{E_1} + \frac{1-\upsilon_2^2}{E_2} \right)^{-1} \tag{3.15}$$

E_1 and E_2 are Young's moduli of the particles in contacts, and υ_1 and υ_2 are Poisson's ratios of the particles in contact.

$$R^* = \left(\frac{1}{R_1} + \frac{1}{R_2} \right)^{-1} \tag{3.16}$$

R_1 and R_2 are the radii of the particles in contact.

3.4.1.3 Mindlin and Deresiewicz's tangential contact model

Mindlin and Deresiewicz [32] developed a tangential model for perfectly elastic contacts. Due to tangential slip at the contact, the tangential force-displacement relationship depends on the loading history and on the rate of change of the normal and tangential force. Following is a description of the model for cases where the normal displacement does not change (i.e. the radius of the contact area is constant) through the change of tangential force:

The tangential force is calculated using the following general equation,

$$f_t = f_{t0} + k_t\left(\alpha_t - \alpha_{t0}\right) \tag{3.17}$$

where f_{t0} is the previous tangential force, $\alpha_t - \alpha_{t0}$ is the change in tangential displacement (the same as $\Delta\alpha_s$ in the linear-spring model) and k_t is the tangential stiffness. Initially, when the tangential displacement starts increasing, the tangential stiffness is calculated based on Equation (3.18),

$$k_t = k_{t0}\left(1 - \frac{f_{t1}}{\mu f_n}\right)^{1/3} \tag{3.18}$$

where μ is the coefficient of sliding friction and k_{t0} and f_{t1} are given by Equations (3.19) and (3.21), respectively.

$$k_{t0} = 8G^* R^{*1/2}\alpha_n^{1/2} \tag{3.19}$$

where G^* is the equivalent contact shear modulus given by Equation (3.20),

$$G^* = \left(\frac{1-\upsilon_1^2}{G_1} + \frac{1-\upsilon_2^2}{G_2}\right)^{-1} \tag{3.20}$$

where G_1 and G_2 are the shear moduli of the particles in contact.

$$f_{t1} = \frac{2}{3}k_{t0}\alpha_t \tag{3.21}$$

The contact starts sliding (macro-slip) once the tangential force reaches Coulomb's limit of friction given by Equation (3.22).

$$\left|f_t\right| \le \mu\left|f_n\right| \tag{3.22}$$

Before the macro-slip occurs, there are regions in the contact area where the shear stress exceed the Coulomb's limit [33]. Therefore, small local tangential displacement occurs while the remainder of the contact area is not relatively displaced. This phenomenon is known as micro-slip. If the contact is unloaded in the tangential direction, the unloading path on the force-displacement curve would be different to that of the loading curve due

to the micro-slip. Mindlin and Deresiewicz [32] considered a hysteretic behaviour to account for the micro-slip, by which the unloading tangential stiffness is given by,

$$k_t = k_{t0}\left(1-\frac{f_t^{TP}-f_{t1}}{2\mu f_n}\right)^{1/3} \tag{3.23}$$

where f_t^{TP} is the tangential force at the point when the contact is unloaded tangentially (turning point). The unloading curve follows Equation (3.23) up to $-f_t^{TP}$, where the history of the turning point becomes insignificant [32]. If the contact is unloaded further, the tangential stiffness is the same as the initial stiffness which is given by Equation (3.18). In the case of subsequent turning points, the tangential stiffness is evaluated using the following equation,

$$k_t = k_{t0}\left(1-\frac{f_{t1}-f_t^{TTP}}{2\mu f_n}\right)^{1/3} \tag{3.24}$$

where f_t^{TTP} is the tangential force at the second turning point. Figure 3.3 shows a schematic tangential force-displacement response of Mindlin and Deresiewicz's model.

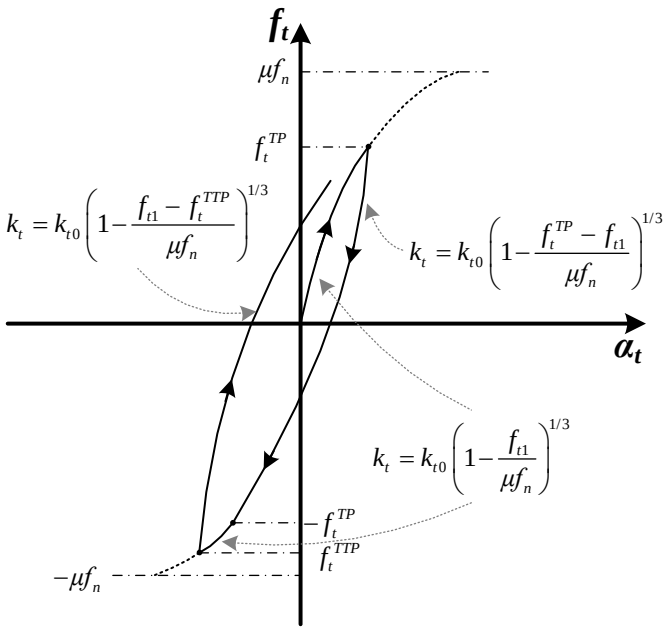

Figure 3.3: Schematic tangential force-overlap response of Mindlin and Deresiewicz's model

In cases where both the tangential and normal displacements vary, the tangential force is evaluated by assuming that the change in the normal displacement is not significant. Mindlin and Deresiewicz [32] considered a "simple loading history" which enables solving the problem by superposition of the effects of change in tangential and normal displacements. This simple loading history defines a linear tangential stiffness which facilitates the tangential force to be adopted for the response corresponding to the new normal force. It is best to make use of illustrations to describe this complicated model. Figure 3.4 shows the tangential force-displacement response of the case where both normal and tangential displacements increase.

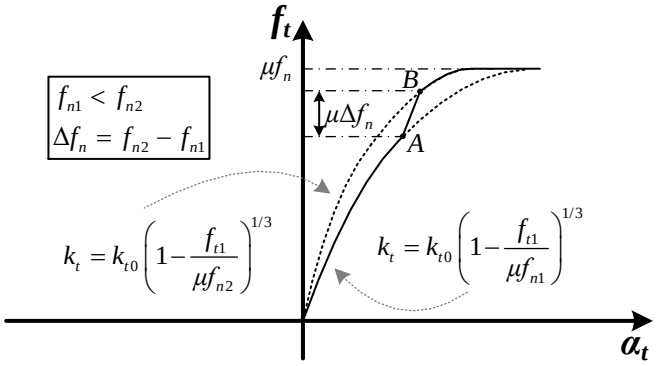

Figure 3.4: Schematic tangential force-overlap response of Mindlin and Deresiewicz's model for the case where both normal and tangential displacements increase

In Figure 3.4, initially the tangential force increases while the normal force is assumed to be constant with a value of f_{n1}. For this part of the loading, the tangential stiffness is calculated based on Equation (3.18). At point *A*, the normal force is increased by Δf_n to the value f_{n2}. Based on the simple loading history that Mindlin and Deresiewicz [32] proposed, the contact is loaded with a linear tangential stiffness so that the response meets the response of a contact which was loaded initially with a constant normal force of f_{n2} at point *B* which corresponds to a tangential force of $\mu\Delta f_n$. For unloading and reloading cases near turning points, the response of the model is treated in the same manner.

3.4.1.4 Mindlin's no-slip tangential contact model

Mindlin [34] proposed a tangential model for perfectly elastic contacts by neglecting the effects of micro-slip. The hysteretic behaviour which was considered for Mindlin and Deresiewicz's model [32] is not present in this model. The loading and unloading path of the tangential force is the same and the tangential stiffness is given by,

$$k_t = 8G^* R^{*1/2} \alpha_n^{1/2} \tag{3.25}$$

Di Renzo and Di Maio [35] simulated oblique impact of a particle to a flat wall at different impact angles using the linear spring, Mindlin's no-slip and Mindlin and Deresiewicz's models. The comparison of the results to the experimental findings of Kharaz *et al.* [36] are shown in Figure 3.5.

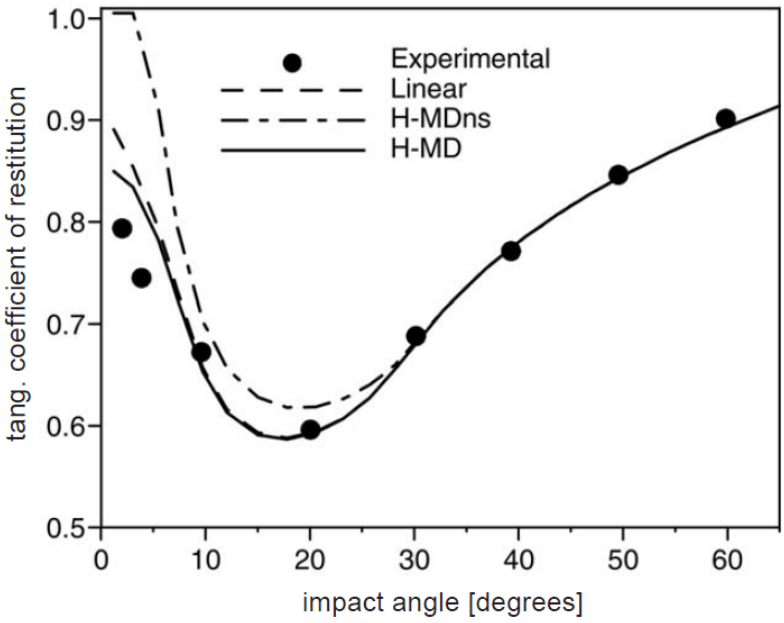

Figure 3.5: Comparison of linear-spring, Mindlin's no-slip and Mindlin and Deresiewicz's models with the experimental data for oblique impact of a particle at different impact angles [35]

Figure 3.5 shows a very good agreement of the three models with the experimental results, except for small impact angles. The linear model surprisingly produced better results compared to Mindlin's no-slip model.

3.4.1.5 Di Renzo and Di Maio's no-slip tangential contact model

Di Renzo and Di Maio [37] proposed a modification to Mindlin's no-slip tangential model [34] so that the macro-slip occurs at the same tangential overlap that Mindlin and Deresiewicz[32] predicted. The tangential stiffness is given by Equation (3.26),

$$k_t = \frac{2}{3} k_{tM} = \frac{16}{3} G^* R^{*1/2} \alpha_n^{1/2} \tag{3.26}$$

where k_{tM} is the tangential stiffness of Mindlin's no-slip model. This model has the advantage of being simple and computationally cost-effective (similar to Mindlin's no-slip model). Figure 3.6 shows comparison of Mindlin's no-slip [34], Di Renzo and Di Maio's no-slip [37] and first loading of Mindlin and Deresiewicz's [32] tangential models.

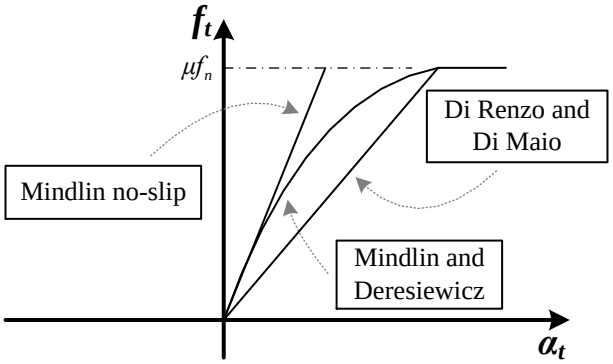

Figure 3.6: Comparison of Mindlin's no-slip, Di Renzo and Di Maio's no-slip and first loading of Mindlin and Deresiewicz's tangential models.

It was analytically shown that for small impact angles the model of Di Renzo and Di Maio provides a better match to Mindlin and Deresiewicz's model in cases where both normal and tangential displacements occur compared to the no-slip model of Mindlin [37]. Di Renzo and Di Maio [35, 37] compared the tangential force response of Hertz-

Mindlin's no-slip (HM), Hertz-Mindlin and Deresiewicz's (HMD) and Hertz-Di Renzo and Di Maio's (HDD) for a particle impacting on a flat wall at different impact angles. Figure 3.7 shows the tangential force-displacement of the three models at two different impact angles.

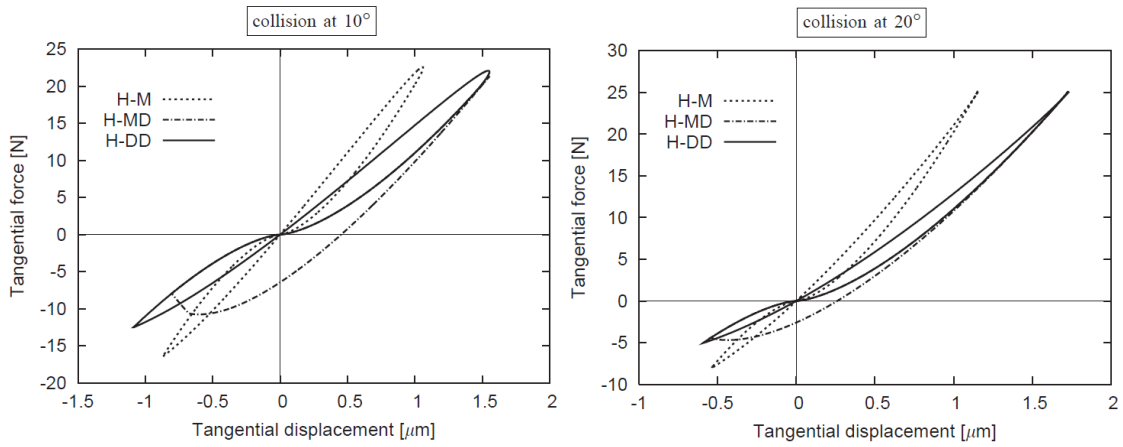

Figure 3.7: Tangential force-displacement of Hertz-Mindlin's no-slip (HM), Hertz-Mindlin and Deresiewicz's (HMD) and Hertz-Di Renzo and Di Maio's (HDD) models at two different impact angles [37]

As it can be seen, HDD model shows a better agreement with HMD compared to HM model. The tangential force-displacement response of HDD model becomes closer to that of HMD model at higher impact angles.

3.4.2 Elasto-plastic contacts

3.4.2.1 Thornton's elasto-plastic normal contact model

In this model [38] the contact force follows Hertz elastic model until it reaches the yield force after which the contact is deformed plastically. The yield force is given by Equation (3.27),

$$F_y = \frac{\pi^3 R^{*2}}{6E^{*2}} p_y^3 \tag{3.27}$$

where p_y is the yield pressure of the contact. Plastic deformation in this model is governed by a constant stiffness of $\pi p_y R^*$ based on the assumptions that the contact pressure does not increase further than the yield pressure and that the pressure distribution over the contact area is Hertzian [31]. The contact force during plastic deformation can be calculated using the following equation,

$$F_n = F_y + \pi p_y R^* \left(\alpha - \alpha_y\right) \tag{3.28}$$

where α_y is the overlap at which the contact yields and is given by,

$$\alpha_y = \frac{\pi^2 R^*}{4E^{*2}} p_y^2 \tag{3.29}$$

If plastic deformation occurs during the loading stage, the contact curvature during unloading is less than that of the elastic unloading curvature due to permanent deformation of the contact surfaces. During unloading, the force-displacement behaviour is assumed to be elastic and is provided by the Hertz equations but with a curvature of $1/R_p^*$ corresponding to the point of maximum compression. This curvature can be evaluated based on the maximum force the contact experiences during the plastic loading, F_{max}, as given by Equation (3.30),

$$R_p^* = \frac{4E^*}{3F_{\max}}\left(\frac{2F_{\max}+F_y}{2\pi p_y}\right)^{3/2} \tag{3.30}$$

Since the unloading is considered to be purely elastic based on Hertz theory [30], the equation for the unloading is given by,

$$F_n = \frac{4}{3}E^* R^{*1/2}\left(\alpha-\alpha_p\right)^{3/2} \tag{3.31}$$

where α_p is the permanent plastic deformation given by Equation (3.32),

$$\alpha_p = \alpha_{\max}\left(1-\frac{R^*}{R_p^*}\right) \tag{3.32}$$

where α_{max} is the maximum overlap during plastic loading. Figure 3.8 is a schematic force-overlap response of Thornton's model.

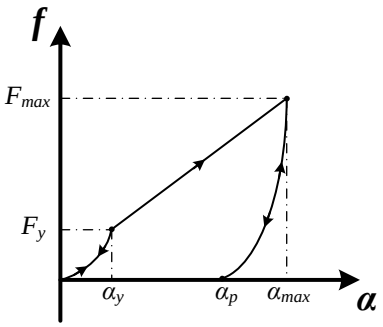

Figure 3.8: Schematic force-overlap response of Thornton's elasto-plastic model

Finite Element Analysis (FEA) of elasto-plastic contacts showed that when the normal stress exceeded the yield pressure, the force-overlap curves were not straight lines [39]. This is shown in Figure 3.9.

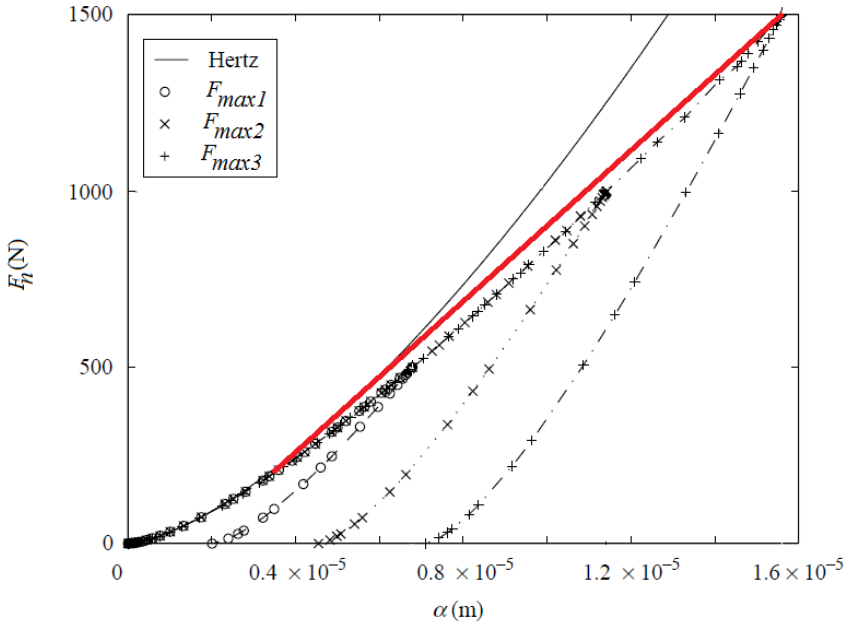

Figure 3.9: FEA force-overlap response of an elasto-plastic contact obtained by Vu-Quoc and Zhang [39]. The contact is unloaded at three different maximum overlaps.

In Figure 3.9 a red line is drawn from the yield point to the maximum loading overlap in order to show that the response in the plastic regime is not linear as assumed by Thornton [31]. It is noteworthy however, that the non-linear response in the plastic regime does not significantly deviate from the linear extrapolation. This shows that the assumptions made by Thornton for a linear plastic stiffness may be adequate.

Vu-Quoc and Zhang [39] compared the pressure distribution over the contact area obtained by FEA to that of Hertz for different maximum overlaps (see Figure 3.10).

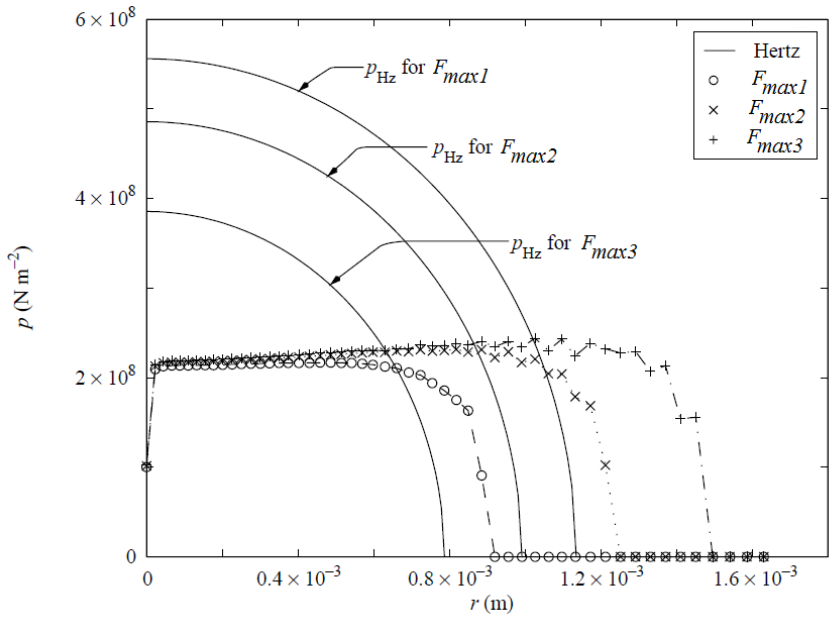

Figure 3.10: Pressure distribution over half of the contact area obtained by FEA and Hertzian pressure distribution for three different maximum loading force

The shape of the distribution in the plastic regime obtained by FEA is in agreement with Thornton's assumption where a Hertzian pressure distribution with a cut-off corresponding to the limiting contact pressure was assumed [31]. However, as it was denoted by Vu-Quoc and Zhang [39], the maximum contact pressure in Thornton's model is larger than the one obtained by the FEA. As a result, the radius of the contact area obtained from FEA is less than the one predicted by Thornton for the same normal force.

3.4.2.2 Vu-Quoc and Zhang's elasto-plastic normal contact model

Vu-Quoc and Zhang [39] proposed a non-linear elasto-plastic model for spheres in collision, based on additive decomposition of the radius of the contact area into an elastic part and a plastic part. In this model the contact follows Hertz elastic curve up to

a yield point (similar to Thornton's model). The yield force for two identical spheres in contact is given by Equation (3.33),

$$F_y = \frac{\pi^3 R^2 \left(1-\upsilon^2\right)^2}{6E^2}\left(A_y\left(\upsilon\right) p_y\right)^3 \tag{3.33}$$

where $A_y(\upsilon)$ is a scalar depending only on Poisson's ratio. Vu-Quoc and Zhang [39] did not define this scalar, however Vu-Quoc *et al.* [40] provided two example values; for Poisson's ratio of 0.3, $A_y(\upsilon) = 1.61$ and for $\upsilon = 0.4$, $A_y(\upsilon) = 1.74$. Comparing Equations (3.33) and (3.27), it can be observed that the yield force calculated in Thornton's model [38] is very similar to that of Vu-Quoc and Zhang's. Vu-Quoc and Zhang [39] derived a very complex equation for evaluation of contact force during plastic deformation which is given by,

$$\left(F_n - F_y\right) + \frac{1}{C_a}\left(\frac{3R\left(1-\upsilon^2\right)}{4E}F_n\right)^{1/3} - \frac{1}{C_a}\left(\left[1+K_c\left(F_n - F_y\right)\right]R\alpha_n\right)^{1/2} = 0 \tag{3.34}$$

where C_a and K_c are fitted parameters obtained from FEA results. C_a in fact defines the relationship between the plastic component of the contact radius and the contact force. K_c defines the permanent deformation relative to the particle radius. Equation (3.34) is a very complex equation for which there is no straight-forward solution. Vu-Quoc and Zhang [39] suggested solving this equation by Newton-Raphson iterative method provided a tolerance value. They showed that for a number of cases within a reasonable tolerance, the equation can be solved after a few iterations [39]. For calculation of the unloading contact force, Hertzian behaviour is considered where a corrected contact curvature, R_p^*, is considered similar to Thornton's model. R_p^* is given by following equation.

$$R_p^* = \left(1 + K_c \left(F - F_y\right)\right) R^* \tag{3.35}$$

Vu-Quoc and Zhang [39] compared the force-overlap response of the FEA results and that of their model to the response of Thornton's model which is shown in Figure 3.11.

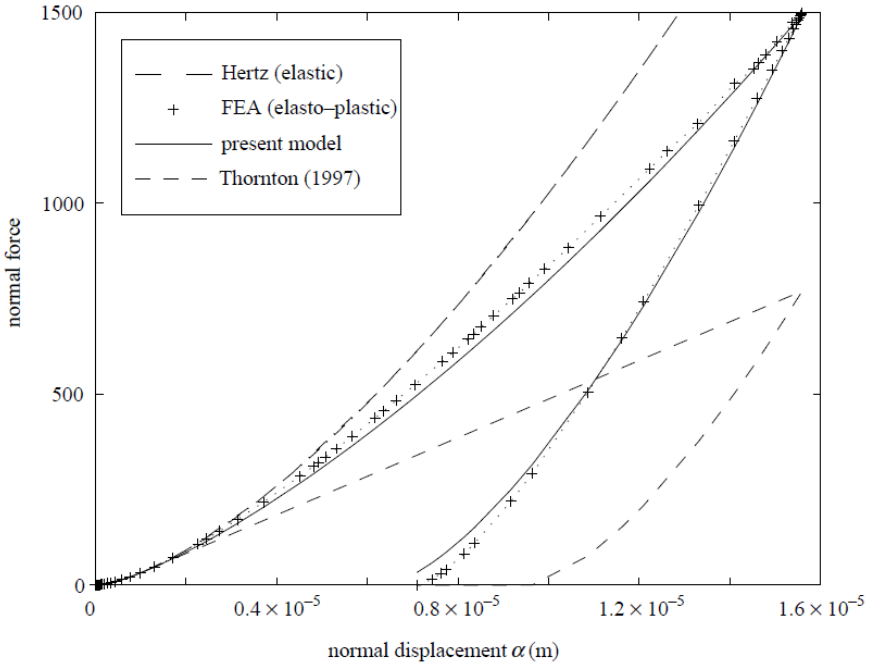

Figure 3.11: Force-overlap response of FEA, Vu-Quoc and Zhang's and Thornton's models [39]

The elastic part of the response in all models overlaps, since they all considered Hertzian behaviour for this region. During the plastic deformation, however, the response of Thornton's model shows significantly lower plastic stiffness compared to the responses of Vu-Quoc and Zhang's model and FEA. The agreement between the FEA results and those of Vu-Quoc and Zhang's model is expected since the parameters of the model are evaluated from FEA simulations. Following is a critique of this model:

For the plastic regime, the contact radius, a_{ep}, is considered to be addition of the elastic Hertzian contact radius, a_e, and a plastic contact radius, a_p. Figure 3.12 shows the plastic contact radius, a_p, as a function of normal contact force, where a_p is calculated by subtracting a_e from the results of FEA [39].

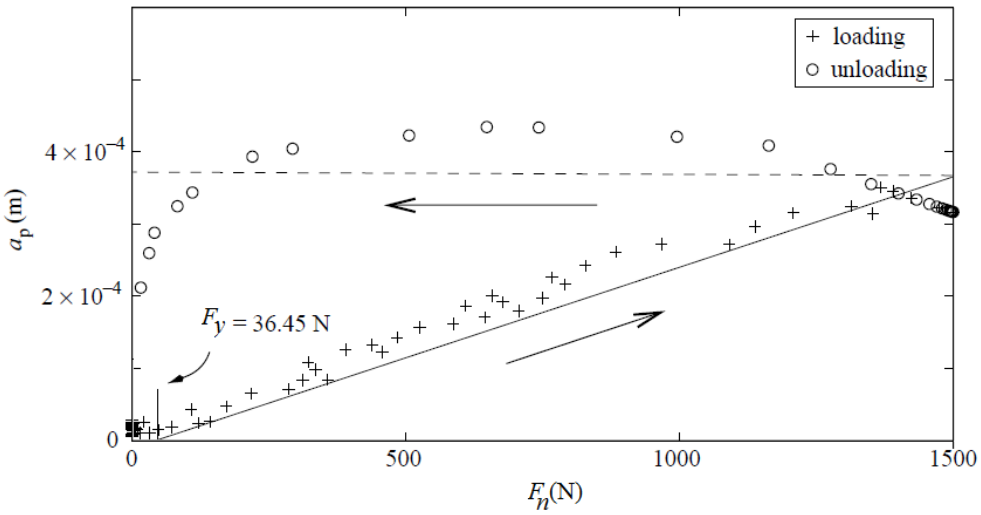

Figure 3.12: Plastic contact radius as a function of normal contact force during loading and unloading of a contact [39]

Vu-Quoc and Zhang concluded from Figure 3.12 that the plastic contact radius is a linear function of normal contact force during plastic contact loading. The parameter C_a is in fact the slope of this linear line. The unloading part of the response in Figure 3.12 surprisingly shows dependency of a_p with contact unloading force. In fact, the plastic contact radius reduces to almost half of its maximum value during unloading. Therefore the contact unloading is not purely elastic. Vu-Quoc and Zhang claimed that FEA simulations were performed for elastic-perfectly plastic materials, which contradicts the unloading behaviour of Figure 3.12. The full description of FEA simulations is

necessary to verify this. In general, the complexity of the non-linear equation for evaluation of plastic contact force as well as the fact that FEA simulations must be performed previously in order to get the input parameters of this model, result in increasing the computational cost extensively.

3.4.2.3 Walton and Braun normal elasto-plastic model

Walton and Braun [41] proposed a simple linear model for elasto-plastic contacts. For contact loading, the normal force is given by,

$$F_n = k_p \alpha \tag{3.36}$$

where k_p is the plastic stiffness. The unloading force is calculated based on Equation (3.37),

$$F_n = k_e (\alpha - \alpha_0) \tag{3.37}$$

where k_e is the elastic stiffness and α_0 is the permanent contact deformation. Figure 3.13 shows a schematic of the force-overlap response of this model.

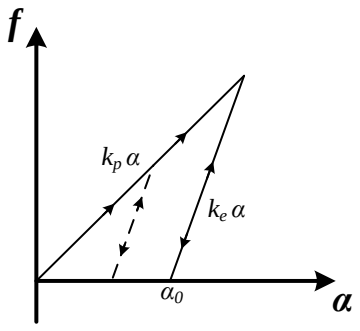

Figure 3.13: Schematic force-overlap response of Walton and Braun's [41] model with constant coefficient of restitution

Since the slopes k_p and k_e are constant, the coefficient of restitution of this model is independent of impact velocity ($e = (k_p/k_e)^{1/2}$). This is not in agreement with experimental and numerical analyses in the literature [42]. In order to account for dependency of coefficient of restitution on impact velocity, Walton and Braun [41] suggested an elastic unloading stiffness which increased linearly with the maximum loading force with a slope *S*. The equation for the elastic stiffness is given by,

$$k_e = k_p + S.F_{\max} \tag{3.38}$$

where F_{max} is the maximum loading force. The parameter *S* was not given any physical definition. However, one can specify *S* on the basis of giving the best fit of the unloading line of the model to the Hertz elastic equation. Figure 3.14 shows a schematic force-overlap response of Walton and Braun's [41] model with varying coefficient of restitution.

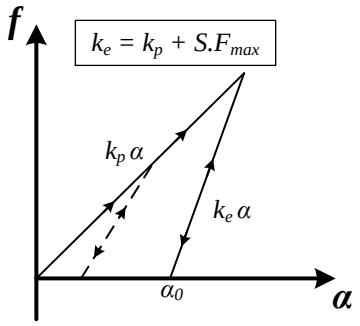

Figure 3.14: Schematic force-overlap response of Walton and Braun's [41] model with varying coefficient of restitution

A more comprehensive model may consider the contact to be elastically deforming (with stiffness k_e) initially up to a yield limit above which the contact deforms

plastically, similar to the models of Thornton, and Vu-Quoc and Zhang. However, in real contacts, the presence of asperities always leads to plastic deformation from the beginning of loading. Moreover, for typical ratios of Young's modulus to yield stress of elasto-plastic materials, the initial elastic deformation is negligible: considering Thornton's model, the single particle strain at which the contact yield occurs can be calculated by dividing the yielding overlap, which is given by Equation (3.29), by $2R^*$. Hence the yield strain, γ_y, is given by,

$$\gamma_y = \frac{\alpha_y}{2R^*} = \frac{\pi^2}{8} \times \left(\frac{p_y}{E^*} \right)^2 = \frac{\pi^2}{8} \times \frac{1}{C^2} \tag{3.39}$$

where C is the ratio of effective Young's modulus to contact yield pressure which typically has a minimum value of about 50 and can range up to a few 1000 for materials with notable plastic component. Figure 3.15 shows the yield strain (percentage) as a function of C which ranges from 50 to 300.

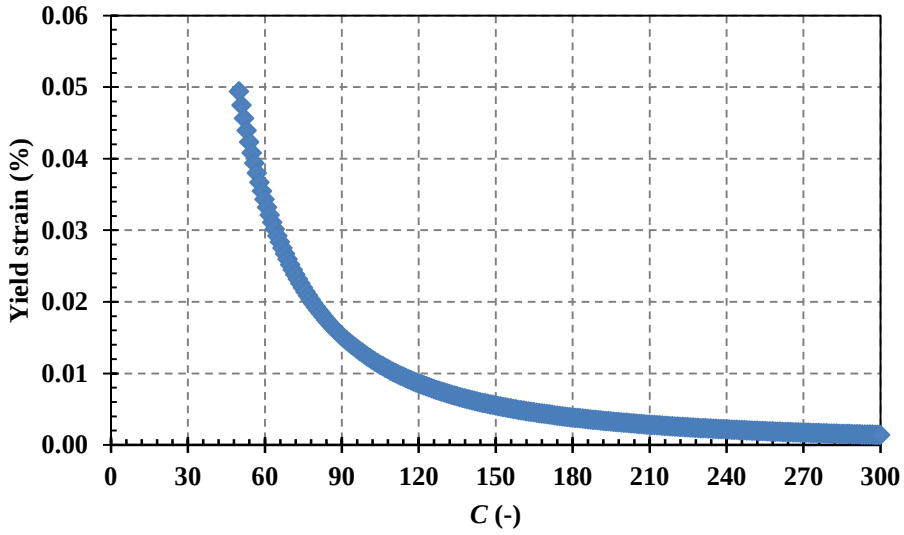

Figure 3.15: Yield strain as a function of C

It can be concluded that generally the yield strain is negligible; therefore excluding an initial elastic deformation for the contact model would not prevent the model from capturing the realistic behaviour.

3.4.2.4 Tangential force in elasto-plastic contacts

Vu-Quoc *et al.* [43] considered the model of Mindlin and Deresiewicz [32] for FEA modelling of elasto-plastic contacts. The normal force was evaluated in a similar manner to [39] (see Section 3.4.2.2). It was shown that when the normal force is constant while the tangential displacement is increased, the tangential force-displacement curve becomes stiffer, in contrast to the case where both normal and tangential displacements are increased [43]. It was concluded that a tangential model for elasto-plastic contacts must facilitate approximation of tangential stiffening and softening under constant and varying normal force, respectively. In contrast to the analysis of Vu-Quoc *et al.* [43], Ning [44] assumed that Mindlin's no-slip solution remains valid for elasto-plastic contacts. Simulation of oblique impact of elasto-plastic particles using the model of Thornton [38] for normal force calculations and Equation (3.25) for evaluation of tangential force showed that that the tangential force-time curves were affected by plastic deformation at low impact angles, however for other impact angles the pattern of evolution was similar to that under elastic deformation [44].

3.4.3 Elastic-adhesive contacts

3.4.3.1 JKR elastic-adhesion normal contact model

JKR theory [45] assumes that the attractive forces are confined within the area of contact and are zero outside. In other words, the attractive inter-particle forces are of

infinitely short range. JKR model extends the Hertz model to two elastic-adhesive spheres by using an energy balance approach. The contact area predicted by the JKR model is larger than that by Hertz. Consequently there is an outer annulus in the contact area which experiences a tensile stress. This annulus surrounds an inner circular region over which a Hertzian compressive distribution acts [46].

Figure 3.16 shows schematically the force-overlap response of JKR model.

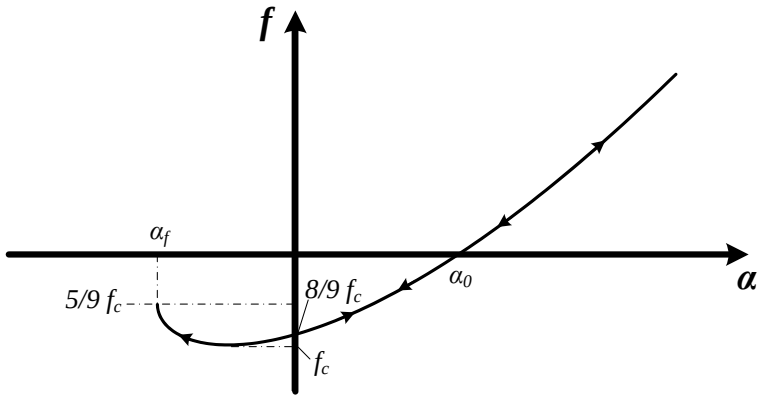

Figure 3.16: Schematic force-overlap response of JKR model

When two spheres come into contact, the normal force between them will immediately drop to a certain value (8/9 f_c, where f_c is the pull-off force [31]) due to van der Waals attractive forces. The velocity of the spheres are then reduced gradually and part of the initial kinetic energy is radiated into the substrates as elastic waves. The particle velocity will reduce to zero at a point where the contact force reaches a maximum value and the loading stage is complete. In the recovery stage, the stored elastic energy is released and is converted into kinetic energy which causes the spheres to move in the

opposite direction. All the work done during the loading stage has been recovered when the contact overlap becomes zero. However at this point the spheres remain adhered to each other and further work (known as work of adhesion) is required to separate the surfaces. The contact breaks at a negative overlap, α_f, with the contact force being 5/9 f_c [44]. Pull-off force, f_c, is the maximum tensile force the contact experiences and is given by [45],

$$f_c = \frac{3}{2}\pi R^* \Gamma \tag{3.40}$$

where Γ is the interface energy. The governing equation for the force-overlap relation is given by [20],

$$F_n = \frac{4E^* a^3}{3R^*} - \left(8\pi\Gamma E^* a^3\right)^{1/2} \tag{3.41}$$

where a is the contact radius. The overlap can be evaluated by Equation (3.42) [20],

$$\alpha = \frac{a^2}{R^*} - \left(\frac{2\pi\Gamma a}{E^*}\right)^{1/2} \tag{3.42}$$

3.4.3.2 Savkoor and Briggs' tangential model for elastic-adhesive contacts

Savkoor and Briggs [47] extended the JKR model to account for the effects of varying tangential displacement. The tangential stress distribution over the contact area was considered to be the no-slip solution of Mindlin [34] (see Section 3.4.1.4), therefore the tangential force-displacement can be evaluated by Equation (3.25). By applying an energy balance, Savkoor and Briggs [47] showed that the contact radius will be affected by the tangential displacement. The contact radius is given by Equation (3.43),

$$a^3 = \frac{3R^*}{4E^*}\left(F_n + 2F_c \pm \sqrt{4F_n F_c + 4F_c^2 - \frac{F_t^2 E^*}{4G^*}}\right) \tag{3.43}$$

where F_n is the normal contact force, F_c is the JKR pull-off (see Equation (3.40)) and F_t is the tangential force evaluated by Equation (3.25). The contact radius according to the JKR model is given by [45],

$$a^3 = \frac{3R^*}{4E^*}\left(F_n + 2F_c \pm \sqrt{4F_nF_c + 4F_c^2}\right) \tag{3.44}$$

Comparing Equations (3.43) and (3.44) shows that the contact force is indeed reduced by increasing the tangential force. Savkoor and Briggs [47] suggested that this reduction corresponds to "peeling" mechanism which continues until a critical value of the tangential force, F_{tc}, is reached,

$$F_{tc} = \sqrt{\frac{16G^*}{E^*}\left(F_nF_c + F_c^2\right)} \tag{3.45}$$

If the tangential displacement increases beyond the point corresponding to F_{tc}, the peeling process is complete and the contact area would immediately reduce to the Hertzian contact area which is given by,

$$a^3 = \frac{3R^*}{4E^*}F_n \tag{3.46}$$

3.4.3.3 Thornton and Yin's tangential model for elastic-adhesive contacts

Thornton and Yin [46] proposed a modified version of Savkoor and Briggs' [47] model. Thornton and Yin [46] showed that the critical tangential force which provided peeling failure (Equation (3.45)) could be larger than the tangential force required to cause sliding. It was concluded that the contacting surfaces must "peel" before contact sliding occurs. In order to account for this, a smooth transition from peeling to sliding was proposed. The tangential and normal forces of this model follow Savkoor and Briggs

[47] model up to the critical tangential force, F_{tc}. With further tangential displacement, the tangential force is given by,

$$F_t = \mu\left(F_n + 2F_c\right)\left[1-\left(1-\frac{\alpha}{\alpha_s}\right)^{3/2}\right] \tag{3.47}$$

where α_s is given by,

$$\alpha_s = 3\mu\frac{F_n + 2F_c}{16G^* a} \tag{3.48}$$

The sliding criteria which is followed by peeling failure is given by,

$$F_t = \mu\left(F_n + 2F_c\right) \tag{3.49}$$

In order to illustrate the transition of peeling to sliding, tangential force-overlap responses of an adhesive-elastic contact with two different constant normal forces are shown in Figure 3.17.

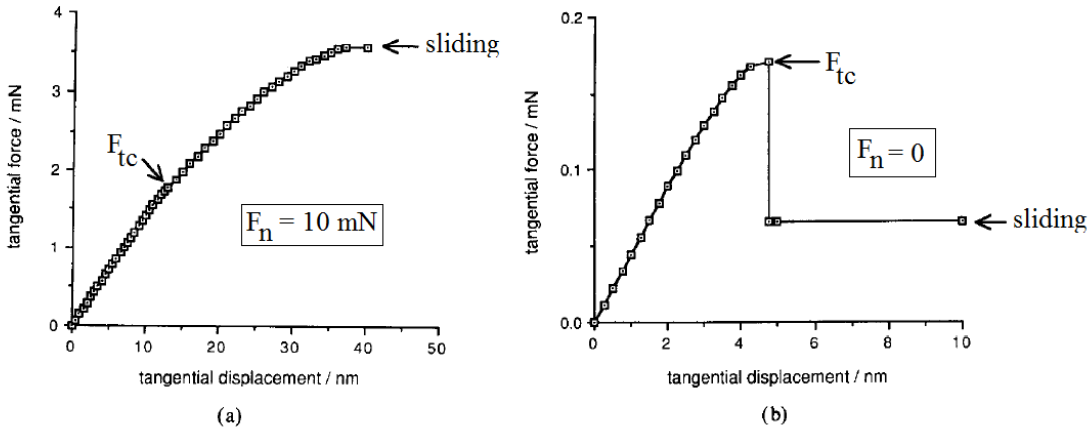

Figure 3.17: Tangential force-overlap response of Thornton and Yin's model for two different constant normal forces [46]

Figure 3.17(a) shows the smooth transition after peeling failure at point F_{tc} to the sliding point. In Figure 3.17(b) at the point where peeling is complete, the tangential force is larger than the critical sliding force, hence the force is reduced to $\mu(F_n + 2F_c)$. Thornton and Ning [46] compared their model with the results of friction measurements reported by Briscoe and Kremnitzer [48] . The comparison is shown in Figure 3.18.

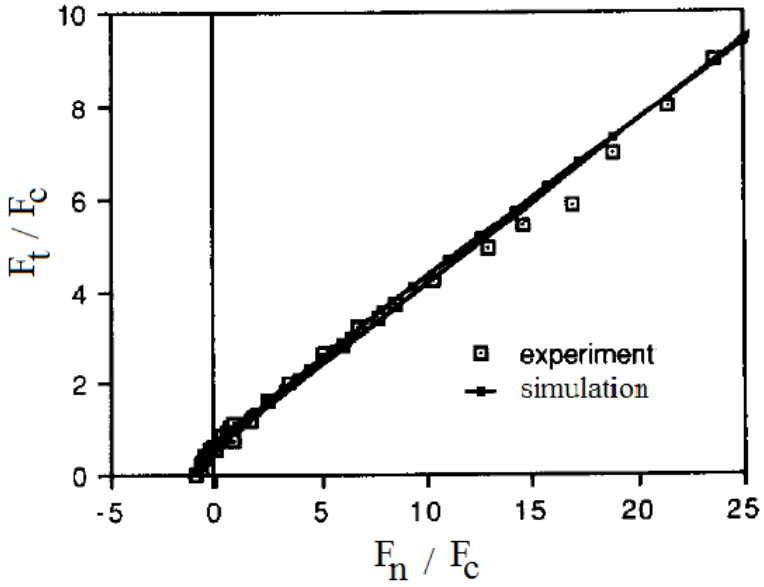

Figure 3.18: Comparison of the experimental work of Briscoe and Kremnitzer with the model of Thornton and Yin [46]

The model can therefore capture the experimental behaviour accurately.

3.4.3.4 DMT elastic-adhesive normal contact model

DMT model [49] assumes that the attractive forces all lie outside the contact zone. The attraction forces are also assumed not to change the deformed profile from that of Hertz. However outside the contact area a tensile stress is assumed to have presence which decreases with surface separation. At the point of contact prior to any deformation, the

resultant attractive force is suddenly increased to a value known as pull-off force which is given by,

$$F_c = 2\pi R^* \Gamma \tag{3.50}$$

As the spheres start deforming, the attractive force is rapidly reduced to half of its initial value. The normal contact force in this model is given by,

$$F_n = \begin{cases} F_c & \rightarrow \alpha_n = 0 \\ F_{Hertz} + \dfrac{F_c}{2} & \rightarrow \alpha_n > 0 \end{cases} \tag{3.51}$$

where F_{Hertz} is the Hertz elastic force given by Equation (3.14). Pashley [50] showed that the DMT model is valid for small, rigid spheres with a low surface energy (see below), whilst JKR model is more applicable to larger, more elastic spheres with a high surface energy. In another attempt Muller *et al.* [51] showed that the prediction of JKR and DMT models for the pull-off force was governed by the parameter,

$$\xi = \frac{8}{3\pi z_0}\left(\frac{\Gamma^2 R^*}{E^{*2}}\right)^{1/3} \tag{3.52}$$

where z_0 is the equilibrium separation. It was found that the JKR and DMT theories were accurate to within 10% for values of $\xi > 3$ and $\xi < 1$, respectively [46]. This shows that JKR model is more applicable to larger and less stiff particles with higher cohesion, and DMT model is suitable for modelling of smaller, more rigid particles with less cohesion.

3.4.3.5 Matuttis and Schinner's elastic-adhesive normal contact model

Matuttis and Schinner [52] assumed that the cohesion strength is proportional to the contact area. Based on this model, a cohesive force , F_c, is added to the contact force.

$$F_c = ka \tag{3.53}$$

where a is the contact area and k is a constant with the units of J.m^{-3}. DEM-Solutions [26] named this constant, cohesion energy density. The physical meaning of this parameter has not been given by Matuttis and Schinner [52]. Hassanpour *et al.* [53] derived an equation for the cohesion energy density based on the JKR interfacial energy by equating the tensile work of Matuttis and Schinner [52] model to the cohesion work of JKR [45] model,

$$k = 0.75\left(\frac{E^{*2}\Gamma}{R^{*}}\right)^{1/3} \tag{3.54}$$

where Γ is the JKR interfacial energy. Figure 3.19 compares the force-overlap responses of the models of Hassanpour *et al.* [53] and JKR [45].

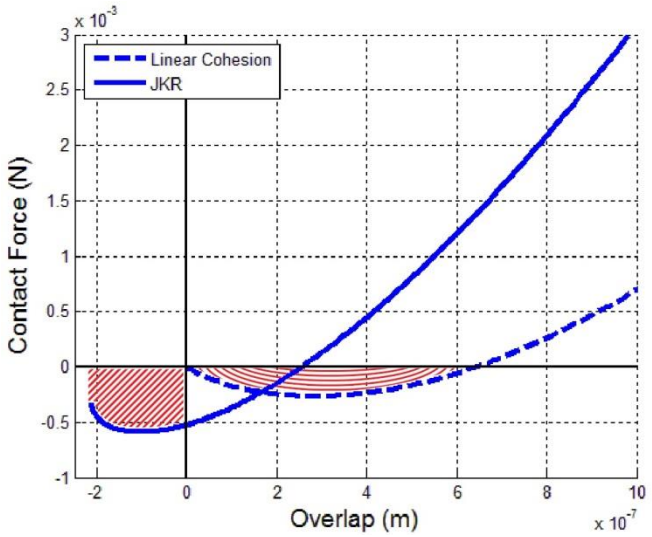

Figure 3.19: Comparison of force-overlap response of JKR and Hassanpour *et al.* models [53]

As it can be seen, the contact force in the compressive side deviates extensively from that of JKR. It must be noted that Hassanpour *et al.* [53] used this model to simulate a

high shear granulation process. The dynamics of such systems results in collision-dominant behaviour, in which the influence of contact stiffness is insignificant (see e.g. [54]).

3.4.4 Elasto-plastic and adhesive contacts

3.4.4.1 Thornton and Ning's elasto-plastic and adhesive normal contact model

Thornton and Ning [31] followed the same approach as Thornton [38] used for elastic-adhesive contacts, to develop a model for elasto-plastic and adhesive contacts. The pressure distribution over the contact area was considered to be the same as that of JKR model with a cut-off corresponding to the limiting contact pressure. Based on this assumption, an equation was derived for the contact yield pressure which is given by Equation (3.55),

$$p_y = \frac{2E^* a_y}{\pi R^*} - \left(\frac{2\Gamma E^*}{\pi a_y}\right)^{1/2} \tag{3.55}$$

where a_y is the contact radius at which the plastic yield occurs. During the plastic deformation, the contact deforms linearly with a stiffness which is given by Equation (3.56),

$$k_n = \frac{3\pi R^* \sigma_y - 2E^* a_y \left(a_c / a\right)^{3/2}}{3 - \left(a_c / a\right)^{3/2}} \tag{3.56}$$

where a_c is the contact radius at the pull-off force given by Equation (3.57) and a is the JKR contact radius from which the normal overlap can be evaluated (see Equation (3.42)).

$$a_c = \left(\frac{3R^* f_{ce}}{4E^*}\right)^{1/3} \tag{3.57}$$

where f_{ce} is the JKR pull-off force given by Equation (3.40). If plastic deformation occurs during the loading stage, the contact curvature during unloading is less than that of elastic unloading curvature due to permanent deformation of the contact surfaces. During unloading the force-displacement behaviour is assumed to be elastic-adhesive and is provided by the JKR equations, but with a curvature of R_p^* corresponding to the point of maximum compression. This curvature can be evaluated based on the maximum force the contact experiences during the plastic loading, F_{max}, as given by Equation (3.58),

$$R_p^* = \frac{R^* F_{\max}^*}{F_{\max} + \sqrt{4F_{ce}F_{\max}^*}} \tag{3.58}$$

where $F_{\max}^*$ is the equivalent JKR force of F_{max}. The plastic pull-off force (i.e. the maximum tensile force the contact experiences after plastic deformation) of this model is given by Equation (3.59),

$$F_{cp} = \frac{3}{2}\pi\Gamma R_p^* \tag{3.59}$$

Figure 3.20 shows a schematic force-overlap response of Thornton and Ning's model.

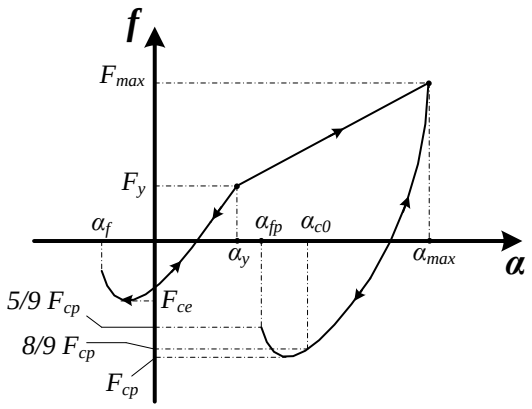

Figure 3.20: Schematic force-overlap response of Thornton and Ning's model

The contact is considered to break at the overlap α_{fp} where the contact force is equal to 5/9 f_{cp}. The contact, however, can be re-established at overlap α_{c0} where the contact force is equal to 8/9 f_{cp} [44]. This is similar to the JKR theory for the elastic-adhesive contacts, where the contact is considered to relax after detachment. Thornton and Ning [31] simulated impact of a spherical particle to a flat wall at different impact velocities using their elasto-plastic and adhesive model. The force-overlap response of the impacts at three different impact velocities is shown in Figure 3.21.

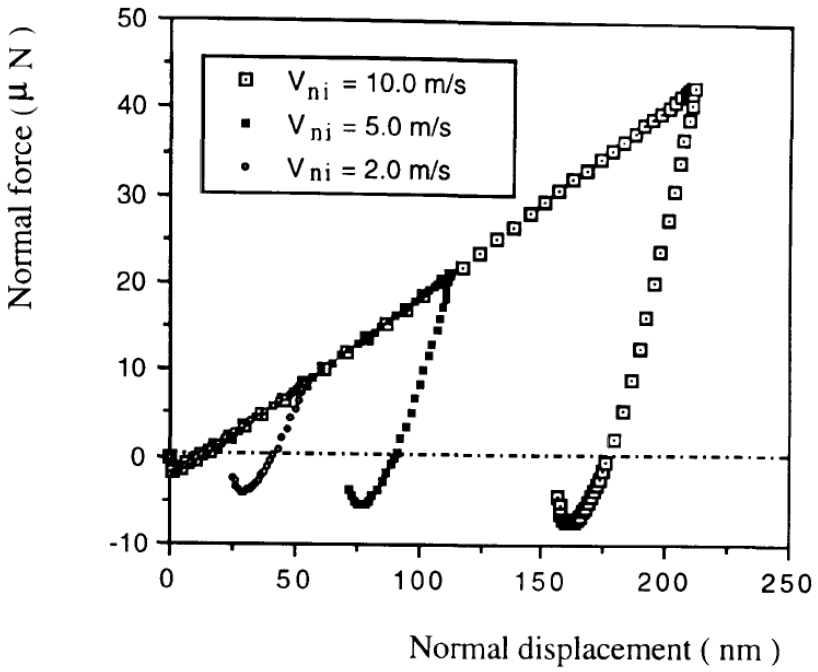

Figure 3.21: Force-overlap response of impact of a particle to a flat wall at three different impact velocities using Thornton and Ning's elasto-plastic and adhesive model [31]

The slope of the loading curve is the same for all three different velocities. It is evident that in the elastic recovery process, the pull-off force increases with an increase of impact velocity; an indication that plastic deformation leads to an increase in the radius

of contact curvature. Thornton and Ning [31] also obtained the dependency of coefficient of restitution with impact velocity for JKR elastic-adhesive, Thornton's elasto-plastic, and Thornton and Ning's elasto-plastic and adhesive model. The results are shown in Figure 3.22.

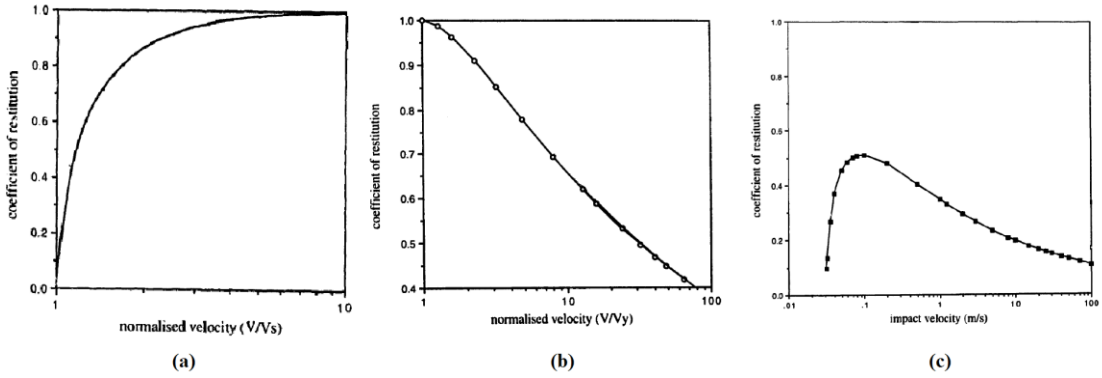

Figure 3.22: Coefficient of restitution as a function of impact velocity for (a) JKR model, (b) Thornton's elasto-plastic model, and (c) Thornton and Ning's elasto-plastic and adhesive model [31]

Elastic-adhesive contacts provide low coefficients of restitution for small impact velocities. This is due to the fact that for small impact velocities the ratio of elastic strain energy to work of adhesion is small and most of the elastic energy is utilised in overcoming the adhesion. Consequently the rebound energy is very small which provides a small rebound velocity. By increasing the impact velocity, the elastic strain energy is increased, however the work required to break the contact (i.e. work of adhesion) remains unchanged. This results in higher rebound energies and hence the increase in coefficient of restitution. With very large impact velocities, the work of adhesion becomes negligible relative to the elastic strain energy, therefore the

coefficient of restitution is very close to unity. In elasto-plastic contacts, at impact velocities which do not provide yielding, the coefficient of restitution is one. Once contact yielding occurs, a portion of the input energy is utilised in plastic deformation of the contact and therefore the elastic strain energy decreases which results in a smaller coefficient of restitution. For elasto-plastic and adhesive contacts, the coefficient of restitution initially increases, suggesting that adhesion is predominant in defining the coefficient of restitution for small impact velocities. For large impact velocities plasticity of the contact dominates the behaviour since the coefficient of restitution decreases.

3.4.4.2 Ning's elasto-plastic and adhesive tangential contact model

Ning [44] assumed that the model of Thornton and Yin [46] (see Section 3.4.3.3) is still applicable after plastic yielding. Based on this assumption the tangential interaction reduces the contact radius through the process of peeling as suggested by Savkoor and Briggs [47] (see Section 3.4.3.2). This reduction in contact radius results in a different permanent deformation, R_p^*, compared to that of the case where friction does not exist. The permanent deformation in the presence of friction is given by,

$$R_p^* = \begin{cases} \dfrac{R^* F_{\max}^*}{F_{\max} + \sqrt{4F_c F_{\max}^* - \dfrac{F_t^2 E^*}{4G^*}}} & \rightarrow \quad \dfrac{F_t^2 E^*}{4G^*} < 4F_c F_{\max}^* \\ \dfrac{R F_{\max}^*}{F_{\max}} & \rightarrow \quad \dfrac{F_t^2 E^*}{4G^*} \geq 4F_c F_{\max}^* \end{cases} \tag{3.60}$$

where F_{max} is the maximum loading force and $F_{\max}^*$ is the JKR equivalent force of F_{max}.

Ning [44] simulated the oblique impact of an elasto-plastic and adhesive particle to a flat wall at different impact angles using this model. The results are shown in Figure 3.23.

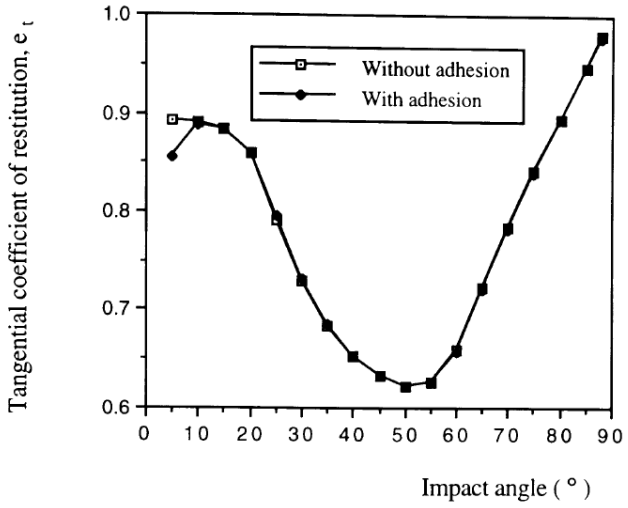

Figure 3.23: Tangential coefficient of restitution as a function of impact angle for elasto-plastic contacts with and without adhesion [44]

It can be observed that the effect of surface adhesion on tangential behaviour of the contact is not significant, since the interactions between the two contacting surfaces are dominated by the effect of plastic deformation [44]. The sensitivity of the critical impact velocity (the minimum velocity that results in a coefficient of restitution larger than zero) to coefficient of sliding friction also confirmed that the tangential behaviour of the contact in elasto-plastic and adhesive cases are similar to that in non-cohesive systems (see Figure 3.24).

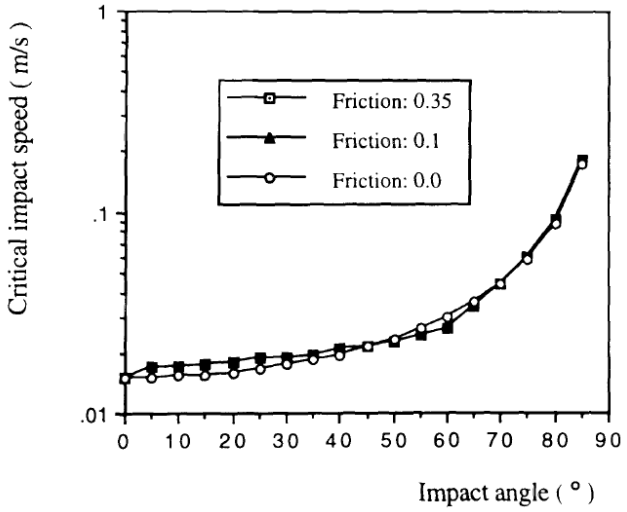

Figure 3.24: Critical impact velocity as a function of impact angle for different coefficients of sliding friction [44]

3.4.4.3 Tomas' elasto-plastic and adhesive normal contact model

Tomas [55] proposed an elasto-plastic and adhesive contact model for ultrafine particles. Short range van der Waals forces (Equation (3.61)) are considered before the two particles come into contact.

$$F_n = -\frac{A_H R^*}{6\left(a_f - \alpha_n\right)^2} \tag{3.61}$$

where A_H is the Hamaker constant (see Section 3.3.1) and a_f is the minimum separation at which van der Waals attractive forces become significant. This separation is approximately 0.3-0.4 nm [55]. Once the particles come into physical contact there is a tensile force (F_{H0}) acting on the contact. From this point the contact is considered to be elastically deformed based on Hertz theory (Equation (3.14)) up to the point where the contact pressure reaches the yield pressure. The overlap at which the contact yielding occurs is given by,

$$\alpha_y = R^* \left(\frac{3\pi p_y \left(\kappa_A - \kappa_p \right)}{2E^*} \right)^2 \tag{3.62}$$

where κ_A is elastic-plastic contact area coefficient and κ_p is plastic repulsion coefficient. κ_A represents the ratio of plastic contact deformation area to total contact deformation area. Tomas [55] showed that κ_A ranges from 2/3 (for purely elastic contacts) to 1 (for purely plastic contacts). κ_p describes a dimensionless ratio of attractive van der Waals pressure to a constant repulsive micro-yield strength p_y. Tomas [55] showed that κ_p ranges from 0 (for elastic contacts) to 1 (for soft plastic contacts). These two parameters were considered to be constant throughout the contact duration, an assumption which is valid only for very fine particles with nanometres of contact radius [55]. During plastic deformation, the contact force is a linear function of normal overlap which is given by Equation (3.63),

$$F_n = \pi R^* p_y \left(\kappa_A - \kappa_p \right) \alpha_n - F_{H0} \tag{3.63}$$

Figure 3.25 shows a schematic force-overlap response of Tomas model.

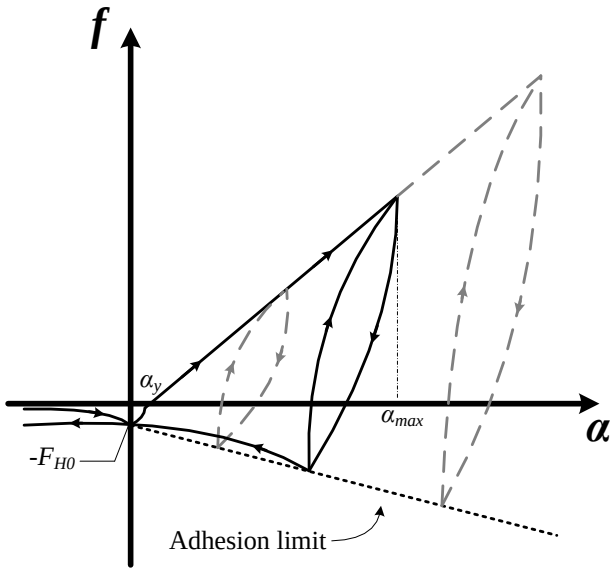

Figure 3.25: Schematic force-overlap response of Tomas' model [55].

A linear adhesion limit is considered in this model, which accounts for increasing adhesion due to increasing plastic deformation. The governing equation for this limit is given by,

$$F_{al} = -\pi R^* p_{vdW} \alpha_n - F_{H0} \tag{3.64}$$

where p_{vdW} is the van der Waals pressure. Contact unloading is assumed to be elastic and is given by,

$$F_n = \frac{2}{3} E^* R^{*3/2} \left(\alpha_n - \alpha_{al}\right)^{3/2} - \pi R^* \kappa_p p_y \alpha_{al} - F_{H0} \tag{3.65}$$

where α_{al} is the overlap at which the unloading curve reaches the adhesion limit. In the case of reloading, the force follows,

$$F_n = -\frac{2}{3} E^* R^{*3/2} \left(\alpha_{\max} - \alpha_n\right)^{3/2} + \pi R^* p_y \left(\kappa_A - \kappa_p\right) \alpha_{\max} - F_{H0} \tag{3.66}$$

which is symmetrical of unloading path with respect to the line α_{max}-α_{al}. There is no clear explanation of this hysteretic behaviour by Tomas [55]. After reaching the adhesion limit, contact unloading follows,

$$F_n = -\frac{F_{H0} a_f^2}{\left(a_f - \alpha_n\right)^2} - \frac{\pi R^* p_{vdW} \alpha_{al} a_f^3}{\left(a_f + \alpha_{al} - \alpha_n\right)^3} \tag{3.67}$$

As it can be seen schematically in Figure 3.25, the unloading stiffness increases with increasing the plastic deformation which is in agreement with Hertz non-linear theory. It can also be observed from Figure 3.25 that the contact breaks at a very small negative overlap which shows that the model does not account for permanent deformation. The independency of contact breakage on plastic history is not realistic for larger particles. It must be noted that Tomas [55] developed this model for very fine particles. For such particle size, the van der Waals forces at close proximity of the contact are still significant relative to gravitational force and therefore the model is valid for this range of particle size. Furthermore, the derivations of this model are based on molecular interactions between the bodies in contact which are the dominant factor only for very small particle sizes. For larger particles, the interactional and surface properties such as roughness and interfacial energy predominate the contact behaviour relative to molecular interactions. It is noteworthy that, in DEM simulations, the particle size is commonly scaled-up in order to increase the time-step and consequently to perform faster simulations [56] for which Tomas model cannot be employed.

3.4.4.4 Tomas' elasto-plastic and adhesive tangential contact model

Tomas [55] supplemented the Mindlin's no-slip solution [34] for the tangential force calculations in his model. The model accounts for "partial sticking the load dependent adhesion force" [55]. The tangential force is given by Equation (3.68),

$$F_t = 4G^* a\alpha_t \tag{3.68}$$

where a is the contact radius which is given by Equation (3.69),

$$a^2 = \frac{F_n + F_{H0}}{\pi p_y \left(\kappa_A - \kappa_p\right)} \tag{3.69}$$

The sliding limit of the tangential force (F_{tc}) is considered to be a function of elasto-plastic contact flattening due to the normal force and positive contribution of the adhesive force,

$$F_{tc} = \mu\left(F_n + F_{ad}\right) = \mu\left(1+\kappa\right)\left(F_{H0} + F_N\right) \tag{3.70}$$

where F_{ad} is the load dependent adhesion force (equivalent to plastic pull-off force, f_{cp}, in Thornton and Ning's model [31]) and κ is the "elastic-plastic contact consolidation coefficient" which was not clearly described by Tomas [55].

3.4.4.5 Luding's (2008) elasto-plastic and adhesive normal contact model

Luding [57] proposed a simplified linear version of Tomas's model. Figure 3.26 illustrates schematically the normal contact model of Luding for elasto-plastic and adhesive contacts.

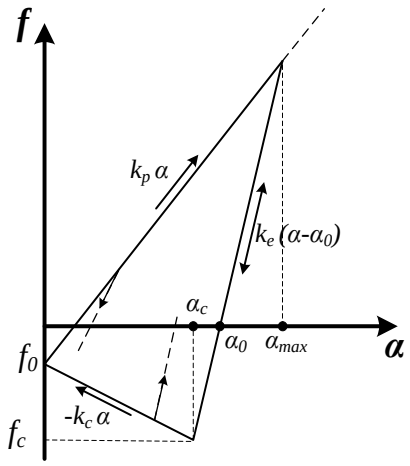

Figure 3.26: Schematic diagram of force-overlap relationship in Luding's [17] model

In this model, the normal force will immediately drop to a certain negative value, f_0, when two spheres come into contact due to van der Waals attractive forces. On initial compressive loading, the contact is considered to be plastically deforming; the contact force increases linearly with a plastic stiffness, k_p, until an overlap α_{max} is reached (α_{max} is kept in memory as a history variable). During unloading, the force drops on a line with the elastic stiffness k_e. The force decreases to zero at overlap α_0, which represents the plastic contact deformation. Reloading at any instant leads to an increase of the force along the same line with slope k_e, until the previous maximum force is reached; if α increases further beyond α_{max}, the force again follows the line with plastic stiffness k_p and α_{max} has to be adjusted accordingly. Unloading below α_0 produces an adhesive force until the maximum tensile force (i.e. pull-off force), f_c, is reached at overlap α_c. Further unloading leads to a reduction in the force on the adhesive branch with a negative stiffness $-k_c$. The maximum tensile force in this model increases by having larger deformations, i.e. increasing α_{max} would result in a larger negative f_c, similar to the models of Thornton and Ning [31], and Tomas [55]. Reloading for overlaps smaller

than α_c, follows a linear line parallel to the initial unloading line. This feature is incorporated in order to account for hysteretic unloading-reloading behaviour of Tomas' model [58]. Luding [17] considered an elastic stiffness which increased with maximum overlap based on the work of Walton and Braun [41] (see Section 3.4.2.3). A plastic flow limit overlap (α^*), i.e. the overlap beyond which the elastic stiffness becomes independent of the maximum overlap, was defined as follows,

$$\alpha^* = \frac{\hat{k}_e}{\hat{k}_e - k_p} \phi_f 2R^* \tag{3.71}$$

where $\hat{k}_e$ is the maximum value of the elastic stiffness and ϕ_f is the dimensionless plasticity depth. The plastic flow limit overlap was defined by Equation (3.72),

$$\alpha^* = \frac{\hat{k}_2}{\hat{k}_2 - k_1} \alpha_{fluid} \tag{3.72}$$

where α_{fluid} is the "stress-free fluid overlap" which can be computed such that the volume fraction in the system equals unity. Luding [59] calculated α_{fluid} by equating the bulk volume fraction to one as follows,

$$\alpha_{fluid} = 0.0477R^* \tag{3.73}$$

For maximum overlaps greater than α^*, elastic stiffness is equal to $\hat{k}_e$ and for smaller maximum overlaps the elastic stiffness is evaluated by Equation (3.74).

$$k_e = k_p + \left(\hat{k}_e - k_p\right)\frac{\alpha_{\max}}{\alpha^*} \tag{3.74}$$

Luding's model contains two functional flaws by which the behaviour of elasto-plastic and adhesive contacts is not realistically simulated. First, contacts break at zero overlap ($\alpha = 0$), regardless of loading or unloading history. This implies that all plastic deformation has been recovered, which is unrealistic since plastic deformation is

permanent. The second issue is with the reloading behaviour at overlaps smaller than α_c. Since the contact unloading is considered to be elastic, the reloading at any point must follow unloading curve up to the point unloading began (α_{max}). For further loading beyond this point, the force should follow the line with slope k_p.

3.4.4.6 Luding's (2008) elasto-plastic and adhesive tangential contact model

Luding [57] considered a linear tangential stiffness, k_t, similar to the linear-spring model (see Section 3.4.1.1). The sliding limit of the tangential force was adopted from the model of Tomas [55], where for an adhesive contact, Coulomb's law is modified by considering a positive contribution of adhesion force,

$$F_{tc} = \mu\left(F_n + k_c\alpha\right) \tag{3.75}$$

In this model, the reference for a contact is no longer the zero force level, but the adhesive force level along $-k_c\alpha$ [57].

3.5 Particle shape

The rotation of spheres is restricted only by frictional forces between the particles and with other surfaces, whereas for irregular particles, rotation is affected by mechanical interlocking in addition to the frictional contacts. For spherical particles only tangential forces result in rotation of particles and normal contact forces do not contribute to the moment and rotation, since they always act through the centre of the spheres. This is not the case for irregular particles for which the rotation can be as a result of both normal and tangential forces [60]. Therefore spheres may not be a good representative for irregular particles in some cases. It has been shown that spherical particles tend to have

a smaller angle of repose [61] and a reduced strength [62] as compared to non-spherical particles. Cleary [63] considered four major ways by which spherical particles differ from real irregular particles:

1. Material shear strength: particle assemblies of irregular particles show resistance to shear forces due to mechanical interlocking at the single particle level.
2. Dilation during shear: irregular particles tend to produce dilated bulk due to their volume of revolution.
3. Voidage distribution: spherical particles pack very efficiently, but irregular particles mostly produce porous bulk.
4. Partitioning of energy between translational and rotational motions is completely different for spherical and irregular particles.

There exist a number of approaches through which non-sphericity of particles can be taken into account. These approaches are reviewed in the following sections.

3.5.1 **Reduction of rotational freedom of spheres**

Amongst all 3D shapes, spheres require the simplest method of contact detection in which a contact can be detected if the distance between two adjacent spheres becomes less than the sum of their radii. Another advantage of spheres is the efficient and accurate evaluation of the contact overlap, which provides fast and reliable calculation of contact forces. Due to these attributes of spheres, it is always of interest to simulate the particulate systems using spheres. In order to represent irregularity of particles while using spheres, Morgan [64] proposed a damped sphere rotation as a proxy for mechanical interlocking of irregular particles. It was shown that restricting the rotation of particles by this method can yield more realistic values of assemblage friction

compared to free rolling spheres. Ng and Dobry [65] fixed rotation for spherical particles in order to represent the shape of real particles. A simulation of a drained monotonic triaxial compression test in which particle rotation is inhibited, showed higher shear strength, greater stiffness, stronger dilation and better experimental agreement compared to the case of free rolling particles. Another approach is based on considering a rolling friction that provides a threshold torque beyond which angular motion is allowed. Iwashita and Oda [66] showed that in the biaxial compression test, development of shear bands can only be simulated when the rolling friction is considered. It was also reported that by considering the rolling resistance in DEM simulations, high gradient of particle rotation along the shear band boundaries can be reproduced in a manner similar to those of natural granular solids. In order to reduce the rotational freedom of spheres, the centre of mass of the spheres can also be moved away from the geometric centre.

Although it has been reported that introducing rolling resistance and replacing the geometrical centre of mass lead to higher shear strength of the bulk, many believe that higher strength of bulk solids with irregular particles principally arises from the mechanical interlocking of particles which may not be well represented by rolling friction or spheres with a modified centre of mass [63].

3.5.2 **Clumped spheres**

In this method, particle shape is approximated by a number of overlapping or touching spheres with different sizes whose centres are fixed in position relative to each other. The advantage of this method is that it provides an approximation of the actual

irregularity while maintaining computational efficiency and accuracy of spheres. It must be noted that this advantage comes at the expense of increased total number of spheres, which increases the computational cost of the simulations [60]. Theoretically any particle shape can be modelled, however highly angular particles require a large number of small spheres to approximate their sharp edges. Therefore this method is not suitable for these sort of shapes [67]. Approximation of shapes with this technique mostly produces inadvertent surface roughness for the modelled particles [68]. The induced roughness can be controlled by increasing the number of spheres while the computations are within a reasonable range of complexity.

Kodam *et al.* [69] investigated the influence of the forces generated by each component sphere using a simple case in which a particle collides with a flat wall. It was shown that when a clumped-spheres particle contacts a flat wall, the component sphere stiffness should not be the same as the master sphere contact stiffness. If the same stiffness is used in the clumped-sphere model, then the contact becomes effectively stiffer. The optimal values of the component sphere stiffness depend upon the number of component spheres contacting the wall simultaneously and the degree of overlap for each component sphere contact. Kruggel-Emden *et al.* [70] showed that the results for the clumped-spheres method strongly depended on the alignment of the particles. These studies demonstrate that great care must be taken when using the clumped-spheres approach to modelling non-spherical particles in DEM simulations.

Favier *et al.* [67] used this method to model discharge of ellipse-shaped particles through an orifice in a flat-bottomed hopper. Also, the process was simulated using

spherical particles. There was a good agreement between simulations of ellipse-shaped particles and physical flows for the rate of discharge and the vertical velocity profiles. The spherical particles had agreement with simulated and experimental ellipse-shaped particles in frequency of arch formation and orifice diameter.

3.5.3 **Polyhedral shapes**

The geometry of polyhedrons is defined in terms of corners, edges and faces; the location of corners is given by a series of vectors from the centre of mass and a unit outward normal vector is associated with each face. The location and orientation in space of each polyhedron is defined by the components of a vector to the centre of gravity (with respect to a fixed reference frame) and by the principal axes of inertia of the body. The advantage of this type of shape is that complex flat-faced particles can be very accurately approximated (Figure 3.27) [71].

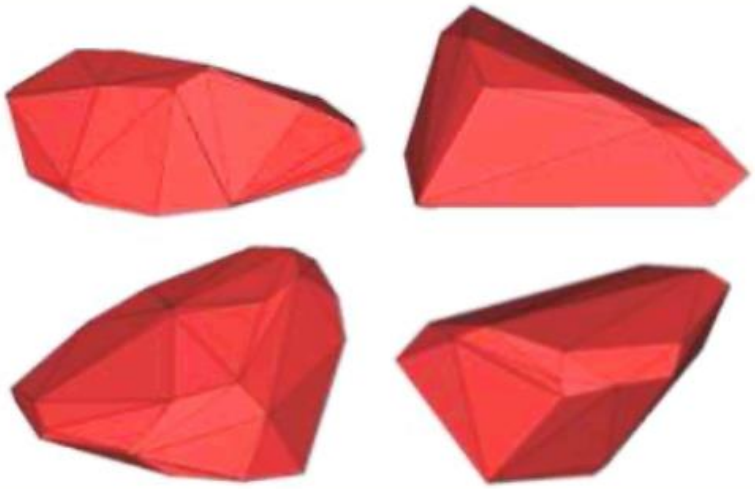

Figure 3.27: Polyhedral-shaped particles [71]

During a simulation, the co-ordinates of each corner and face need to be recomputed each time the collision detection algorithm is used. This is the main limitation which requires massive computational power to calculate these coordinates for each individual particle. For calculations of contact force, contacts are divided into two main types; corner-to-face and edge-to-edge contacts. There exist a number of force evaluation methods for these two types of contact. Mostly a linear contact model based on stiffness is used. The stiffness varies for edge-to-edge and corner-to-face contacts. Applications of linear contact models for polyhedral shapes have not been verified yet. Contact detection involves calculation of distance between all edges of a particle with all the faces of the surrounding particles which again increases the computational complexity of the simulations. This approach is not applicable for smoothly curved shapes since a large number of corners and edges are required to approximate curvatures [72].

Smith *et al.* [73] simulated triaxial compaction of polyhedral particles using an energy-based elastic contact model. It was concluded that the evolution of coordination numbers and the number of contact groups depended strongly upon particle shape.

Recently, a combination of polyhedra and spheres have been introduced to model complex curved shapes. These shapes also allow for simulations of spheres and irregular particles together. Spheropolyhedra (Figure 3.28) are obtained as Minkowski sums of polyhedra and spheres [74].

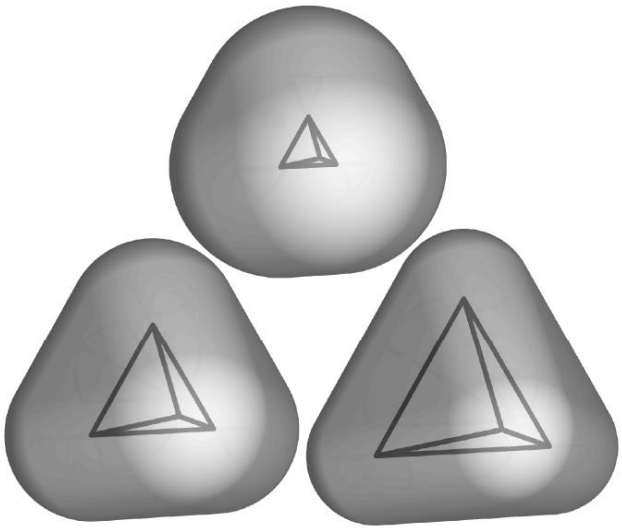

Figure 3.28: Spheropolyhedra [74]

Alonso-Marroquin *et al.* [75] simulated quasi-static biaxial compression of spheres (with varying rolling friction) and spherotetrahedrons. The results suggested that spherical particles with rolling friction capture some effects of particle shape, but some modes of collapse of force chains in highly anisotropic particles cannot be reproduced with rolling friction alone.

3.5.4 **Continuous super-quadric function**

Smooth irregular shaped particles can also be represented by using one or more continuous functions to describe the surface of a particle. Super-quadrics are mathematical shapes that can be generated using the following equation [63],

$$\left(\frac{x}{a}\right)^m + \left(\frac{y}{b}\right)^m + \left(\frac{z}{c}\right)^m = 1 \tag{3.76}$$

where the power *m* determines the roundness or blockiness of the particle shape. The ratios *b/a* and *c/a* define the aspect ratio of the shapes and control whether they are

elongated or platey or roundish. Figure 3.29 shows a range of shapes that can be generated by this method.

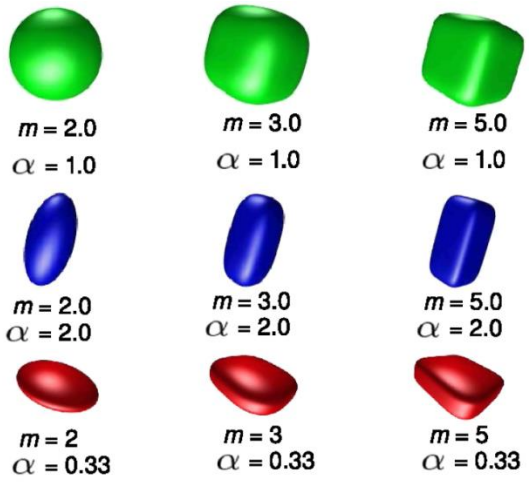

Figure 3.29: Super-quadric shapes [76]

Contact detection between two super-quadric shapes can be determined from the intersection of the two functions. Due to the nonlinearity of the equations, this process is computationally expensive, though more efficient than polyhedra. Similar to polyhedral, the lack of a well-defined contact model for this shape type is the main disadvantage.

3.5.5 **Discrete function representation (DFP)**

Solving the nonlinear equations in a continuous function shape can be avoided by discretising the boundary of the mathematical shape. This will allow for the contact detection to calculate distances between nodes of the discretised elements. It must be noted that discretisation affects the smoothness [72]. By enhancing the discretisation the smoothness can be approximated; however, this will increase the computational

complexity of contact detection. With DFP, super-quadrics perform better compared to polyhedral shapes [63].

3.5.6 **Digitisation**

Jia *et al.* [77] developed a method in which complex shapes are digitised and represented by 3D pixels (voxels). The digitisation is computationally efficient and complex shapes can be approximated quite accurately by increasing pixel density. Digitisation translates each of the particles into a coherent collection of pixels as shown in Figure 3.30.

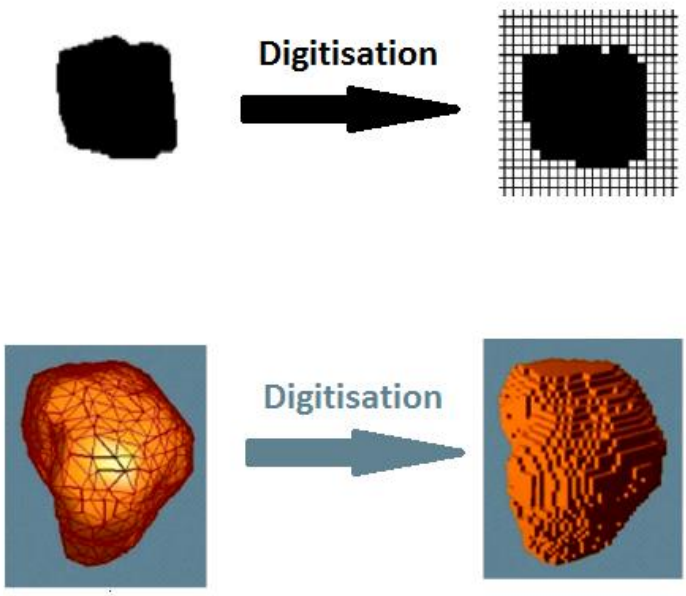

Figure 3.30: 2D and 3D digitisation of shapes [77]

A contact is detected if one pixel is occupied by two or more particles. The overlaps can be accurately and efficiently calculated using the digitised pixels. The time taken to check overlaps is a linear function of the particle number and does not increase with the complexity of particle shapes which makes this technique preferable compared to other

shape representations in terms of computational complexity. Contact force between pixels is not yet fully defined. By considering random movements for particles, this technique can be used to model packing of particles with complex shapes in to complex geometries. Modelling of particulate systems in which particle contacts and collisions dominate the flow, is not achievable at the present time

CHAPTER 4 A New Linear Model for Elasto-Plastic and Adhesive Contacts in DEM

Rigorous non-linear models of elasto-plastic contact deformation are time-consuming in numerical calculations for DEM and quite often unnecessary for representing actual contact deformation of common particulate systems. Simplifications can be made in order to reduce the computational complexity of the models, whilst ensuring the accuracy of capturing the realistic behaviour of contact interactions. In this chapter a new linear model for elasto-plastic and adhesive contacts is described, which is based on the model of Thornton and Ning [31]. The motivation behind proposing a new linear contact model is that available rigorous models such as the model of Thornton and Ning [31] are difficult to be implemented as computer codes [78]. Additionally these models, due to their complexity, lead to slow simulations.

4.1 Normal contacts

Considering the contact of two spherical bodies, Figure 4.1 shows schematically the normal force-overlap response of the proposed model.

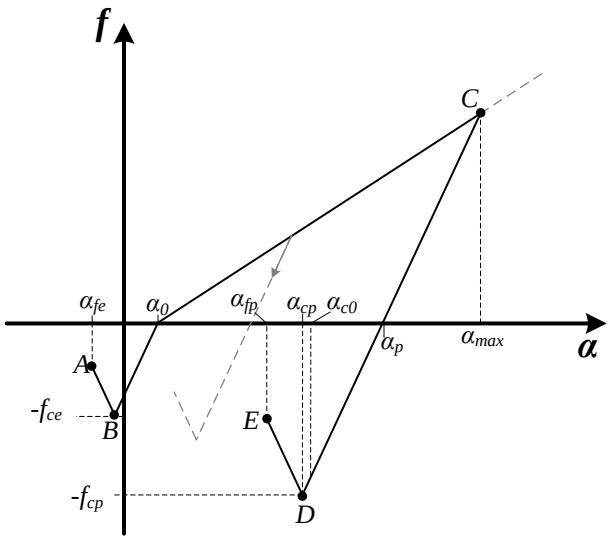

Figure 4.1: Normal force-overlap response of the proposed model. The governing equations are: $F_n = -k_e\alpha - 10/9 f_{ce}$ from *A* to *B*, $F_n = k_e\alpha - 8/9 f_{ce}$ from *B* to α_0, $F_n = k_p(\alpha - \alpha_0)$ from α_0 to *C*, $F_n = k_e(\alpha - \alpha_p)$ from *C* to *D*, and $F_n = k_e(2\alpha_{cp} - \alpha_p - \alpha)$ from *D* to *E*

Initially the contact is assumed to be elastically deforming prior to reaching the compressive state (from point *A* to α_0), after which the plastic deformation is initiated. The initial elastic deformation is considered to be a linear version of JKR: once the contact is established at $\alpha = 0$, the contact force is immediately dropped to a tensile force (see Section 3.4.3.1), which is equivalent to $8/9 f_{ce}$, where f_{ce} at point *B* is the JKR elastic pull-off force given by Equation (4.1),

$$f_{ce} = \frac{3}{2}\pi R^* \Gamma \tag{4.1}$$

where Γ is the interface energy and R^* is the reduced radius. The contact is assumed to be elastically deforming from point *A* to point *B* with an elastic stiffness, k_e. The contact force for this part of deformation can be evaluated using Equation (4.2),

$$F_n = k_e\alpha - \frac{8}{9}f_{ce} \tag{4.2}$$

Since the deformation is elastic, the unloading curve follows the same path. When, during unloading, the normal overlap becomes zero (intersect of the response with force-axis), all the work done during the loading stage has been recovered. However at this point the sphere remains adhered to the target and further work (known as work of adhesion) is required to separate the surfaces. The contact breaks at a negative overlap, α_{fe}, with the contact force being 5/9 f_{ce}. For overlaps larger than α_0 the contact deformation is fully plastic and it is governed by the plastic stiffness, k_p, where the contact force can be evaluated using Equation (4.3),

$$F_n = k_p\left(\alpha - \alpha_0\right) \tag{4.3}$$

The unloading curve from point *C* to point *D* lies on a line with the elastic stiffness k_e. The equation for this line is given by,

$$F_n = k_e\left(\alpha - \alpha_p\right) \tag{4.4}$$

where α_p is the overlap at which the unloading force becomes zero i.e. the amount of plastic deformation. The unloading path continues until a maximum tensile force (f_{cp}), known as the pull-off force, is reached. The calculation of f_{cp} is provided later in this chapter. For unloading beyond the pull-off force from point *D* to point *E*, a negative elastic stiffness, $-k_e$, is considered. The governing equation for this part of contact force can be evaluated as follows,

$$F_n = k_e\left(2\alpha_{cp} - \alpha_p - \alpha\right) \tag{4.5}$$

where α_{cp} is the overlap at which the pull-off force is achieved (see Figure 4.1). The contact is considered to break at point *E* at an overlap which provides a force equivalent

to $5/9f_{cp}$ similar to the JKR theory. Deformations expressed by Equations (4.4) and (4.5) are reversible i.e. reloading follows the path of unloading. If the particles come towards each other after the contact is broken (but while $\alpha > 0$), the contact is considered to be established at α_{fp}. This behaviour is different from the one which Thornton and Ning [31] considered for their elasto-plastic and adhesive contact model (see Section 3.4.4.1 and [31, 44]). In their model, the unloading part of the contact was considered to follow the JKR equation with a reduced local contact curvature due to plastic deformation, α_p. Therefore, in their model, if the particles come towards each other after the contact is broken, the contact is considered to be established at α_{c0} (see Figure 3.20), where the contact force is equal to $-8/9f_{cp}$.

4.1.1 **Load-dependent pull-off force**

In order to account for the increase in the pull-off force due to plastic deformation (i.e. flattening of the contact area), the pull-off force (i.e. the maximum tensile force the contact experiences during unloading if the contact is deformed plastically) is evaluated by applying an energy balance: the work of adhesion of the contacts is equated to $A_p\Gamma$, where A_p is the contact area of the plastic deformation and Γ is the interface energy. The plastic deformation, α_{pd}, is,

$$\alpha_{pd} = \alpha_p - \alpha_0 \tag{4.6}$$

The contact area can be estimated as the projected area of a spherical cap with a diameter of $2R^*$ and a cap height of α_{pd} (the coloured area in Figure 4.2).

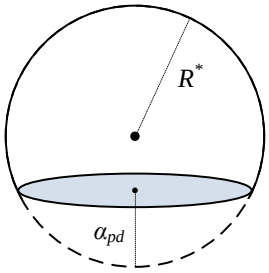

Figure 4.2: Representation of plastic contact area as a spherical cap

The area is calculated by [17],

$$A_p = \pi\left(2R^*\alpha_{pd} - \alpha_{pd}^2\right) \tag{4.7}$$

The work of adhesion can be evaluated using the following equation,

$$W_{ad} = \pi\Gamma\left(2R^*\alpha_p - 2R^*\alpha_0 - \alpha_p^2 - \alpha_0^2 + 2\alpha_p\alpha_0\right) \tag{4.8}$$

The work of adhesion, W_{ad}, is the area under the unloading response from α_{fp} to α_p, which is given by,

$$\left|W_{ad}\right| = \frac{137}{162}k_e\left(\alpha_{cp}^2 - 2\alpha_p\alpha_{cp} + \alpha_p^2\right) \tag{4.9}$$

The derivation of Equations (4.8) and (4.9) is described in detail in Appendix I. By equating the right hand sides of Equations (4.8) and (4.9), an equation for α_{cp} can be derived (see Appendix I),

$$\alpha_{cp} = \alpha_p - \sqrt{\alpha_p^2 - C} \tag{4.10}$$

where C is given by,

$$C = \frac{162}{137k_e}\left(\left(\frac{137}{162}k_e + \pi\Gamma\right)\alpha_p^2 - 2\pi\Gamma\left(R^* + \alpha_0\right)\alpha_p + \pi\Gamma\alpha_0^2 + 2\pi\Gamma R^*\alpha_0\right) \tag{4.11}$$

Figure 4.3 shows the elastic JKR and the proposed model's pull-off forces as functions of α_{cp} for the case where k_e = 1500 N/m, k_p = 210 N/m, Γ = 0.02 J/m^2 and R^* = 2.45 μm. These values were selected to aid comparison with Thornton and Ning's and Luding's

models, as described in Section 4.1.5. The reason why the pull-off force is plotted against α_{cp} is that it shows the locus of the pull-off force in a contact behaviour which is used to further simplify the model in Section 4.1.4.

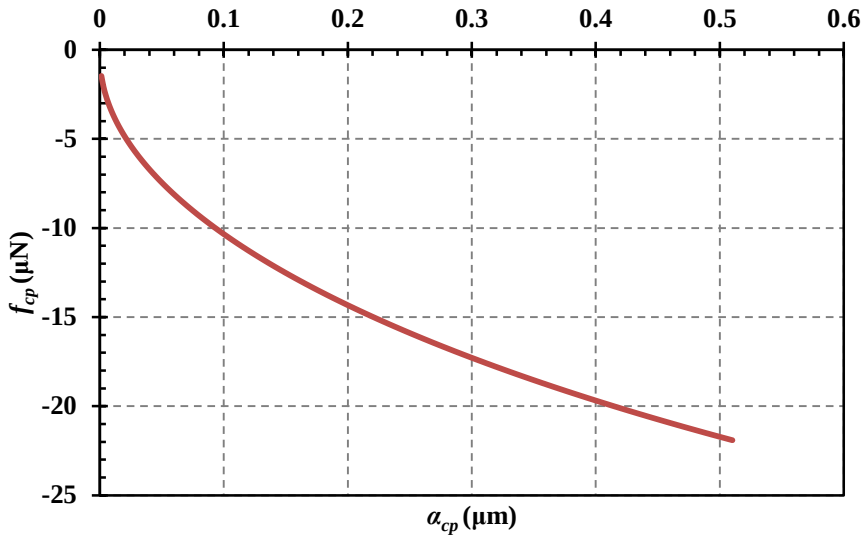

Figure 4.3: The proposed model's pull-off forces as a function of α_{cp}

Figure 4.3 shows that the pull-off increases with plastic deformation, an observation which also has presence in the elasto-plastic and adhesive models of Thornton and Ning [31], Tomas [55], and Luding [57]. The pull-off force is obviously always larger than the JKR elastic pull-off force. In fact, f_{cp} is a function of k_e, k_p, Γ and α_{max}, for which a direct equation based on these parameters could not be derived. In the following sections, the sensitivity of the plastic pull-off force to these parameters is investigated.

4.1.2 **Sensitivity of plastic pull-off force to contact properties**

Figures 4.4-4.7 show the normalised pull-off force (i.e. f_{cp} / f_{ce}) as a function of normalised α_{cp} (i.e. α_{cp} / R^*) for different values of the interface energy, elastic stiffness,

plastic stiffness and reduced radius, respectively. For all cases the fixed properties are as follows: k_e = 1500 N/m, k_p = 210 N/m, Γ = 0.02 J/m^2, and R^* = 2.45 μm.

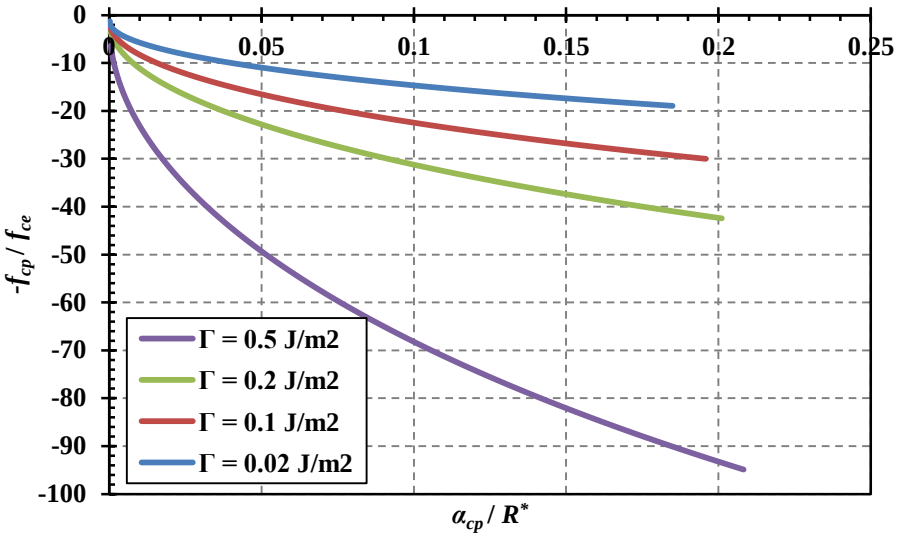

Figure 4.4: Normalised pull-off force as a function of normalised α_{cp} for different interface energies

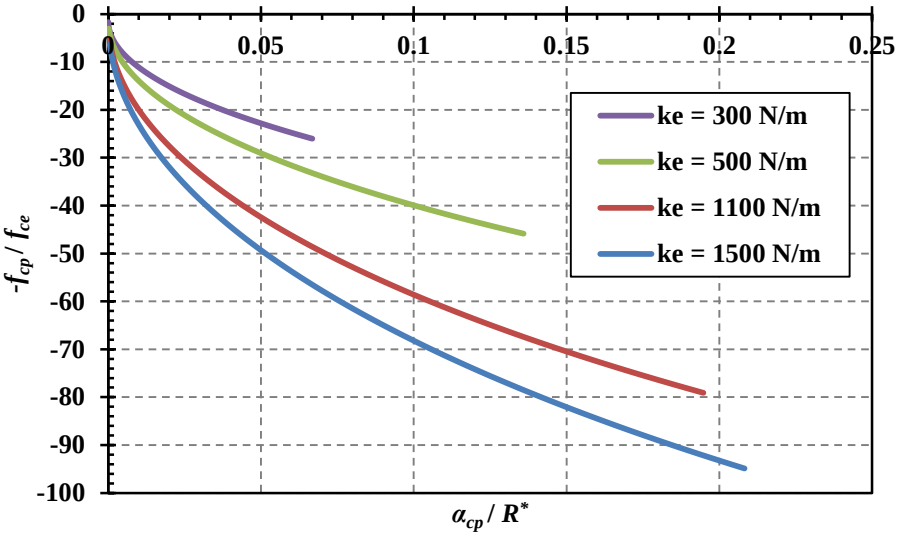

Figure 4.5: Normalised pull-off force as a function of normalised α_{cp} for different elastic sitffnesses

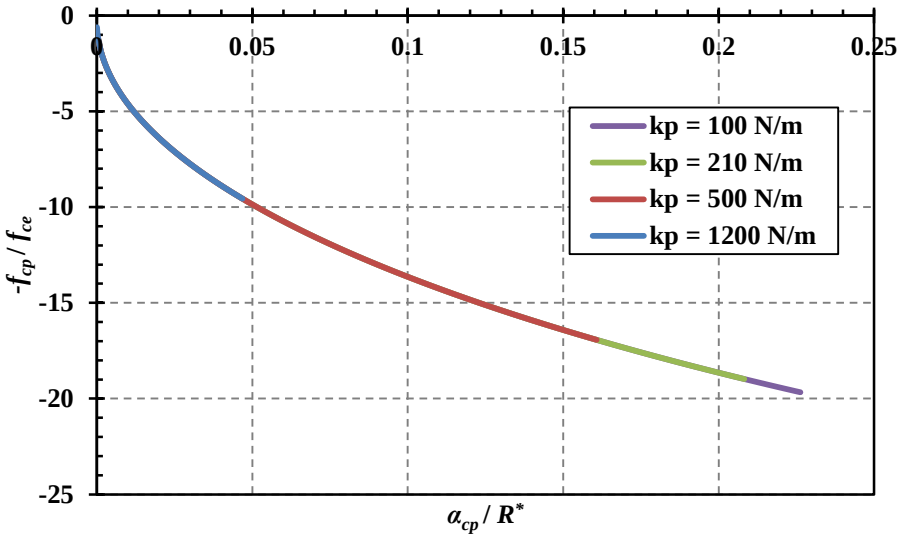

Figure 4.6: Normalised pull-off force as a function of normalised α_{cp} for different plastic stiffnesses

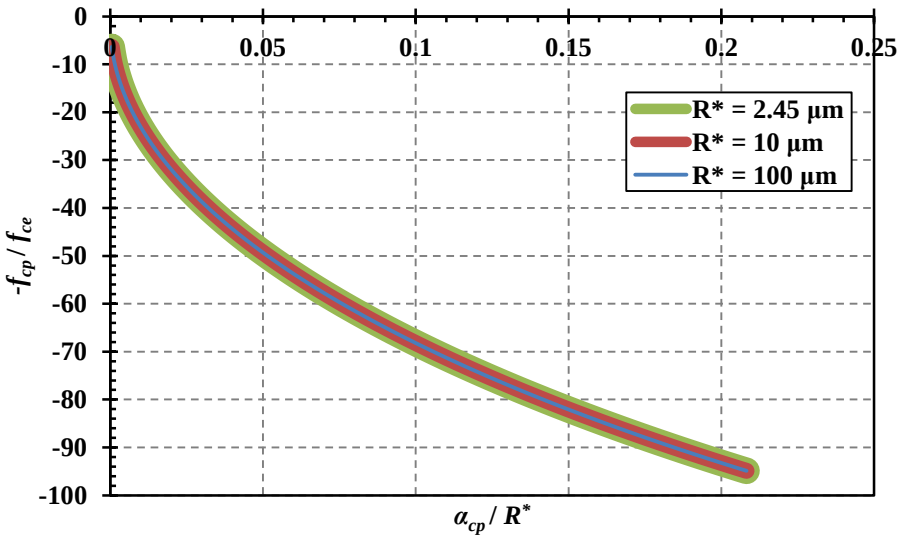

Figure 4.7: Normalised pull-off force as a function of normalised α_{cp} for different reduced radii

As expected, an increase in the interface energy increases the pull-off force sensitivity to plastic deformation (see Figure 4.4).

With an increase in the elastic stiffness, the pull-off force increases. This is due to the fact that higher elastic stiffness results in larger plastic deformation for the same maximum overlap. This is illustrated in Figure 4.8.

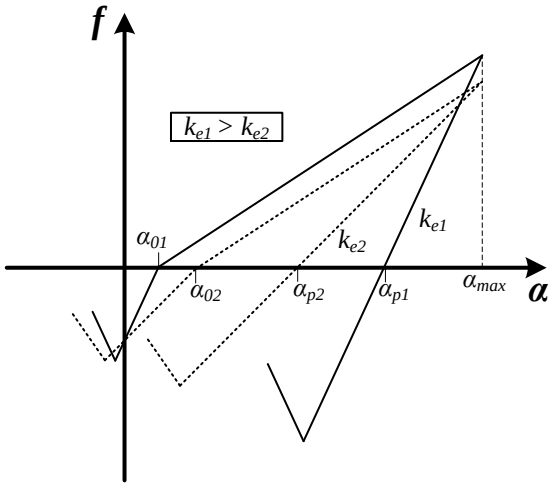

Figure 4.8: Schematic force-overlap response of the proposed model: dotted line correspond to the case with lower elastic stiffness

Since the pull-off force is calculated based on plastic deformation, i.e. $\alpha_p - \alpha_0$, and the plastic deformation increases with the elastic stiffness, the pull-off force increases with elastic stiffness (see Figure 4.5).

The responses for different plastic stiffness lie on each other as can be seen in Figure 4.6. It can be observed that, despite the fact that the responses follow the same

trend, the same pull-off force is achieved at a different maximum overlap, as illustrated in Figure 4.9. Note that in the responses investigated in Figure 4.6, the data was generated for the same range of maximum overlap.

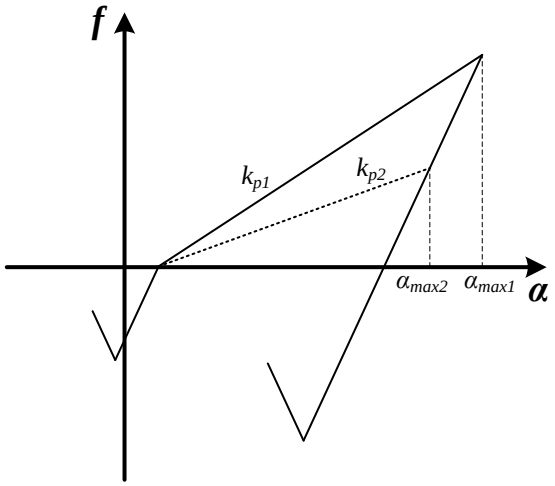

Figure 4.9: Schematic force-overlap response of the proposed model for different plastic stiffness

The plastic pull-off force was found to be independent of reduced radius, according to Figure 4.7.

4.1.3 **Impact, rebound and critical sticking velocities**

In this section, the equations for the impact, rebound and sticking velocities are derived based on applying an energy balance during contact loading and unloading due to the collision of a sphere with a semi-infinite rigid flat target. Figure 4.10 shows schematically the force-overlap response of the proposed model. Different areas under the response, which correspond to different energies, are shaded and coloured.

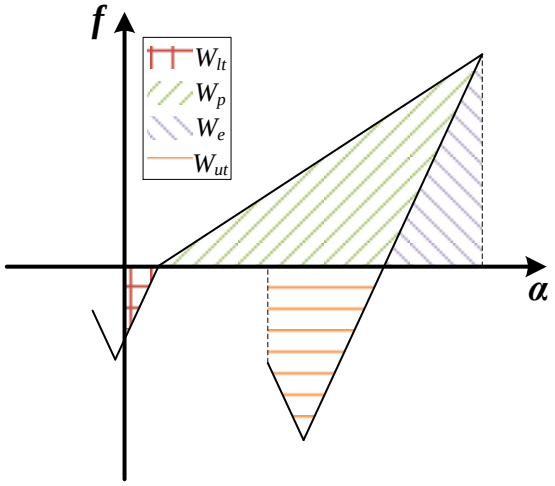

Figure 4.10: Schematic force-overlap response of the proposed model

In Figure 4.10 W_{lt}, W_p, W_e and W_{ut} correspond to the initial loading tensile work, plastic work, elastic work and unloading tensile work, respectively. The impact energy balance from the initial velocity to the point where the sphere is brought to rest, E_i, is,

$$E_i = \frac{1}{2} m v_i^2 = W_p + W_e - |W_{lt}| \tag{4.12}$$

where v_i is the impact velocity. Based on this energy balance, an equation is derived for v_i,

$$v_i = \left(\frac{k_p \left(\alpha_{\max} - \alpha_0 \right)^2 - k_e \alpha_0^2}{m} \right)^{1/2} \tag{4.13}$$

The full detailed derivation of Equation (4.13) is provided in Appendix II. It must be noted that v_i is an independent variable and in fact maximum overlap, α_{max}, is a function of v_i. However by rearranging the parameters, v_i is given as a function of other parameters in Equation (4.13). This enables derivations of equations for critical sticking

velocity, rebound velocity and coefficient of restitution which will be discussed in the following sections.

It is proposed that the critical sticking velocity, v_s, i.e. the maximum impact velocity for which the contact does not break is given by,

$$W_e = |W_{ut}| \quad \rightarrow \quad v_i = v_s \tag{4.14}$$

For impact velocities larger than v_s, the unloading leads to detachment of the contact, as there is sufficient elastic strain energy to overcome the work of adhesion. The rebound velocity, v_r, can be derived based on the following energy balance,

$$E_r = \frac{1}{2} m v_r^2 = W_e - |W_{ut}| \tag{4.15}$$

where E_r is the rebound kinetic energy. The rebound velocity can be derived based on Equation (4.15) (see Appendix II),

$$v_r = \left(\frac{k_p \left(\alpha_{\max} - \alpha_0\right)\left(\alpha_{\max} - \alpha_p\right) - \frac{f_{cp}}{9}\left(-3\alpha_{cp} - 14\alpha_{fp} + 9\alpha_{c0} + 8\alpha_p\right)}{m} \right)^{1/2} \tag{4.16}$$

Figures 4.11-4.14 show the critical sticking velocity, v_s, as a function of interface energy, elastic stiffness, plastic stiffness and reduced radius, respectively. For all the cases the fixed properties are as follow: k_e = 1500 N/m, k_p = 210 N/m, Γ = 0.02 J/m^2, and R^* = 2.45 μm. These conditions have been chosen to facilitate comparison with the model of Thornton and Ning and experimental data reported in the literature (see Section 4.1.5).

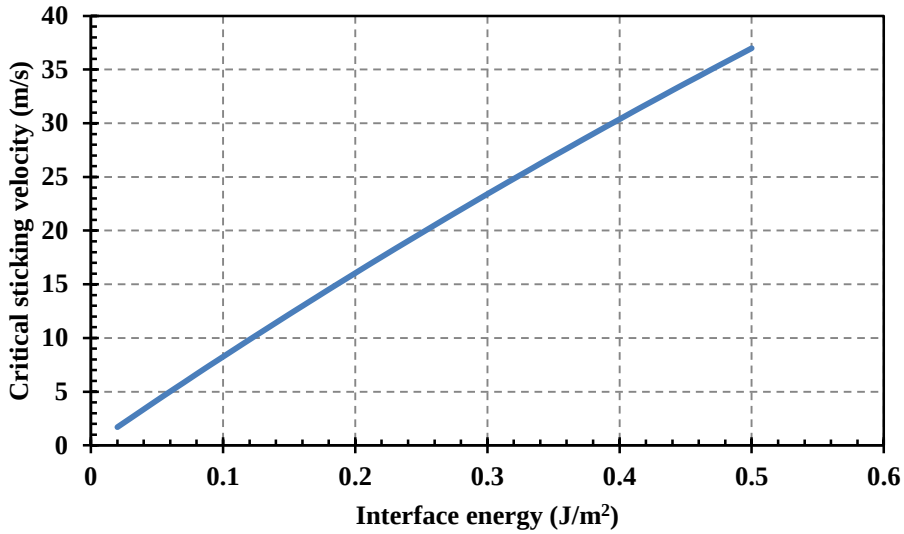

Figure 4.11: Critical sticking velocity as a function of interface energy

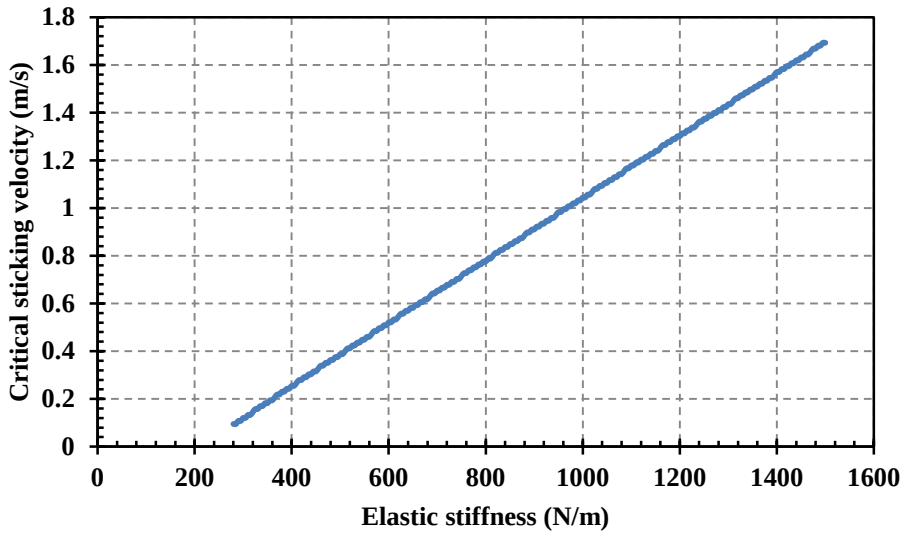

Figure 4.12: Critical sticking velocity as a function of elastic stiffness

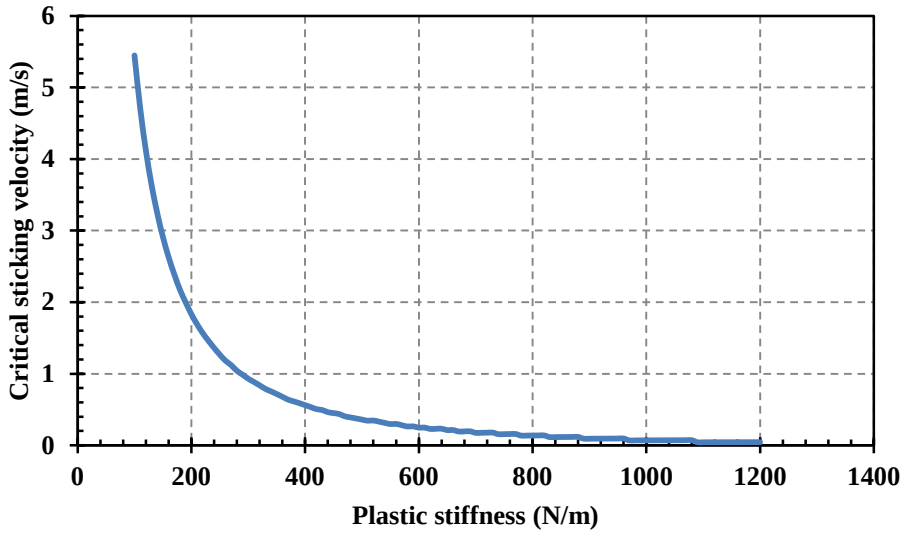

Figure 4.13: Critical sticking velocity as a function of plastic stiffness

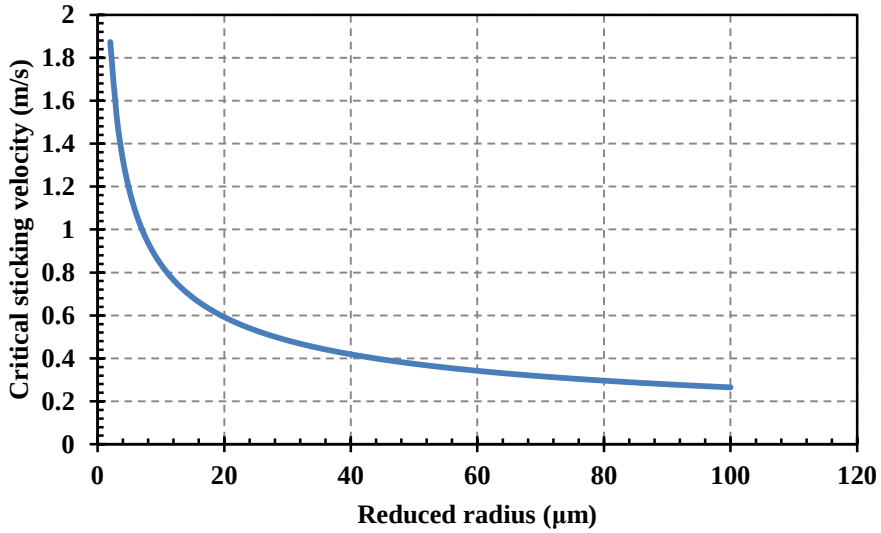

Figure 4.14: Critical sticking velocity as a function of reduced radius

The critical sticking velocity is a linear function of the interface energy and elastic stiffness, but its relationship to plastic stiffness and reduced radius is non-linear. One

way of finding an equation for the sticking velocity based on single particle properties, i.e. elastic and plastic stiffness, interface energy and reduced radius, is to determine the best fit equations to responses in Figures 4.11-14.

The critical sticking velocity increases with increasing the interface energy since the work of adhesion is increased and larger elastic strain energy is required to break the contact. By increasing the elastic stiffness, the unloading elastic work is decreased and therefore there is a reduction in the elastic strain energy. In order to compensate for this, a larger impact velocity is required to provide a sufficiently large elastic strain energy to break the contact. This explains the behaviour seen in Figure 4.12. The critical sticking velocity decreases with an increase in the plastic stiffness or reduced radius. Figure 4.13 shows that the critical sticking velocity decreases with increasing the plastic stiffness. This is due to the fact that by increasing the plastic stiffness while keeping the elastic stiffness unchanged, the elastic strain energy is increased for a given contact force.

Figures 4.15-4.18 show the coefficient of restitution as a function of impact velocity for different values of interface energy, elastic stiffness, plastic stiffness and reduced radius, respectively. In all cases the fixed properties are as follow: k_e = 1500 N/m, k_p = 210 N/m, Γ = 0.02 J/m^2, and R^* = 2.45 μm.

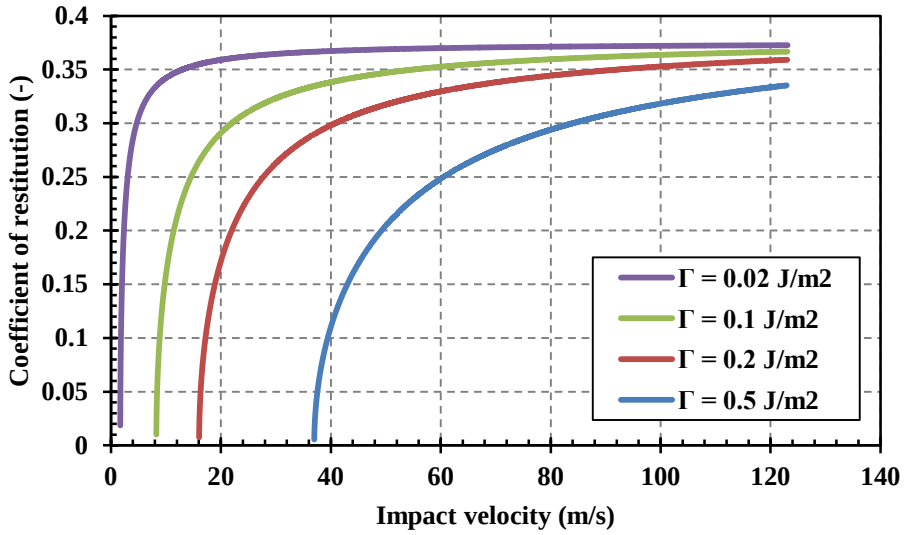

Figure 4.15: Coefficient of restitution as a function of impact velocity for different values of interface energy

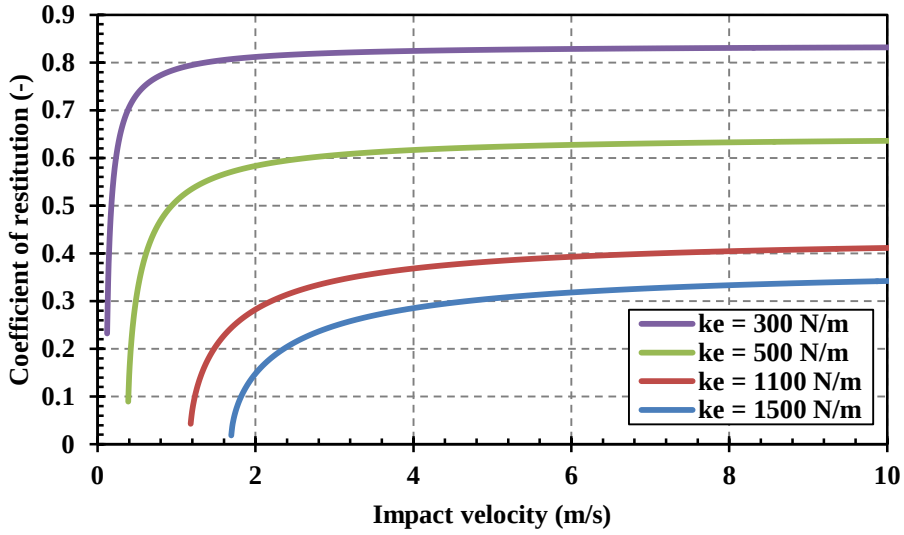

Figure 4.16: Coefficient of restitution as a function of impact velocity for different values of elastic stiffness

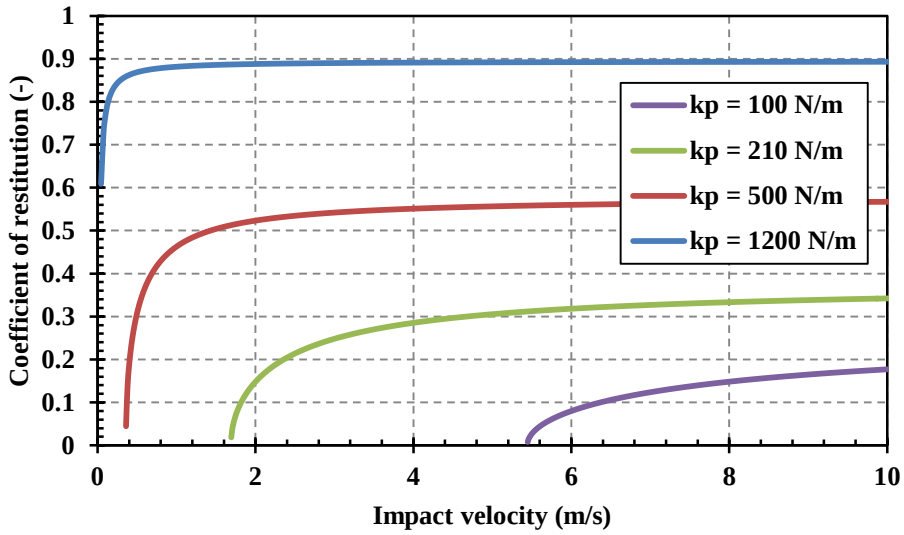

Figure 4.17: Coefficient of restitution as a function of impact velocity for different values of plastic stiffness

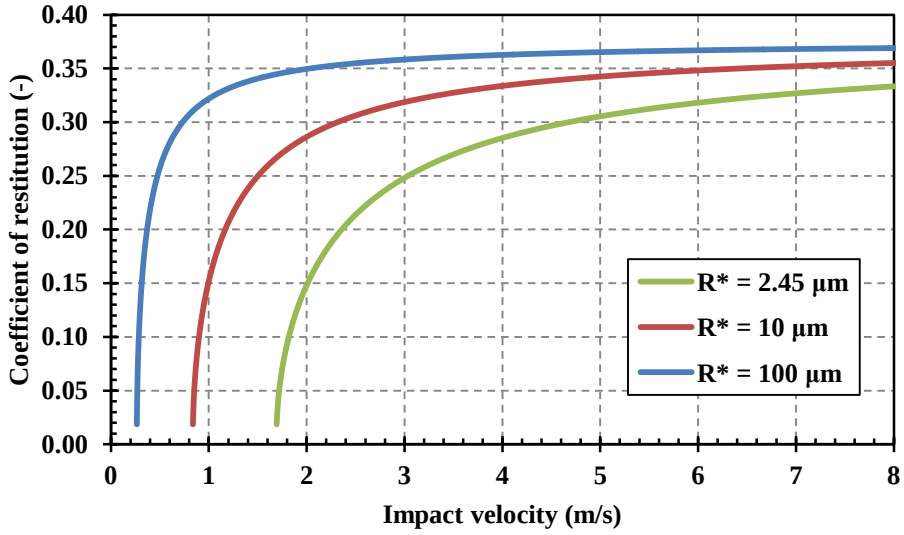

Figure 4.18: Coefficient of restitution as a function of impact velocity for different values of reduced radius

Generally the coefficient of restitution increases with the impact velocity because of adhesive nature of the contact; an observation which was seen in experimental analysis [42]. The coefficient of restitution reaches an asymptote at very high impact velocities. The asymptotic value is a function of contact properties. Increasing the interface energy results in a reduction of the coefficient of restitution since the cohesion is increased. Increasing the elastic stiffness also reduces the coefficient of restitution, since the plastic work and plastic deformation is increased. Increasing the plastic stiffness increases the coefficient of restitution, since the contact becomes stiffer and the extent of plastic deformation is reduced. Increasing the reduced radius increases the coefficient of restitution, since the mass of the particles increases, subsequently the impact kinetic energy is increased.

4.1.4 **Linearisation of locus of pull-off force**

Figures 4.3-4.7 showed that the locus of pull-off force is governed by the specific surface energy and the flattened contact area. The locus is governed by an equation which is not linear for very small deformations, yet becomes approximately linear towards large deformations ($\alpha_{cp} > 0.06R^*$ as can be seen in Figures 4.4-4.7). In an attempt to propose a more computationally cost-effective model, the locus of the pull-off force is considered to be a linear fit to the linear part of the locus. Hence,

$$f_{cp} = -k_{cp}\alpha_{cp} - f_{0p} \tag{4.17}$$

where k_{cp} is the slope of the linear fit and f_{0p} is the intersection of the fit with the force-axis. Figure 4.19 shows the pull-off force locus for $\alpha_{cp} > 0.147$ μm (i.e. $\alpha_{cp} > 0.06R^*$)

and the linear fit for different interface energies: k_e = 1500 N/m, k_p = 210 N/m, and R^* = 2.45 μm.

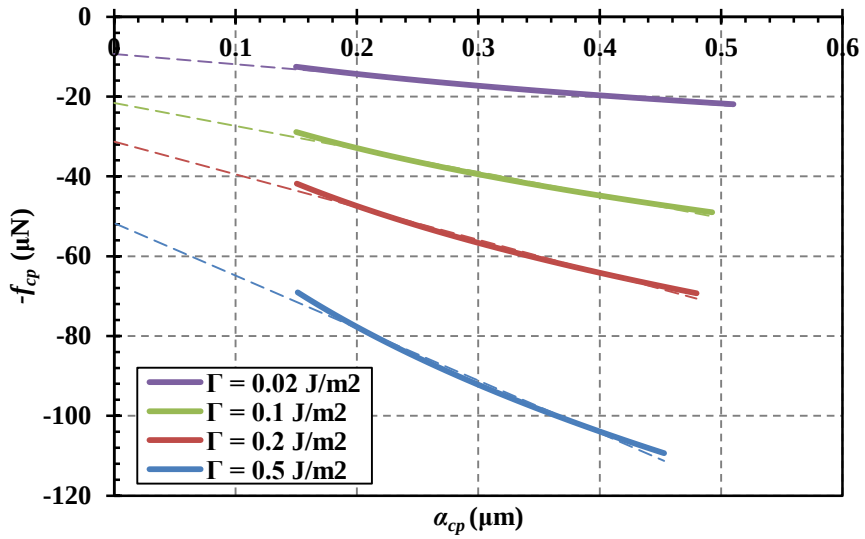

Figure 4.19: Plastic pull-off force as a function of α_{cp} for different interface energy

Furthermore, in a number of cases the initial elastic deformation may be small as compared to the total deformation in which case the model can be simplified further, as it is the case for materials with notable plastic deformation (see Section 3.4.2.3). In real contacts, the presence of asperities always leads to plastic deformation right from the beginning of loading. If the initial elastic deformation is ignored, the force-overlap response can be simplified to the model that is shown schematically in Figure 4.20.

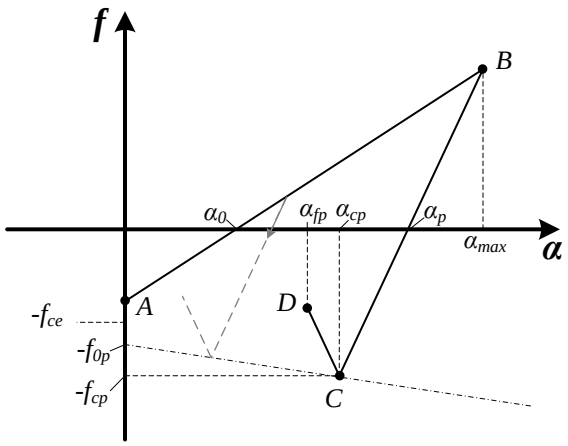

Figure 4.20: Schematic force-overlap response of the simplified model. The governing equations are: $F_n = k_p(\alpha-\alpha_0)$ from *A* to *B*, $F_n = k_e(\alpha-\alpha_p)$ from *B* to *C*, and $F_n = k_e(2\alpha_{cp}-\alpha_p-\alpha)$ from *C* to *D*

4.1.5 Comparison of the proposed model with Luding's, and Thornton and Ning's [15] models

Ning [44] simulated impact of an ammonium fluorescein particle to a silicon target using Thornton and Ning's [31] model. The parameters in their simulations are summarised in Table 4.1.

Table 4.1: Properties of ammonium fluorescein particle and silicon wall used in Ning's [44] simulations

Property	Particle	Wall
Radius (μm)	2.45	-
Density (kg/m^3)	1350	1350
Elastic modulus (GPa)	1.2	182
Poisson's ratio (-)	0.3	0.3
Interface energy (J/m^2)	0.2	
Contact yield pressure (MPa)	35.3	

The force-overlap response at three different impact velocities was obtained by Ning [44] which is shown in Figure 4.21.

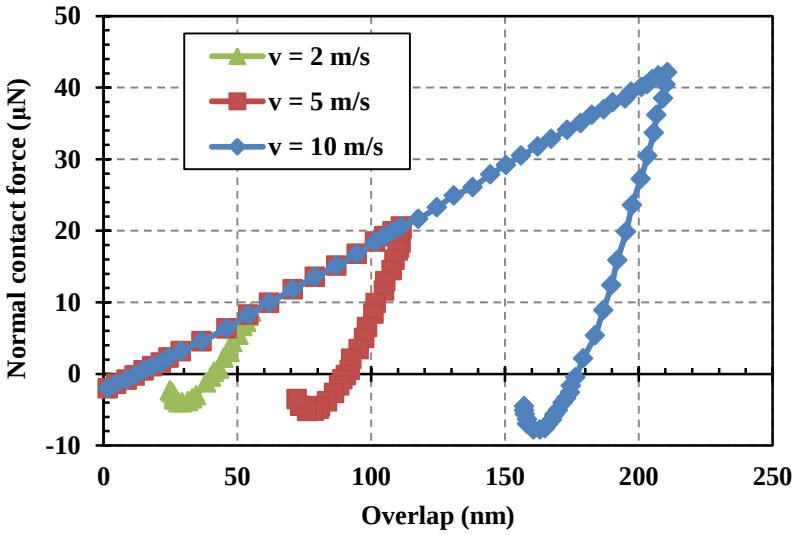

Figure 4.21: Normal force-overlap response of impact of an ammonium fluorescein particle to a silicon target using Thornton and Ning's model with three different impact velocities [44].

PlotDigitizer [79] software is used to digitise the response in their published work and reproduced as Figure 4.21. In order to simulate the same system with Luding's and the proposed linear models, the elastic, plastic and adhesive stiffnesses are evaluated by determining the slopes of the responses in Figure 4.21. The values are summarised in Table 4.2.

Table 4.2: Model parameters obtained by determining the slopes of the responses in Figure 4.21

Property	Value
k_e (N/m)	1500
k_p (N/m)	210
k_{cp}, k_c (N/m)	20
f_{01}, 8/9 f_{ce} (μN)	2.1
f_{0p} (μN)	4.0

It is noteworthy that the elastic stiffness, k_e, in Table 4.3 is the average value of the initial unloading slopes in Figure 4.21. Luding's and the proposed models were implemented as subroutines for EDEM® software provided by DEM-Solutions, Edinburgh, UK. The model with linear pull-off force locus is considered in these analyses. The contact breakage is considered to be at zero force for this model, i.e. at α_{fp} the contact force is zero; this provides easier implementation of the model as a computer code. It will be shown later on that this simplification does not have any significant effect on the contact behaviour. Using the parameters in Table 4.2, a 2.45-μm radius particle was simulated impacting a flat wall at three impact velocities; 2, 5 and 10 m/s. The response using the proposed simplified model is shown in Figure 4.22.

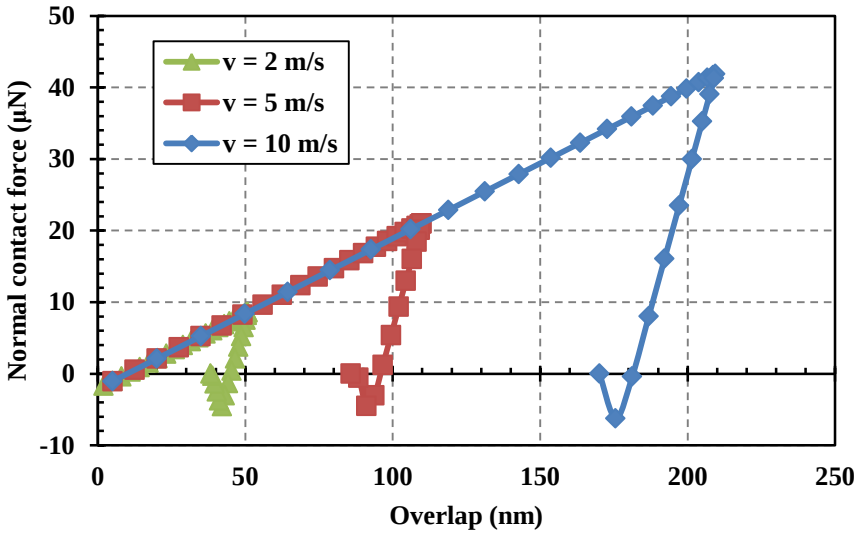

Figure 4.22: Normal force-overlap responses of impact of a 2.45-μm radius particle to a wall with the parameters in Table 4.2 using the proposed simplified model for three different impact velocities.

Comparing Figures 4.21 and 4.22 shows a good agreement between the proposed model and the one of Thornton and Ning in terms of maximum overlap and permanent plastic deformation at different impact velocities. In contrast to this agreement, using Luding's model, the particle did not detach from the wall with impact velocities of 2, 5 and 10 m/s. Figure 4.23 shows the contact force-overlap response of the system using Luding's model with three different impact velocities that led to detachment. The maximum elastic stiffness, $\hat{k}_e$, and the dimensionless plasticity depth, ϕ_f, were set to 1500 N/m and 0.02, respectively in these simulations. The critical sticking velocity in Luding's model provided a maximum overlap which was larger than α^*, hence the unloading elastic stiffness was constant for the impact velocities of 15 - 25 m/s. The plastic flow limit overlap, α^*, was indeed very small (with the dimensionless plasticity depth of 0.02,

α^* is equal to ~ 0.114 μm). For the dimensionless plasticity depths larger than 0.0412, there was always a finite rebound velocity despite extensive plastic deformation.

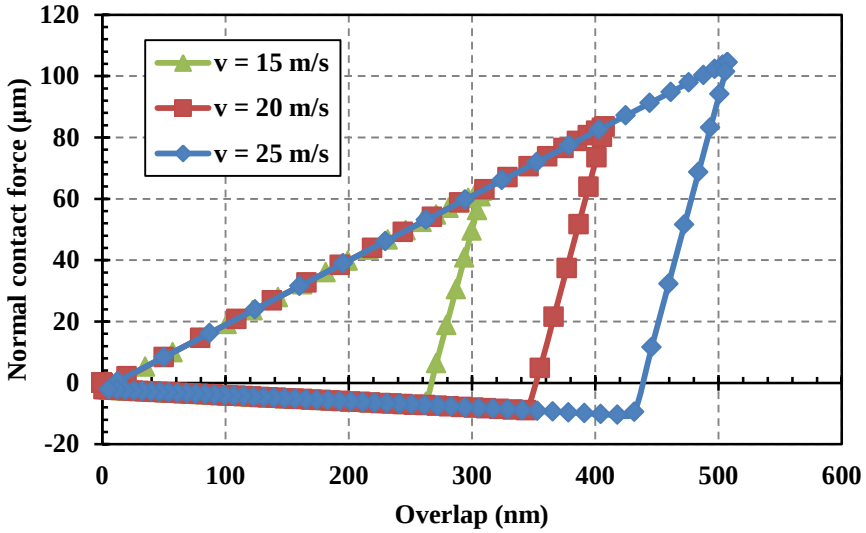

Figure 4.23: Normal force-overlap responses of impact of a 2.45-μm radius particle to a wall with the parameters in Table 4.2 using Luding's model for three different impact velocities.

The critical sticking velocity was found to be approximately 13.8 m/s. This is due to the fact that with Luding's model, the adhesive work (the negative area under the curve) is much larger compared to that of the proposed and Thornton and Ning's model. It is noteworthy that with an impact velocity of 13.8 m/s, the maximum overlap is approximately 12% of the particle radius. The impact velocity by which the contact breaks can be evaluated by applying a work balance, in a manner similar to Section 4.1.3.

In order to provide a more in depth comparison, the coefficient of restitution as a function of impact velocity is compared for a range of impact velocities. The results of the coefficient of restitution for the 2.45 μm radius ammonium fluorescein particle impacting on the silicon target obtained by simulations using Luding's and the proposed models are compared with findings of Ning's [3] in Figure 4.24. The data for Thornton and Ning' model were obtained by digitisation of their published work [31].

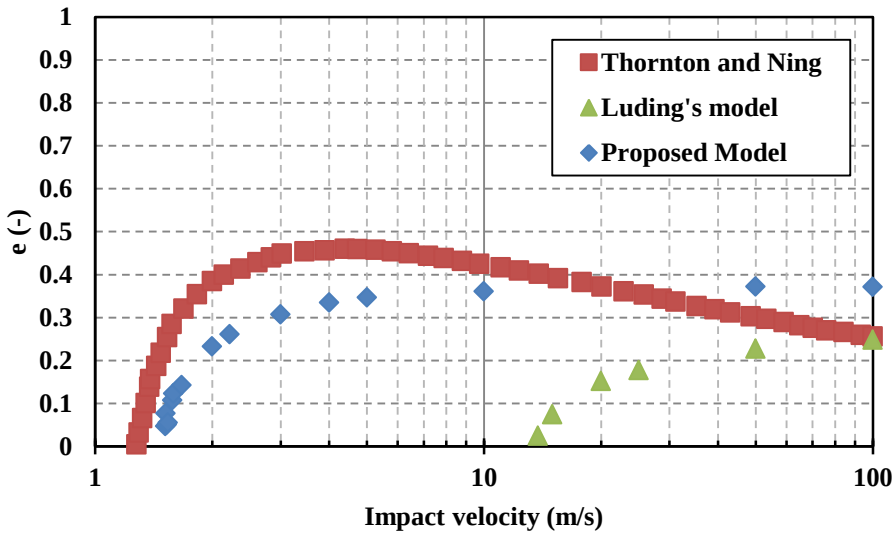

Figure 4.24: Coefficient of restitution as a function of impact velocity using different contact models for a 2.45-μm radius ammonium fluorescein particle impacting to a silicon target.

Figure 4.24 shows a better agreement between the proposed model and the one of Thornton and Ning compared to Luding's model. With the proposed model, the coefficient of restitution initially increases however it reaches an asymptotic value of ~0.38 for impact velocities larger than ~6 m/s. The minimum impact velocity which

provides detachment in the proposed model is very similar to the one of Thornton and Ning (~1.6 m/s). Thornton and Ning's results show that the coefficient of restitution starts reducing for impact velocities larger than ~ 10 m/s, at which the maximum overlap is ~8.5% of the particle radius. For larger impact velocities the overlap becomes comparable to particle size, at which point DEM simulations are not realistic due to large deformations. Figure 4.24 also shows that the minimum impact velocity that results in particle detachment in Luding's model is much larger compared to that of the proposed model and Thornton and Ning's, 13.8 m/s compared to 1.6 m/s.

In order to verify the energy balance equations in Section 4.1.3, the analytical equation for the coefficient of restitution as a function of impact velocity is obtained for Luding's and the proposed simplified models and is compared to the simulation results of Figure 4.24. The impact velocity of Luding's and the simplified models can be obtained by Equation ,

$$v_i = \left(\frac{k_p}{m} \left(\alpha_{\max}^2 - 2\alpha_0 \alpha_{\max} \right) \right)^{1/2} \tag{4.18}$$

For full detailed derivation of Equation (4.18) see Appendix III. The rebound velocity can be calculated using Equations (4.19) and (4.20) for Luding's and the simplified models, respectively (see Appendices II and III).

$$v_r = \left(\frac{F_{\max}}{m} \left(\alpha_{\max} - \alpha_p \right) - \frac{f_{cp}}{m} \left(\alpha_p - \alpha_{fp} \right) \right)^{1/2} \tag{4.19}$$

$$v_r = \left(\frac{F_{\max}}{m} \left(\alpha_{\max} - \alpha_p \right) - \frac{8}{9m} f_{ce} \alpha_p - \frac{f_{cp}}{m} \alpha_{fe} \right)^{1/2} \tag{4.20}$$

where α_{fe} is the overlap at which the unloading contact force is equal to $-8/9f_{ce}$. The coefficient of restitution is analytically calculated for a range of impact velocities. The analytical results (dotted lines) are plotted alongside the simulated results in Figure 4.25.

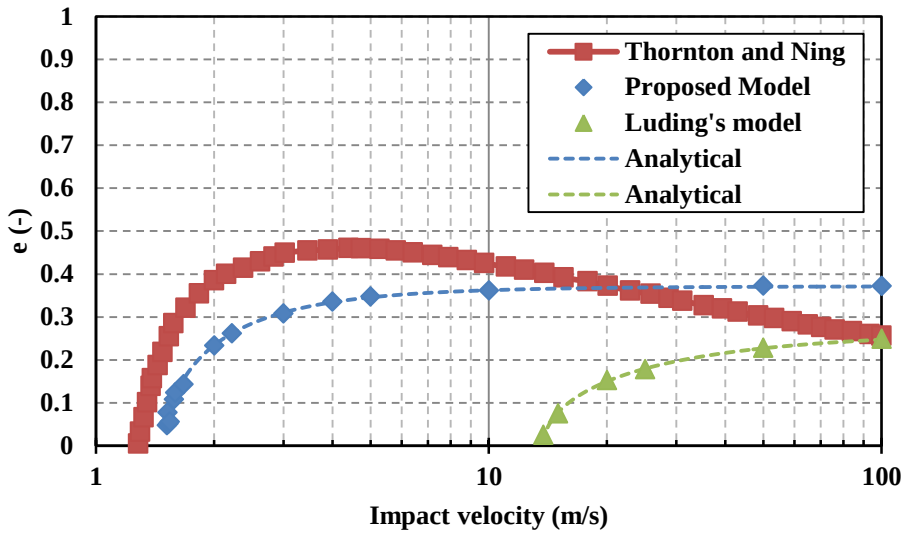

Figure 4.25: Coefficient of restitution as a function of impact velocity using different contact models for a 2.45-μm radius ammonium fluorescein particle impacting to a silicon target. The dashed lines are obtained analytically using Equations (4.19) and (4.20).

Since the simulations results of Luding's and the proposed model lie on the analytical curves, it can be concluded that the energy balance considerations are correct.

The reason for the asymptotic response of the coefficient of restitution at high impact velocities with the proposed model is attributed to a constant elastic stiffness, for which the ratio of elastic work (W_e) to plastic work (W_p) is always constant. At very high

impact velocities, the elastic strain energy becomes very large relative to the work of adhesion (W_{ut}), so elasto-plastic process dominates since the plastic-cohesive stiffness, k_{cp}, is normally smaller than the plastic stiffness, k_p. Hence the asymptote has a value of $(k_p/k_e)^{1/2}$ [14]. This asymptotic behaviour is not in line with the experimental evidence [80, 81]. In order to account for a decreasing coefficient of restitution at high impact velocities, the elastic unloading stiffness must be made load-dependent. Now, considering that the stiffness increases proportionally with the contact area, which in turn is a function of the maximum overlap, α_{max}, the stiffness, k_e, is given by,

$$k_e \propto r^2 = 2R^*\alpha_{\max} - \alpha_{\max}^2 \tag{4.21}$$

where r is the contact radius. Assuming the maximum elastic stiffness, $\hat{k}_e$, is at an overlap of R^*, then

$$k_e = \left(\frac{r}{R^*}\right)^2 \hat{k}_e \tag{4.22}$$

For very small deformations, Equation (4.22) gives elastic stiffness values which can be smaller than the plastic stiffness. In order to avoid such values for k_e, following the approach of Luding [57] as per Equation (3.74), Equation (4.22) can be modified as follows,

$$k_e = k_p + \left(\frac{r}{R^*}\right)^2 \left(\hat{k}_e - k_p\right) \tag{4.23}$$

The maximum elastic stiffness can be evaluated by finding the tangent to the Hertz response of the contact and finding the best match to the Hertz curve for unloading. For the values given in Table 4.1 and Table 4.2, a maximum elastic stiffness of 13000 N/m provided the closest agreement with the Hertz analysis.

The coefficient of restitution as a function of impact velocity is shown in Figure 4.26 for the proposed model with a load-dependent elastic unloading stiffness. This response is obtained by the same energy balance approach as described in Section 4.1.3. The prediction from Thornton and Ning's model is also given for comparison.

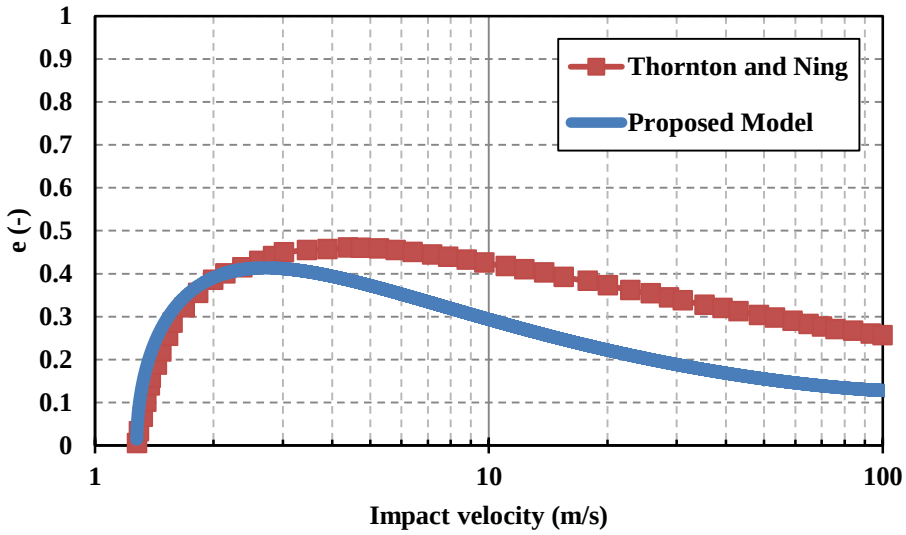

Figure 4.26: Coefficient of restitution as a function of impact velocity using the proposed model with a load-dependent unloading stiffness and Thornton and Ning model.

As expected a decreasing coefficient of restitution is observed at high impact velocities, although showing a deviation form Thornton and Ning's model. It must be noted that the increasing elastic stiffness is not capped here, unlike Luding's approach, where the elastic stiffness for overlaps larger than α^* is capped. Limiting the elastic stiffness is not physically sound since, based on the Hertz non-linear theory, the elastic stiffness increases sharply with deformation at high loads for an elastic sphere.

Using Luding's model with increasing elastic stiffness without capping resulted in zero rebound velocity and hence zero coefficient of restitution for impact velocities ranging from zero to a value that provided a deformation equal to R^*. The data in Figures 4.23-4.25 for Luding's model were obtained for the case where the elastic stiffness was capped at $\hat{k}_e$ for overlaps larger than α^*. New experimental data are needed to check the validity of models predictions, as a larger data set than that available for ammonium fluorescein particles would provide more certaintity.

4.2 Normal contact damping

The normal damping force is a function of normal relative velocity, v_r, of the two particles in contact. The general equation for mass-spring systems is adopted here for normal damping force [57],

$$F_{nd} = \beta \upsilon_r \tag{4.24}$$

where β is the viscous damping given by Equation (4.25) ,

$$\beta = \sqrt{\frac{4\ln^2(e) m^* k_n}{\ln^2(e) + \pi^2}} \tag{4.25}$$

where e is the coefficient of restitution, m^* is the equivalent mass of the two particles in contact and k_n is the 'instantaneous' normal contact stiffness. During the initial elastic loading and throughout the elastic unloading $k_n = k_e$ and during the plastic loading $k_n = k_p$.

4.3 Tangential model

For tangential force calculation, a linear tangential stiffness, k_t, similar to the linear-spring model is considered. Therefore the tangential force is evaluated as follow,

$$F_t = k_t \alpha_t \tag{4.26}$$

where α_t is the tangential displacement. The sliding limit of the tangential force is adopted from the models of Tomas [55], Luding [57] and Thornton and Yin [46]. In all the aforementioned models a positive contribution of the normal contact force in addition to contribution of the adhesive force is considered for defining the sliding limit. Tomas [55] and Luding [57] stated that the reference for the contact is no longer the zero force level, but the adhesive force level along the locus of the pull-off force. The adhesive contribution in the proposed model is assumed to be $f_{cp} - f_{ce}$, therefore the critical tangential force (sliding limit) is given by,

$$F_{t_c} = \mu\left(F_n + f_{cp} - f_{ce}\right) \tag{4.27}$$

For the simplified version of the model, the sliding limit can also be evaluated as follow,

$$F_{t_c} = \mu\left(F_n + k_{cp}\alpha_n + f_{0p} - f_{ce}\right) \tag{4.28}$$

4.4 Sensitivity analysis of the proposed model parameters

A set of simulations are carried out in order to investigate the effects of the model parameters on the elastic and plastic components of work during loading and unloading of bulk compression. The simplified version of the proposed model is used. The tangential stiffness, k_t, is equated to the elastic stiffness, k_e, throughout the simulations. The model parameters for the particles are summarized in Table 4.3.

Table 4.3: Model parameter values used in the simulations

Parameter varied	k_p (kN/m)	k_e (kN/m)	Γ
k_e	10	50, 100, 500, 1000	0
k_p	10, 50, 100, 250, 500	1000	0
k_p	50, 100, 500, 1000, 2500	5000	0
$k_e = k_e$	100	100	0
Γ	100	1000	0.05, 0.1, 1, 2, 5

For non-adhesive cases (i.e. when $\Gamma = 0$), the model becomes identical to that of Walton and Braun [41]. For adhesive cases, the plastic-adhesive stiffness, k_{cp}, is kept constant at a value of 5 kN/m. The sensitivity of bulk compression response to the plastic stiffness (k_p) is evaluated with two different fixed values of elastic stiffness (k_e) in order to achieve the same stiffness ratio (k_e/k_p) with different ranges of elastic and plastic stiffnesses. This will facilitate the sensitivity analysis of stiffness ratio as well as sensitivity of elastic and plastic stiffnesses. The walls are considered to be elastic with zero adhesion (i.e. $\Gamma = 0$, $k_{cp} = 0$ and $k_p = k_e = k_t$). The stiffness of the walls is set to be 8000 kN/m. 3400 particles with a mean diameter of 1 mm and a normal size distribution (as shown in Table 4.4) are generated inside a cylindrical die of 12 mm diameter. This number of particles provides a bed height of approximately 36 mm. The density of the particles is set to be 1000 kg/m^3.

Table 4.4: Size distribution of the generated particles

Particle diameter (mm)	Number frequency (%)
0.8	5
0.9	25
1	40
1.1	25
1.2	5

The time-step is calculated based on a mass-spring system and is given by,

$$t = 0.2t_{crit} = 0.2\sqrt{\frac{m^*}{k^*_{crit}}} \tag{4.29}$$

where t_{crit} is the critical time-step for a mass-spring system, m^* is the equivalent mass of the smallest particle given by Equation(4.30), and k^*_{crit} is the largest equivalent stiffness in the system given by,

$$m^* = \frac{m_{\text{smallest}}}{2} \tag{4.30}$$

where $m_{smallest}$ is the mass of the smallest particle in the system.

$$k^*_{crit} = \frac{k_{\text{largest}}}{2} \tag{4.31}$$

where $k_{largest}$ is the largest stiffness in the system. The coefficients of sliding friction and restitution are 0.25 and 0.3, respectively for both the particle-particle and particle-wall contacts. The compression was simulated at a strain rate of 0.28 s^{-1}. In order to define the dynamics of the process, the dimensionless shear strain rate of Tardos *et. al.* [82] is evaluated using following equation,

$$\dot{\gamma} = \gamma \left(\frac{d_p}{g} \right)^{1/2} \tag{4.32}$$

where γ is the shear strain rate, d_p is the mean particle diameter and g is the gravitational acceleration. The strain rate of 0.28 s^{-1} provides a dimensionless shear strain rate of ~ 0.003. It is shown by Tardos *et. al.* [82] that for dimensionless shear strain rates of < 0.15, the process is quasi-static, therefore the inertial effects on the stresses throughout the bulk are negligible. The assembly is compressed by moving the top platen until a bulk strain of 11% (for non-cohesive cases) or a solids fraction of 0.58 (for cohesive cases) is achieved, after which the platen is unloaded with the same speed as during the compression. Figure 4.27 shows a typical force-displacement curve of the top platen during the bulk compression using DEM.

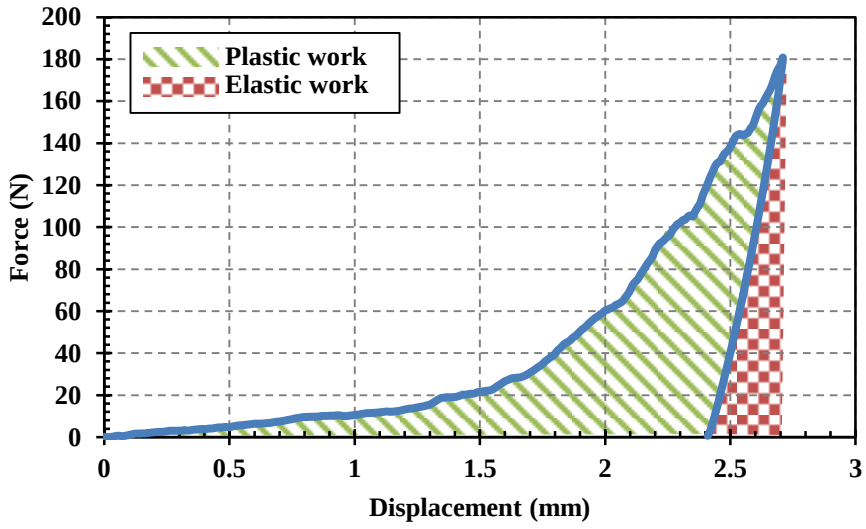

Figure 4.27: Typical loading-unloading curve of compaction (k_p = 10 kN/m and k_e = 50 kN/m)

The plastic work (i.e. irrecoverable work) on loading is calculated as the closed area underneath the curve (the shaded area in Figure 4.27). The elastic work (i.e. recoverable work) is calculated as the area underneath the unloading curve (the hatched area in Figure 4.27). The total input work is the addition of the plastic and elastic work components. The normalised elastic and plastic work component are defined as the elastic and plastic work, respectively, divided by the input work. Figure 4.28 shows the normalised elastic and plastic work components as a function of stiffness ratio, k_e/k_p, for all the cohesionless cases (first 4 rows of Table 4.3).

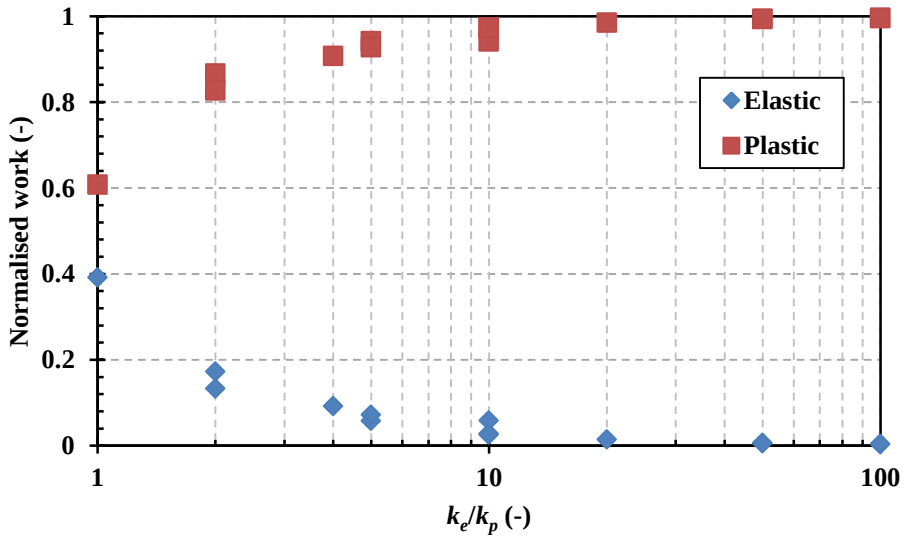

Figure 4.28: Normalised work as a function of stiffness ratio for all the cohesionless cases

Large stiffness ratios imply particles deforming extensively plastically, whereas a stiffness ratio of one implies a purely elastic deformation. For the stiffness ratio of one, the plastic component of the work is still larger than the elastic one. The plastic work in

this case has contributed towards particle rearrangements and frictional forces between the particles and the geometry, since the contacts deform elastically. The graph shows that as the stiffness ratio increases, the fraction of plastic work increases, while that of elastic work decreases. The increase in the ratio means either the plastic stiffness is decreased or the elastic stiffness is increased. If the plastic stiffness is decreased while the elastic stiffness is kept constant (softer particles), more work is expanded in deforming contacts to reach the same force. This leads to an increase of the total work, while the elastic work remains the same. Therefore normalised elastic work decreases and normalised plastic work increases. In the case where the elastic stiffness is increased while plastic work is kept constant, the total input work does not change, but the fraction of elastic work decreases. This leads to a decrease in the normalised elastic work and consequently normalised plastic work increases. It can also be seen from Figure 4.28 that there exists a limit for the stiffness ratio ($k_e/k_p \approx 20$) beyond which almost all of the work input into the system is used in plastic deformation.

Figure 4.29 shows the plastic and elastic works as a function of increasing the interface energy.

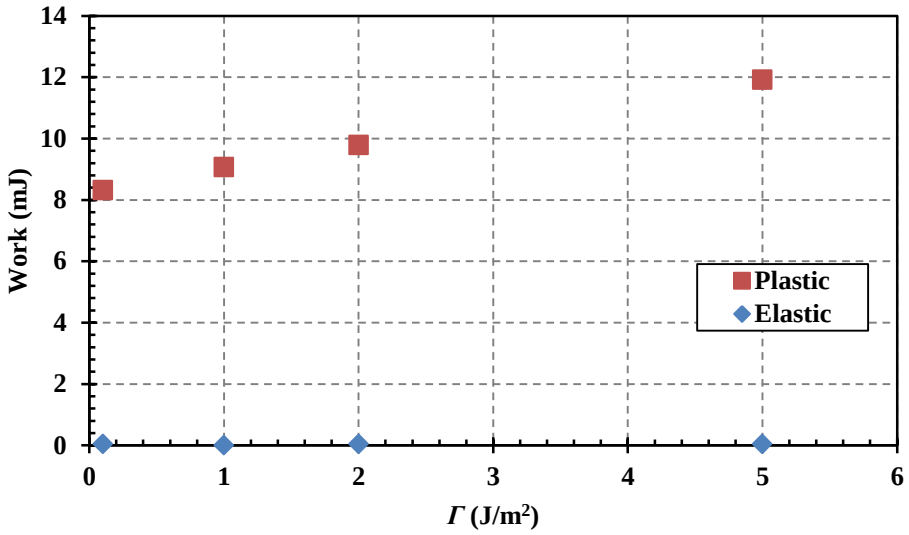

Figure 4.29: Elastic and plastic work components as a function of Γ (k_p = 100 kN/m, k_e = 1000 kN/m)

As it can be seen in Figure 4.29, by increasing the interface energy, the plastic work increases; however the elastic work is very small for the range of Γ investigated here and it does not change significantly with the interface energy. An increase in the interface energy increases the work of adhesion.

4.5 Conclusions

A new linear elasto-plastic and adhesive contact model for spherical particles has been proposed based on improvements of Luding's model and considering aspects of Thornton and Ning's and Tomas's contact models. Plastic deformation of contacts during loading and pure elastic unloading, accompanied by adhesion are considered, for which the pull-off force increases with plastic deformation. Considering the collision of a spherical cohesive body with a rigid flat target, the impact velocity that provides contact breakage in the proposed model is found to be very similar to that of Thornton

and Ning's model. However with Luding's model the contact breaks with a much higher impact velocity. The coefficient of restitution as a function of impact velocity was obtained for the proposed model and Luding's model. The response of the proposed model is in good agreement with the work of Thornton and Ning, however Luding's model underestimated the coefficient of restitution significantly.

Sensitivity analyses of the model parameters on work of compaction reveal that by increasing the stiffness ratio (k_e/k_p) the normalised plastic work increases and the normalised elastic work decreases. By increasing the interface energy, the plastic work increases, however the elastic work does not change significantly. This highlights the flexibility of the model in representing a wide range of particulate materials. The linear nature of the model leads to time efficient simulations whilst still capturing the complex material behaviour.

CHAPTER 5 Numerical Analysis of Minimum Sample Size and Indenter Size Range in Ball Indentation Method by DEM

As discussed in Section 2.3.5, it has been shown by Hassanpour and Ghadiri [4] that under certain circumstances, indentation on a cohesive powder bed by a blunt indenter can give a measure of the resistance to powder flow which is related to flowability. However, the specification of the operation window in terms of indenter size and penetration depth has yet to be fully analysed. In this chapter, the ball indentation process is analysed by numerical simulations using the DEM. The flow resistance of the assembly, commonly termed hardness, is evaluated for a range of sample quantities and operation variables.

5.1 DEM Simulation of the indentation process

5.1.1 Contact models

The calculation of the contact forces of the particles is based on the Hertz analysis for the elastic regime. The adhesion force calculation between the particles is based on a modified version of the theory of Johnson *et al.* [45], referred to as JKR model (see Section 3.4.3.1). Figure 5.1 compares the Hertz elastic model with the JKR and the modified version of the JKR models.

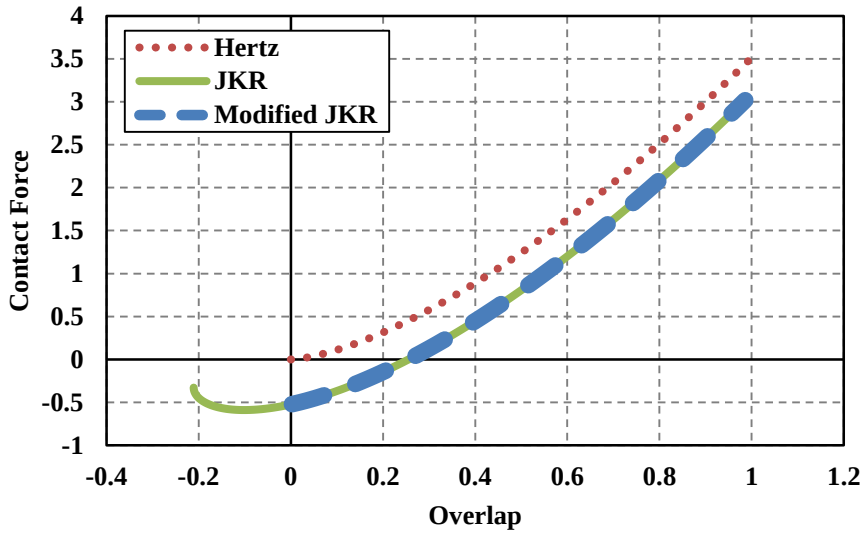

Figure 5.1: Comparison of force-overlap behaviour of Hertz, JKR and modified JKR contact models

In the modified model, at the point of contact, the normal contact force immediately drops to 8/9 of the pull-off force, similar to the JKR model. The particle velocity reduces to zero at a point where the contact force reaches a maximum value and the loading stage is complete. In the unloading stage, the stored elastic energy is released and is converted into kinetic energy which makes the particle move in the opposite direction. All the work done during the loading stage is recovered when the contact overlap becomes zero. Based on the JKR theory, at this point, the spheres remain adhered together and further work is required to separate the surfaces. The modified model does not consider this additional work and the contact for this model breaks once the overlap becomes zero. However the pull-off force required to break the contact is representative of the JKR theory.

For tangential contact force calculations the no-slip solution of Mindlin [34] is used (see Section 3.4.1.4).

5.1.2 **Stress calculation**

In the results section of this chapter, localised stresses amongst the powder bed are evaluated for various operational variables. The approach that Bagi [83] introduced for evaluation of stress in granular assemblies, is adopted here. For a localised measurement volume, the forces acting on each particle whose centre is inside the volume are calculated and the components of the stress tensor within the cell are evaluated as follows,

$$\sigma_{ij} = -\frac{1}{V}\sum_{N_p}\sum_{N_c}\left|x_i^c - x_i^p\right| n_i F_j \tag{5.1}$$

where σ_{ij} is the ij-component of stress tensor, V is the volume of the measurement space, N_p is number of particles in the bin, N_c is the number of contacts around particle p, x_i^c, x_i^p and n_i are the i-components of contact location, particle centre and normal vector directed from a particle centroid to its contact, respectively, and F_j is the j-component of the contact force [83].

The localised hydrostatic and deviatoric stresses are also evaluated in the results section. The governing equations for calculation of the hydrostatic, σ_{hyd}, and deviatoric, τ_D, stresses are Equations (5.2) and (5.3), respectively.

$$\sigma_{hyd} = \frac{\sigma_{xx} + \sigma_{yy} + \sigma_{zz}}{3} \tag{5.2}$$

$$\tau_D = \left(\frac{\left(\sigma_{xx} - \sigma_{yy}\right)^2 + \left(\sigma_{xx} - \sigma_{zz}\right)^2 + \left(\sigma_{yy} - \sigma_{zz}\right)^2}{6} \right)^{1/2} \quad (5.3)$$

This stress calculation is implemented as a subroutine for EDEM® software. For the details of this implementation see Appendix IV.

5.1.3 **Simulation properties**

16000 particles with a mean diameter of 1 mm and a Gaussian size distribution (as shown in Table 5.1) are generated inside a cylindrical die which has a diameter (d_b) of 39 mm.

Table 5.1: Size distribution of the generated particles

Particle diameter (mm)	Number Frequency (%)
0.59	0.33
0.72	3.84
0.81	11.24
0.9	21.00
1.00	27.75
1.10	20.85
1.19	10.95
1.28	3.74
1.41	0.29

The use of a size distribution rather than a mono disperse system, avoids the formation of ordered packing. The material properties are chosen so that they represent glass beads

with a cohesive interaction (Material 1) and stainless steel (Material 2), as summarised in Table 5.2.

Table 5.2: Material properties used in the simulations

Material property	Material 1	Material 2
Young's modulus	55 GPa	182 GPa
Poisson's ratio	0.25	0.3
Density	2456 kg/m^3	7800 kg/m^3

The particles and the indenter are made of Material 1, whereas the cylindrical die and the piston, which is used to consolidate the bed, are made of Material 2. The interaction properties used in the simulations are summarised in Table 5.3.

Table 5.3: Interaction properties used in the simulations

Interactional property	Material 1-Material 1	Material 1-Material 2
Coefficient of restitution	0.50	0.30
Coefficient of sliding friction	0.15	0.0
Coefficient of rolling friction	0.10	0.0
Interface energy	0.50	0.0

In order to avoid the influence of wall friction on the assembly, the coefficients of sliding and rolling friction between the cylindrical die and the particles are considered to be zero. 16000 particles provide a bed height (h_b) of about 13 mm. The particles are generated within the die and allowed to settle under gravity. The assembly is then

consolidated with a piston at a constant strain rate of 1 s^{-1}. In order to define the dynamics of the process, the dimensionless shear strain rate of Tardos *et al.* [82] is evaluated using Equation (5.4),

$$\dot{\gamma} = \gamma \left(\frac{d_p}{g} \right)^{1/2} \tag{5.4}$$

where γ is the shear strain rate, d_p is the mean particle diameter and g is the gravitational acceleration. The strain rate of 1 s^{-1} provides a dimensionless shear strain rate of ~ 0.01. It is shown by Tardos *et al.* [82] that for dimensionless shear strain rates of < 0.15, the process is quasi-static, therefore the effects of the dynamics of the geometries on the stresses throughout the bulk are minimised. For all the simulations, the assembly is pre-consolidated to 10 kPa (σ_{pre} = 10 kPa), as this is within the realistic range of experimental work, where results of other flowability techniques, e.g. uniaxial unconfined compression, have been reported. Once the desired stress is achieved, the piston is unloaded with the same speed as that of the loading. The indentation process is simulated using a cohesionless spherical indenter made of Material 1, and the ball is penetrated at the same constant velocity as of the piston during consolidation. The indenter is a mesh CAD geometry imported into the software in order to facilitate strain controlled motion of the indenter with a fixed speed.

5.2 **Results and discussions**

Figure 5.2 shows the hardness values calculated (see Section 2.3.5 for details of this calculation) for a 13 mm spherical indenter on a bed of cohesive spheres for a range of indentation loads.

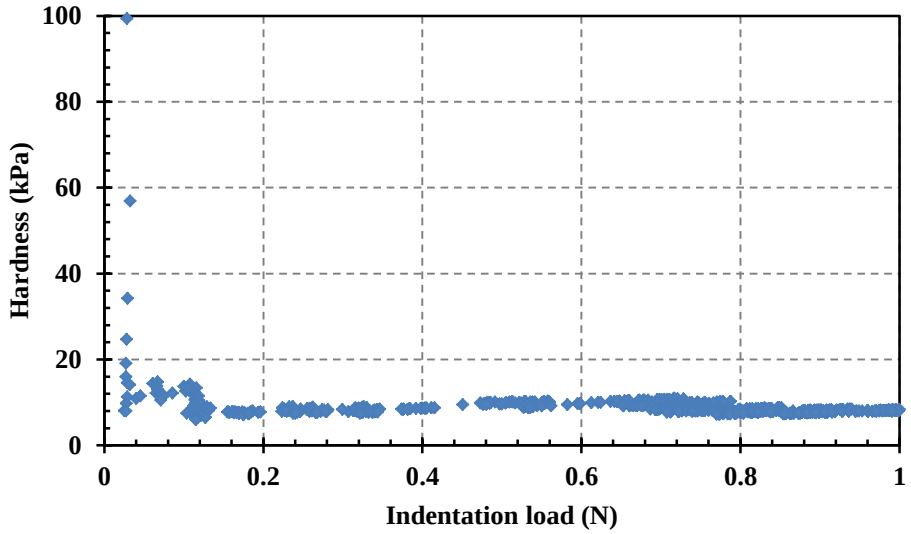

Figure 5.2: Hardness as a function of indentation load (σ_{pre} = 10 kPa, h_b = 13 mm, d_b = 39 mm, d = 13 mm)

At very low indentation loads/penetration depths, high values of hardness are obtained. However, the hardness decreases very rapidly to an asymptotic value. Hardness must be independent of indentation load in order to represent the plastic yield stress. At very small penetration depths, the force on the indenter is due to its interactions with only a few spheres, and hence the calculation of projected area of the impression is not suitably described by Equation (2.9). As hardness is a continuum measure of resistance to plastic deformation, it is necessary to identify a range for indentation load within which a relatively constant value of hardness is obtained. The lower limit of this range should therefore be based on the depth of penetration which initiates plastic flow in the powder bed. The upper limit is affected by the presence of the die wall and the indenter size. The limits of penetration depth are investigated later in this paper for a range of indenter

sizes. In order to compare the results of different indenter sizes, a dimensionless penetration, h_d, as defined by Equation (5.5), is considered.

$$h_d = \frac{h}{r} \tag{5.5}$$

where h is the penetration depth and r is the radius of the indenter. Figure 5.3 shows the hardness against dimensionless penetration for an indenter size of 13 mm and at 10 kPa pre-consolidation pressure. In order to disregard the artificially high values of hardness that occur at the start of the indentation process, the data are presented for dimensionless penetrations greater than that corresponding to one particle diameter.

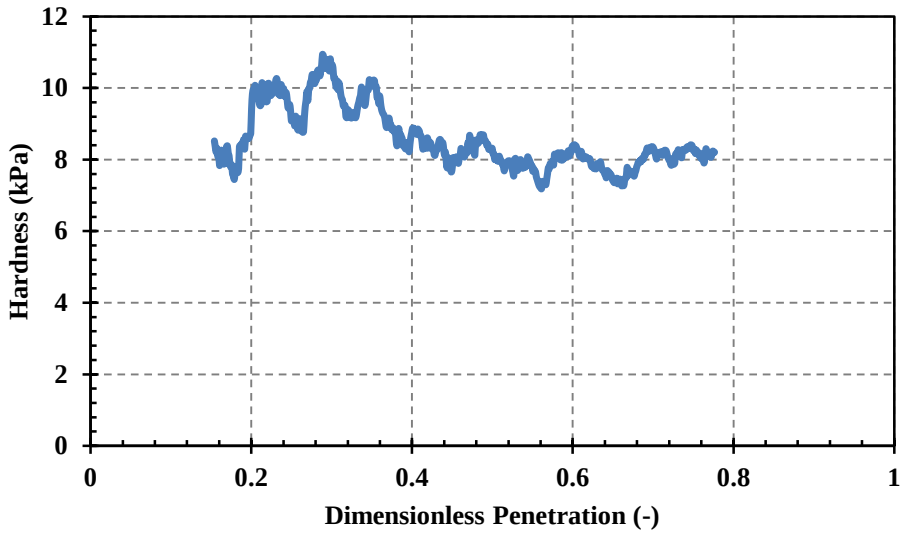

Figure 5.3: Hardness as a function of dimensionless penetration (σ_{pre} = 10 kPa, h_b = 13 mm, d_b = 39 mm, d = 13 mm)

It can be seen that initially there are fluctuations in the hardness value, however, after a dimensionless penetration of about 0.4, the hardness stabilises around 8 kPa. This behaviour can be attributed to the fact that for low penetration depths the plastic flow in

the bed is not fully initiated. Figure 5.4 shows hardness against dimensionless penetration for indenter sizes of 16 and 19 mm.

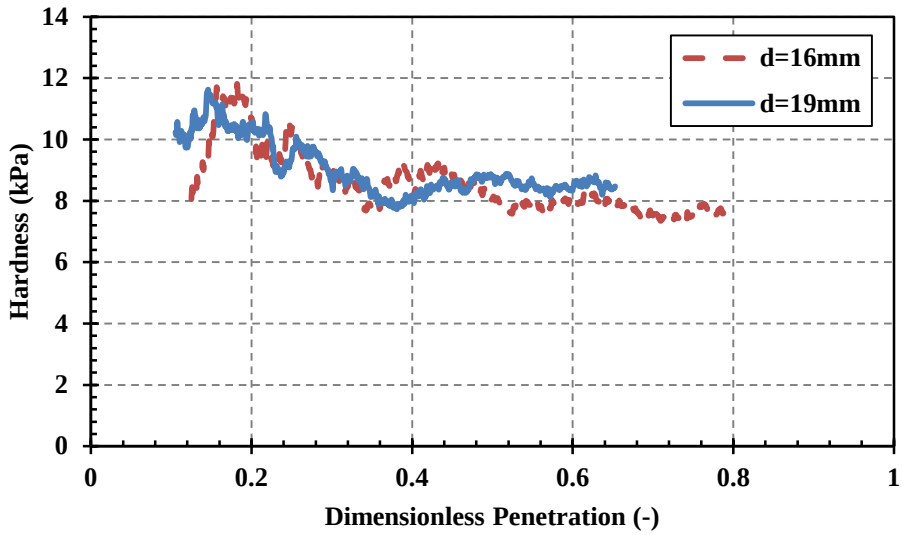

Figure 5.4: Hardness as a function of dimensionless penetration (σ_{pre} = 10 kPa, h_b = 13 mm, d_b = 39 mm)

For these indenter sizes initial fluctuations in the hardness value are also present, but after a dimensionless penetration of about 0.35, the hardness stabilises around 8 kPa. Figure 5.5 shows the hardness against dimensionless penetration for indenter sizes of 7 and 10 mm.

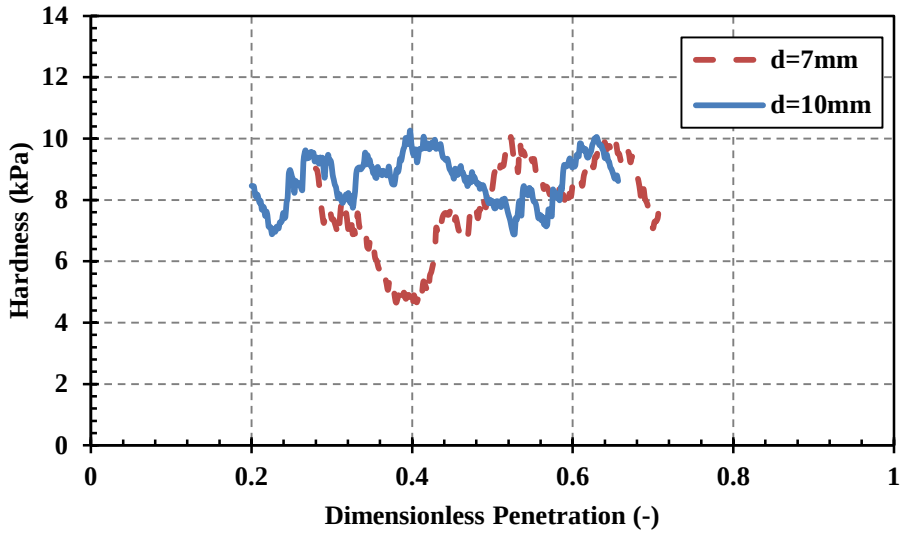

Figure 5.5: Hardness as a function of dimensionless penetration (σ_{pre} = 10 kPa, h_b = 13 mm, d_b = 39 mm)

As it can be seen, the hardness exhibits wider fluctuations than previously observed for the larger indenters within the whole range of penetration depths investigated here. These fluctuations are significantly larger for smaller penetration depths and smaller indenter diameters. As the indenter size decreases, approaching the size of bed particles, particle rearrangements at the single particle level become more prominent and substantially influence the force on the indenter throughout the indentation process, resulting in fluctuations, whereas the number of particle-indenter contacts increases if the indenter size is increased. This leads to a reduction in the fluctuations of force acting on the indenter. Moreover, small indenters may introduce localised consolidation, resulting in measuring a greater hardness. Figure 5.6 shows the hardness against dimensionless penetration for the indenter sizes of 22 and 25 mm.

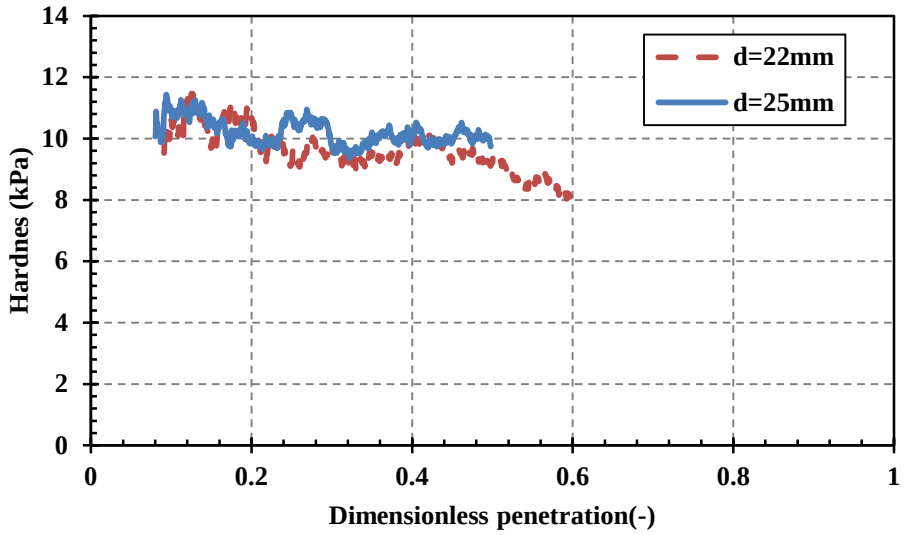

Figure 5.6: Hardness as a function of dimensionless penetration (σ_{pre} = 10 kPa, h_b = 13 mm, d_b = 39 mm)

After initial fluctuations with these larger indenter sizes, the hardness value is stabilised around 10 kPa, which is larger than those measured by smaller indenters (13-19 mm in diameter). With large indenters, the indent size may be affected by the surrounding wall. In order to examine the wall effects with larger indenters, the particle assembly is plotted at three different penetration depths using the 25 mm indenter in Figure 5.7. The grey-scale of each particle in Figure 5.7 indicates its velocity, with lighter particles having negligible velocity.

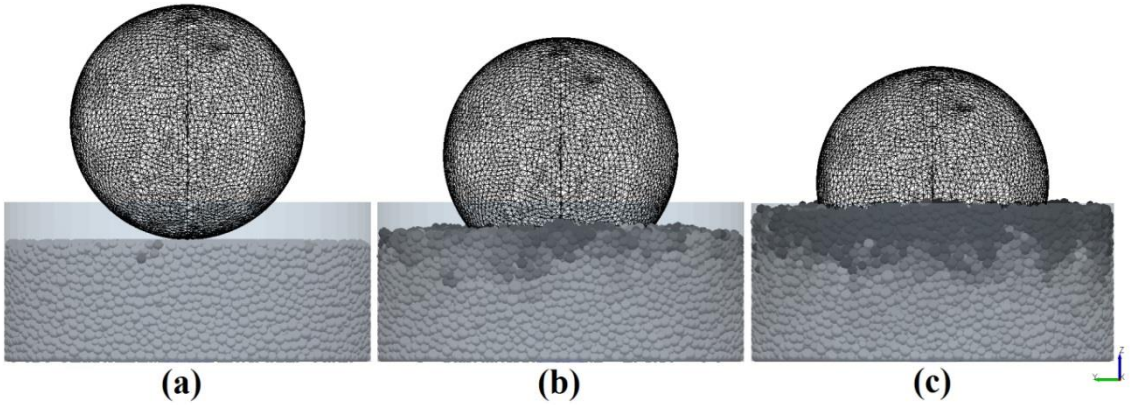

Figure 5.7: Indentation process using the 25 mm indenter (a) h_d = 0.0 (b) h_d = 0.27 (c) h_d = 0.49

It can be seen that the whole bed is deforming during the indentation process at greater penetration depths (Figure 5.7c), as indicated by the particles neighbouring the die wall. The surrounding walls are therefore restricting the bed deformation, which leads to an increase in the resistance of the bed against shear deformation and hence an increase in hardness. In order to investigate the wall effects in more detail, localised stresses and particle velocities are evaluated for various indenter sizes. For this purpose, a cuboid region centrally aligned with the axis in the cylindrical die is considered for the analysis (Figure 5.8a). The cuboid region is divided into 15 bins, each of which has dimensions of 5.2, 5.2 and 4.2 mm in x, y and z directions, respectively (Figure 5.8).

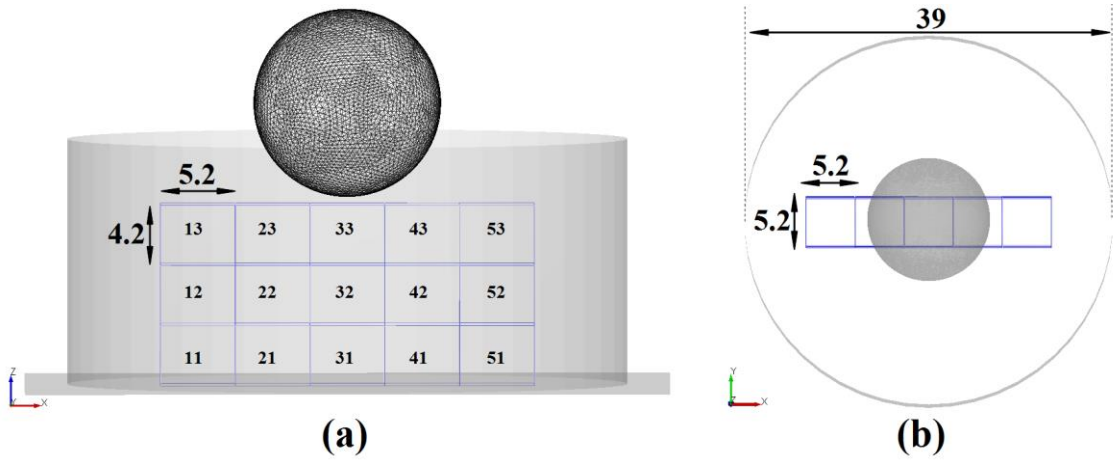

Figure 5.8: Cuboid bins used for localised velocity and stresses analysis: (a) side view (b) plan view (dimensions are normalised by mean particle size, which is 1 mm)

The height of the cuboid region approximates the bed height. This region is not extended to the walls in order to avoid an excessive number of bins. Within each bin, the forces acting on each particle whose centre is inside this cell are calculated and the components of the stress tensor within the cell are evaluated as discussed in Section 5.1.2. The hydrostatic and deviatoric stresses are also evaluated. The stress calculations for each bin are carried out as the indenter is penetrating the bed. Once the indenter is inside a bin, the calculation volume in Equation (5.1) is reduced to the volume of the bin which is not occupied by the indenter. The calculation of effective bin volume due to the interaction between the spherical indenter and cuboid bins is mathematically complex; hence the stress calculations are performed only for the range of depths within which the indenter does not have an intersection with the bin under consideration. The deviatoric and hydrostatic stresses within each of the bins for indenter diameters of 7, 13 and 25 mm are shown in Figures 5.9-5.11, respectively.

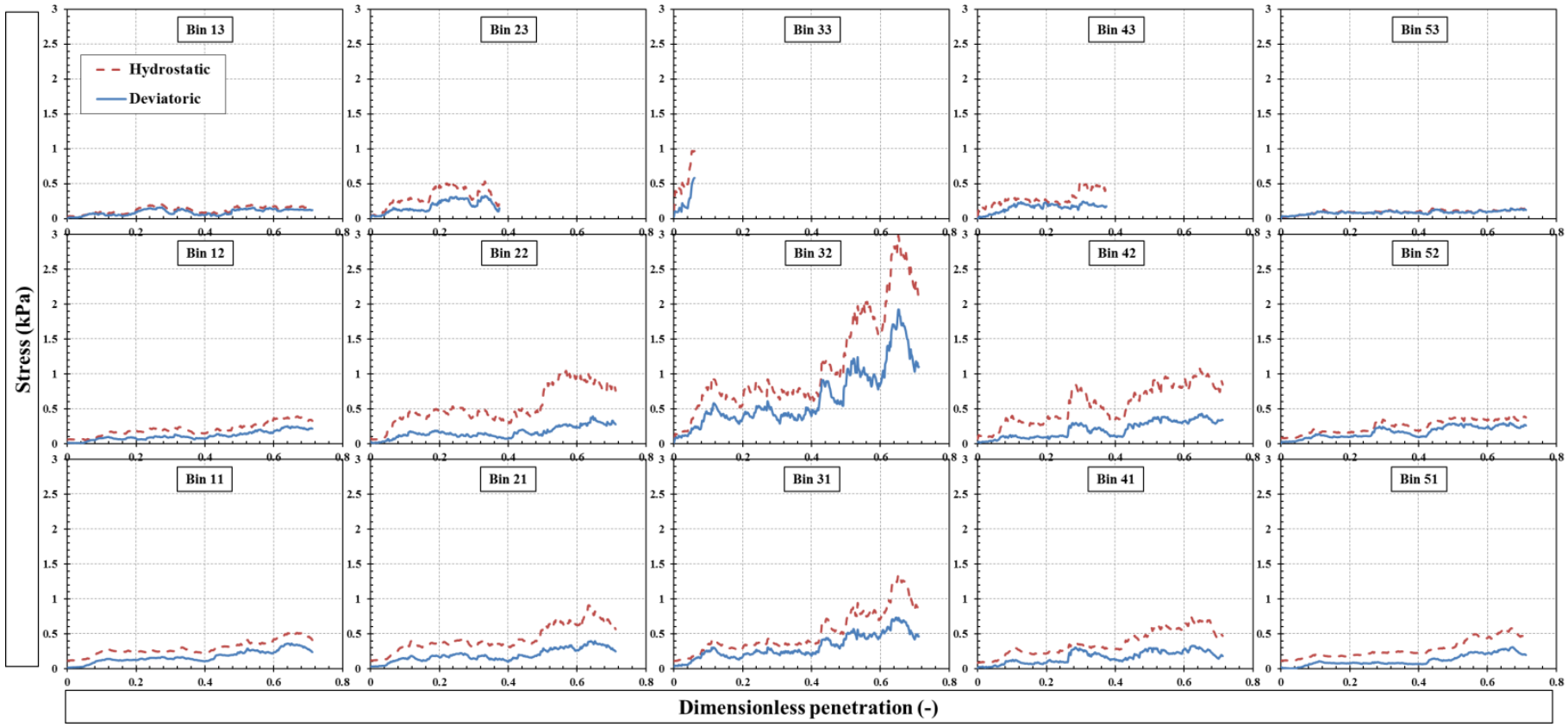

Figure 5.9: Hydrostatic and deviatoric stresses within the cuboid bins (σ_{pre} = 10 kPa, h_b = 13 mm, d_b = 39 mm, d = 7 mm)

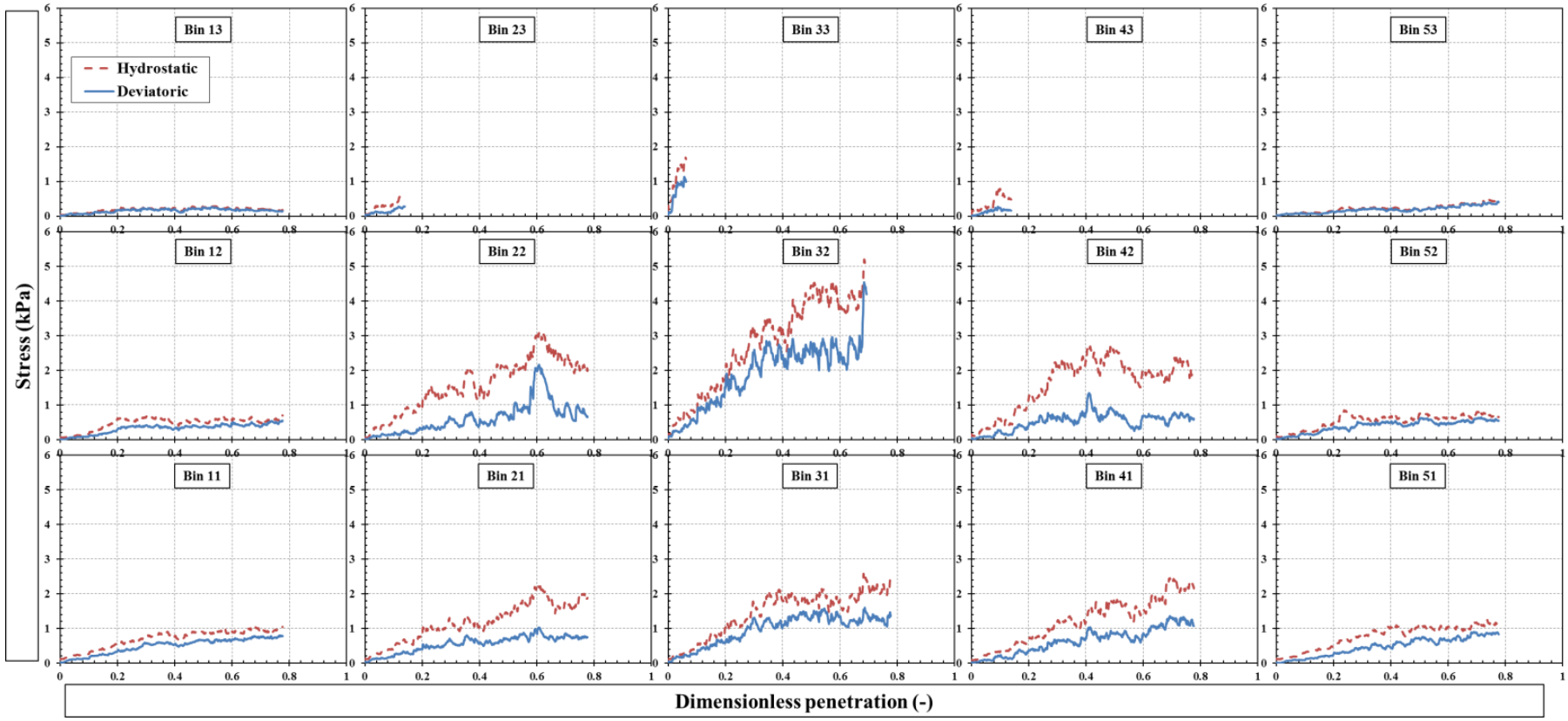

Figure 5.10: Hydrostatic and deviatoric stresses within the cuboid bins (σ_{pre} = 10 kPa, h_b = 13 mm, d_b = 39 mm, d = 13 mm)

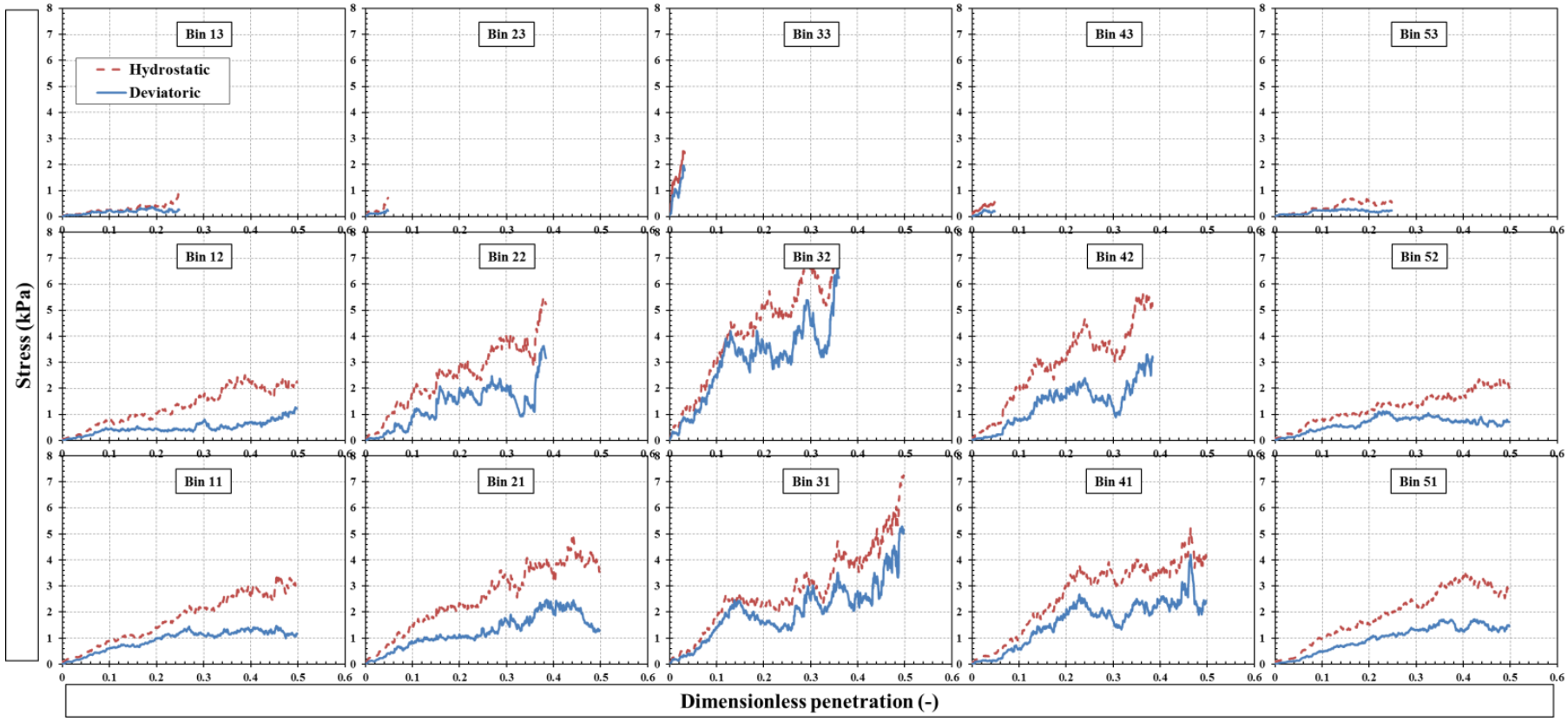

Figure 5.11: Hydrostatic and deviatoric stresses within the cuboid bins (σ_{pre} = 10 kPa, h_b = 13 mm, d_b = 39 mm, d = 25 mm)

For the 7 mm indenter, the stresses do not vary significantly within all the bins, except for the bin directly below the indenter (bin: 32) which exhibits the highest stress level. In this case, the bin width is greater than the projected diameter of impression for most of the penetration depth. This may explain the negligible increase in force in all regions except for bin 32. For both the 13 and 25 mm indenters, the stresses close to the bottom of the die (bins: 21, 31and 41) are notable, indicating interactions with the die base. The bins close to the die cylindrical wall (bins: 11, 12, 51, and 52) show high levels of stress only with the 25 mm indenter. These analyses show that with larger indenters the stresses close to the die base are relatively large and the stresses close to the die wall may also be large. This indicates that the die in this case provides a resistance to the bed shear deformation caused by the indenter. It is necessary to have a sufficiently large clearance between the edge of the indentation zone and the die wall and the base, such that the plastic flow of the powder is not restrained by the boundaries. The principle of flowability measurement using this technique relies upon establishing a constraint factor, i.e. the ratio between hardness and plastic yield stress for a given material. If the indenter diameter is too large the constraint factor will increase due to the wall effects, rather than being purely determined by the shear zone.

In order to clarify the influence of wall confinement on hardness measurements, a wider range of simulations is required. By varying the bed height and die diameter, the minimum sample quantity which is required to reliably measure hardness by ball indentation can be determined. Therefore in addition to the simulations with a bed height of 13 mm and a bed diameter of 39 mm, a series of simulations are performed for a die diameter of 45 mm and bed heights of 20, 30 and 50 mm, using a 13 mm indenter.

Hardness against dimensionless penetration for these four simulations is shown in Figure 5.12.

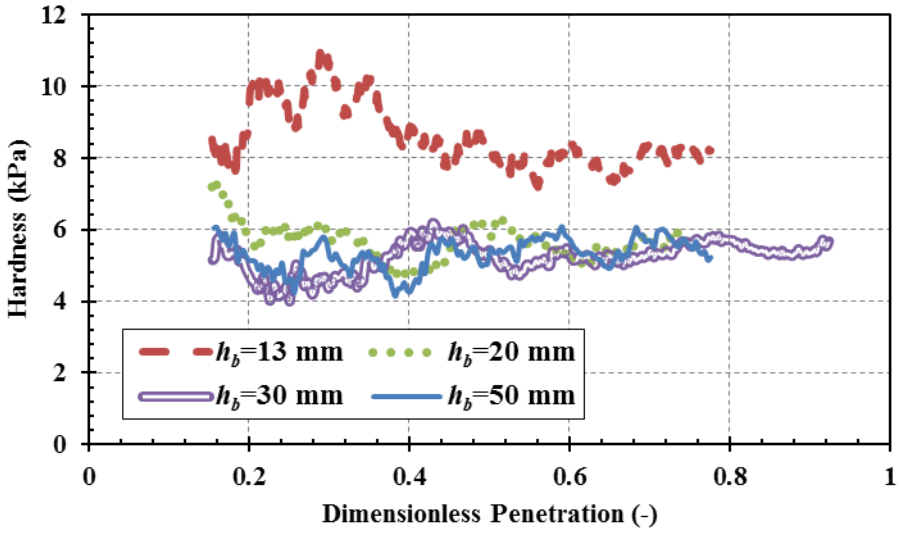

Figure 5.12: Hardness vs. dimensionless penetration for four different bed heights (σ_{pre} = 10 kPa, d = 13 mm)

For all of the bed heights, initial fluctuations in hardness can be observed; however, bed heights of 20, 30 and 50 mm exhibit lower hardness values (about 6 kPa) than the 13 mm bed height (about 8 kPa). Since for the larger bed heights a relatively constant hardness can be obtained, the simulations for this range of bed heights are not influenced by confinement at the base. This is shown to be the case by detailed analyses of the internal stresses and velocities, similar to those carried out for the 13 mm bed height. As compared to the bin analysis for the 13 mm bed height, the cuboid region here is extended by 1 row of cuboid bins towards the die base for the bed height of 20 mm (Figure 5.13) in order to analyse the stresses throughout the assembly.

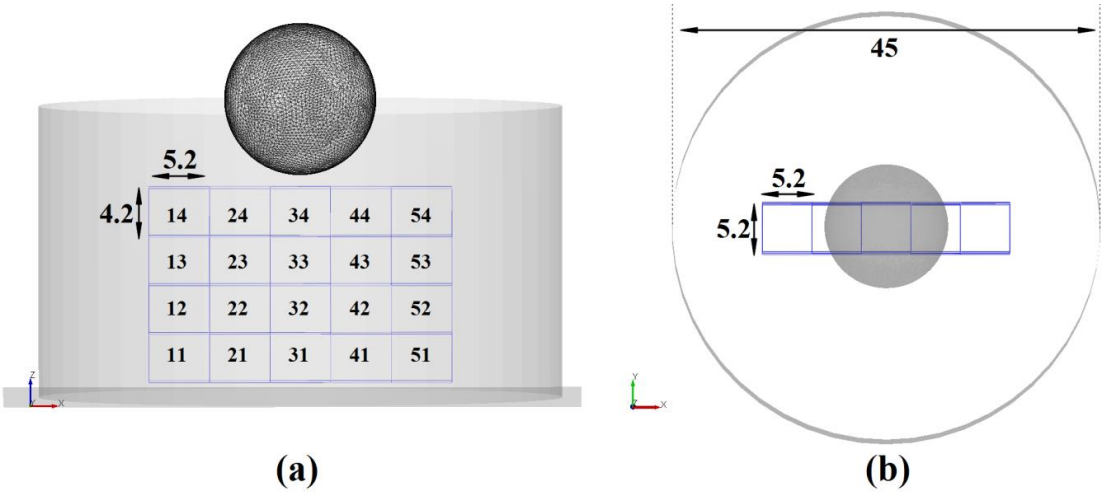

Figure 5.13: Cuboid bins used for localised velocity and stress analysis for 20 mm bed height (a) side view (b) plan view (dimensions are normalised by mean particle size which is 1 mm)

The internal stresses inside each bin are shown in Figure 5.14.

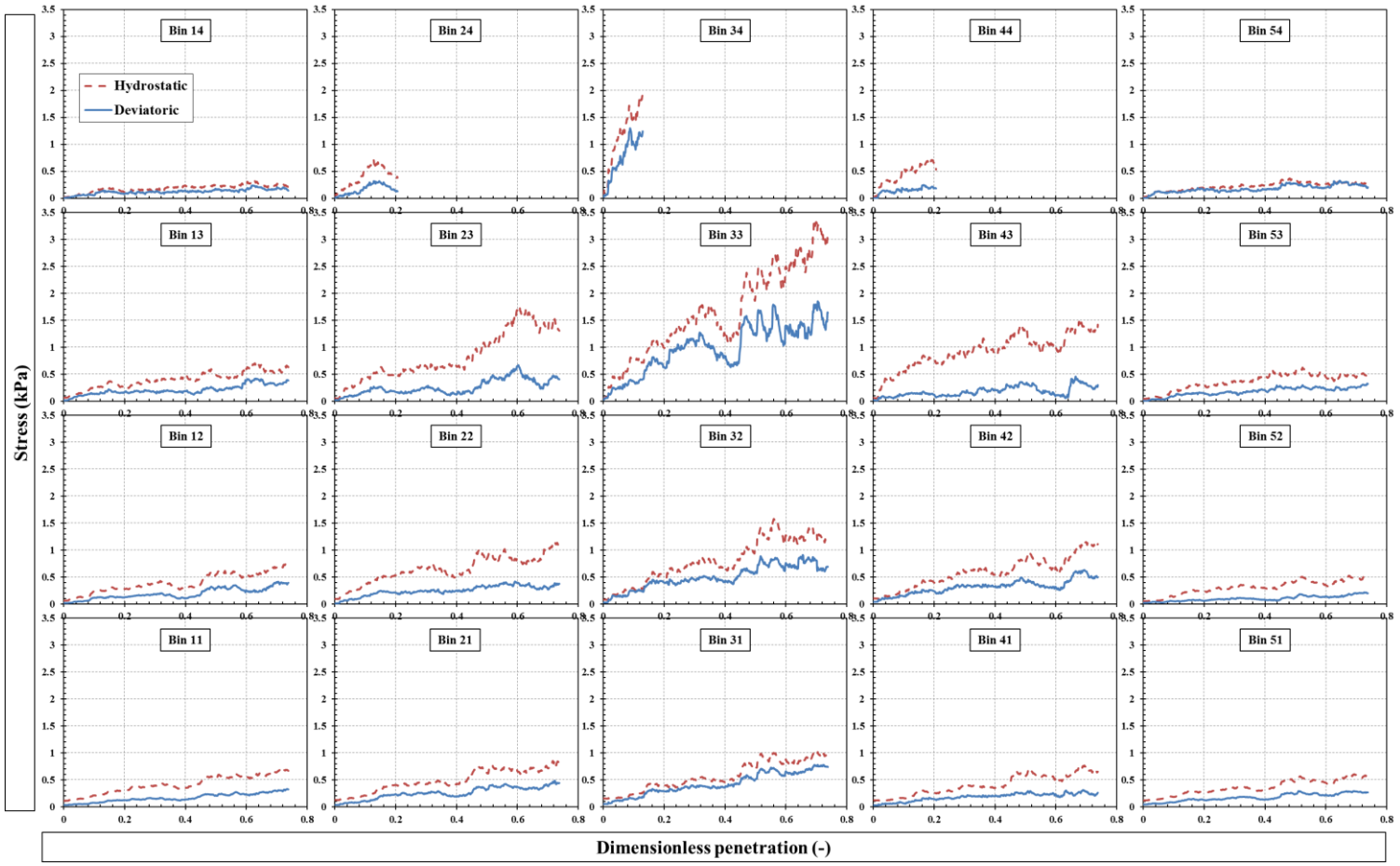

Figure 5.14: Hydrostatic and deviatoric stresses within cuboid bins (σ_{pre} = 10 kPa, h_b = 20 mm, d_b = 45 mm, d = 13 mm)

As it can be seen, the stresses decrease to negligible levels towards the base and cylindrical walls. Near the base, these stresses are negligible. This is another indication that for this scale of simulation, the wall confinement is not influencing the hardness.

With the minimum sample size in terms of bed height and bed diameter now determined, a sensitivity analysis for a range of indenter sizes is carried out to reveal the effect of indenter size on hardness measurement. The same range of indenter sizes as of the previous case is used here to simulate ball indentation on the 20 mm bed height. The bed is pre-consolidated to 10 kPa. Figure 5.15 shows hardness against dimensionless penetration for indenter sizes of 16, 19 and 22 mm.

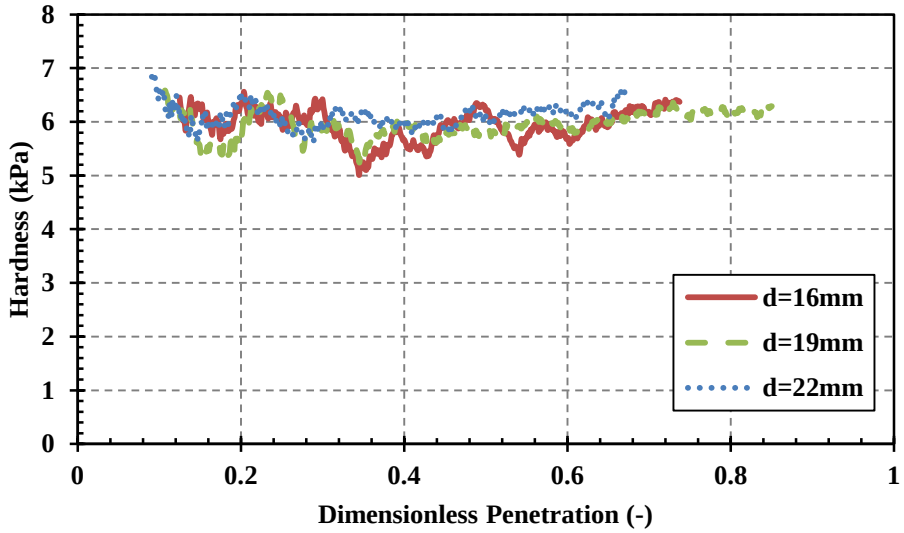

Figure 5.15: Hardness as a function of dimensionless penetration (σ_{pre} = 10 kPa, h_b = 20mm, d_b = 45 mm)

As compared to the 13 mm bed height system (Figures 5.3-5.6), the hardness shows smaller fluctuations. For this range of indenter sizes, a relatively constant value of hardness (about 6 kPa) is obtained. Figure 5.16 shows the hardness as a function of the dimensionless penetration for indenter diameters of 7, 10 and 13 mm, bed height of 20 mm and bed diameter of 45 mm.

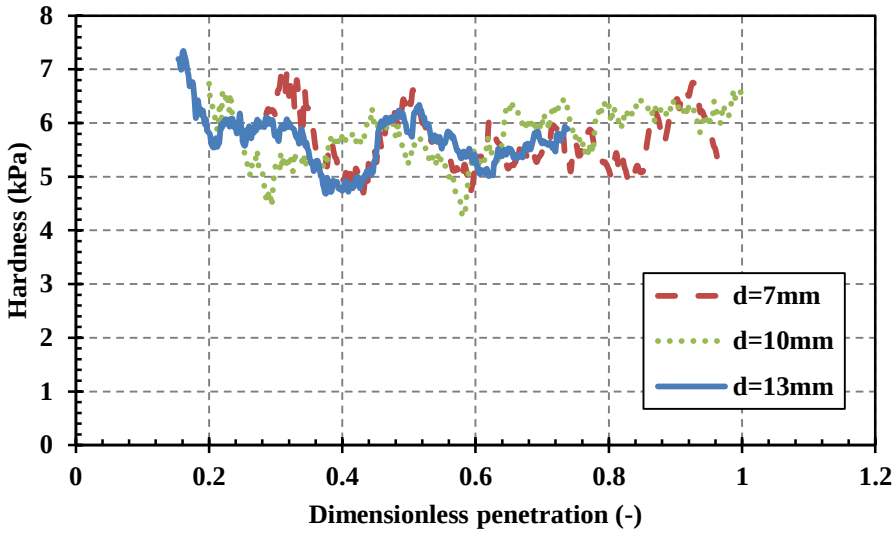

Figure 5.16: Hardness as a function of dimensionless penetration (σ_{pre} = 10 kPa, h_b = 20 mm, d_b = 45mm)

As compared to the larger indenters (16-22 mm in Figure 5.15), the fluctuations within the whole range of dimensionless penetration depths are larger for indenter diameters of 7, 10 and 13 mm. Similar to the 13 mm bed height case, this can be attributed to the fact that the smaller indenters are comparable in size to single particles, and rearrangements at the single particle level influence the force on the indenter throughout the indentation process, resulting in instabilities. The increase in fluctuations with decreasing the

indenter size can be quantitatively observed in Figure 5.17, by the range of fluctuations as it widens for smaller indenters.

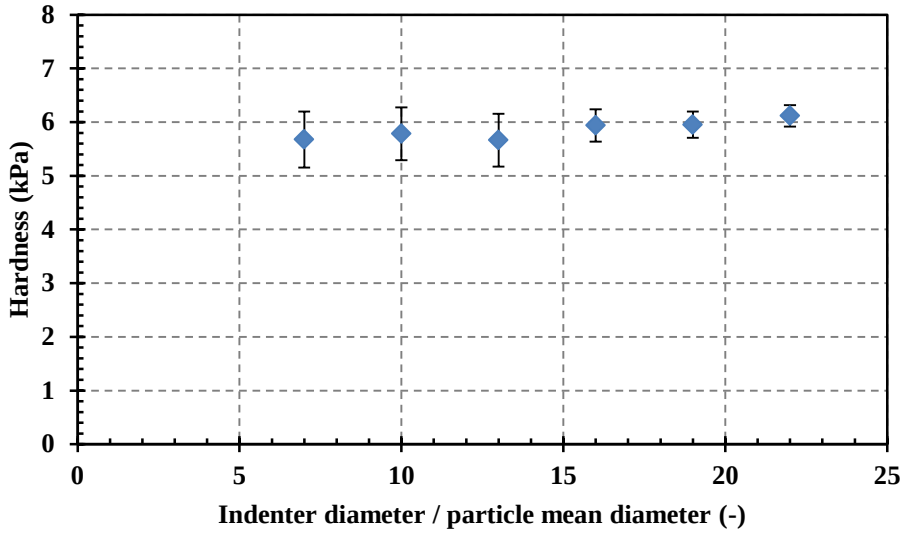

Figure 5.17: Average hardness with fluctuation bars indicating standard deviation for different indenter sizes (σ_{pre} = 10 kPa, h_b = 20 mm, d_b = 45mm)

It can be concluded that the indenter size should be greater than 13 particle diameters, with 16 diameters being adequate.

With the minimum sample size and suitable indenter size now determined, the operation window for the penetration depth is investigated by calculation of hydrostatic stress inside a dynamic bin directly below and centrally aligned with the indenter, whose position is fixed relative to the indenter, i.e. it moves with the indenter (see Figure 5.18). The size of the bin is the same as the individual bins in the previous analyses, i.e. 5.2, 5.2 and 4.2 mm in x, y and z directions, respectively.

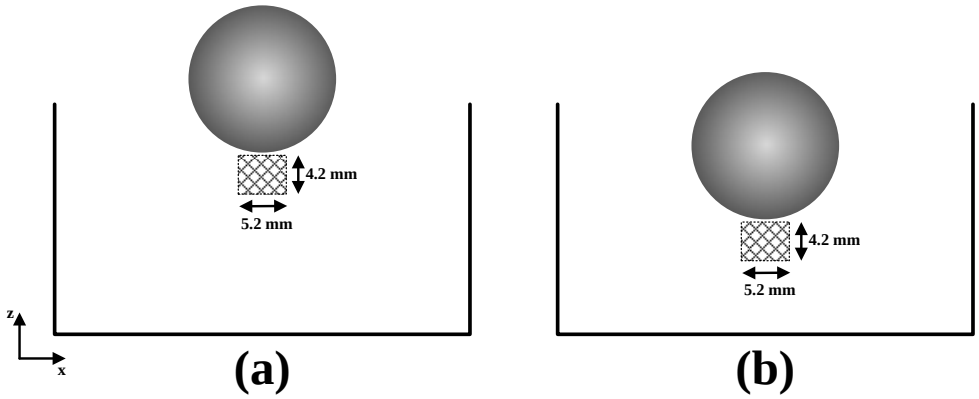

Figure 5.18: Schematic diagram of the dynamic bin underneath the indenter at two different penetration depths

Figure 5.19 shows the hydrostatic stress inside this bin for indenter diameters of 7, 16, 19 and 22 mm, a bed height of 20 mm and a bed diameter of 45 mm.

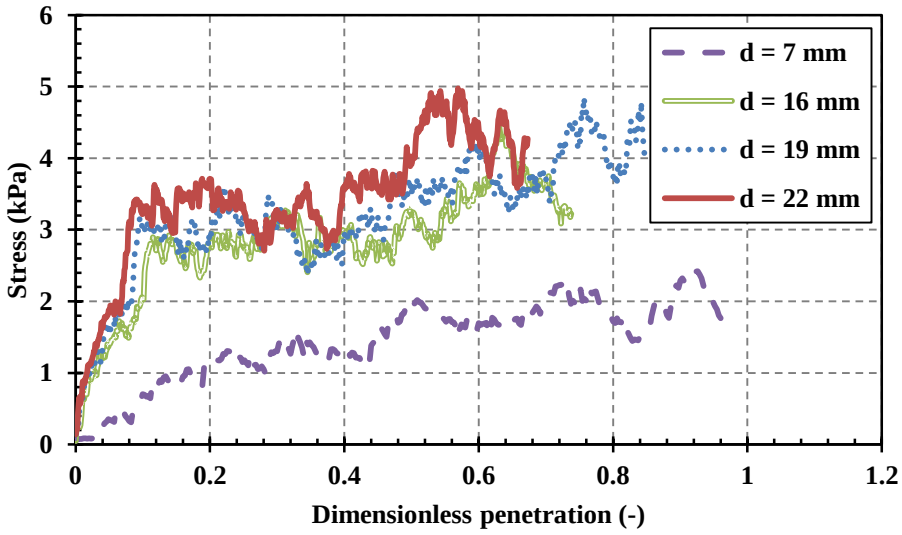

Figure 5.19: Hydrostatic stress inside the dynamic bin as a function of dimensionless penetration for different indenter sizes (σ_{pre} = 10 kPa, h_b = 20 mm, d_b = 45mm)

For the suitable indenter sizes, i.e. 16, 19 and 22 mm indenters, the hydrostatic stress increases initially up to a dimensionless penetration of about 0.1. Beyond this point the stress has a relatively constant average value, although fluctuating. This is the region of interest where the flow stress is calculated. For dimensionless penetrations beyond 0.5, the stress starts increasing again, which indicates the influence of a number of factors depending on the proximity of the walls and the base and ultimate penetration depth. For the 7-mm indenter, it is difficult to determine a range for constant value of hardness due to large fluctuations.

5.3 **Conclusions**

The ball indentation on a compacted assembly of cohesive spheres was simulated using DEM. The hardness of the compacted assembly was evaluated for a range of sample quantities. It was found that a minimum bed height of 20 particle diameters is required in order to achieve reliable hardness values. With small sample sizes, for which the surrounding walls and base of the die restrain the bed deformation, an increase in the resistance of the bed, i.e. an increase in hardness, is observed. It is necessary to have a sufficiently large clearance between the edge of the indentation zone and the die wall, such that the plastic flow of the powder is not restrained. The penetration depth is normalised with respect to the indenter radius in order to allow the effect of different indenter sizes to be analysed and compared. The penetration depth should be sufficiently large to cause notable bed shear deformation. It is found that this minimum penetration depth is approximately equal to 0.1 in terms of dimensionless penetration. A sensitivity analysis of indenter size reveals that indenters with diameters smaller than 16 particle diameters exhibit fluctuations in hardness measurements, whereas indenters

with a diameter of up to 22 particle diameters result in stable hardness values, providing the minimum sample criteria are met. As the indenter size decreases, it approaches the size of bed particles. Therefore, rearrangements at the single particle level influence the force on the indenter throughout the indentation process, resulting in fluctuations in hardness. With very large indenters comparable in size to the die, the measurement of hardness may be affected by the wall.

CHAPTER 6 Sensitivity Analysis of Indenter and Single Particle Properties in Ball Indentation Method by DEM

With the minimum sample size, suitable indenter size and penetration depth determined numerically in Chapter 5, the operation window for the indenter properties such as shape, stiffness and friction is investigated in this chapter. Moreover variation of hardness and internal stresses with single particle properties such as inter-particle friction and cohesion are analysed by DEM simulations of the ball indentation process.

6.1 DEM simulation of the indentation process

For DEM simulations reported in this chapter, the simplified version of the proposed contact model discussed in Chapter 4 is used (see Figure 4.20). The simulations are based on meeting the criteria defined in Chapter 5. The sample height and diameter are 20 and 45 mean particle diameters, respectively. The indentation process was simulated using a 16 mm indenter. The simulations are conducted using EDEM® software provided by DEM Solutions, Edinburgh, UK.

Particles with a normal size distribution and a mean diameter of 1 mm (as shown in Table 6.1) are generated inside the cylindrical die. The use of a size distribution rather

than a mono disperse system avoids the formation of ordered packing. In order to provide a bed height of approximately 20 mm, 29000 particles are generated.

Table 6.1: Size distribution of the generated particles

Particle diameter (mm)	Number Frequency (%)
0.724	3.87
0.814	11.31
0.896	21.14
1.000	27.92
1.104	20.99
1.188	11.02
1.278	3.76
1.28	3.74
1.41	0.29

The tangential stiffness, k_t, was equated to the elastic stiffness, k_e, throughout the simulations. The material and interactional properties of the elasto-plastic-adhesive particles and the non-cohesive elastic geometries (indenter, cylindrical die and piston) are summarised in Tables 6.2 and 6.3.

Table 6.2: Material properties used in the simulations

Material property	Particles	Geometries
Density (kg/m^3)	2500	7800
Poisson's ratio (-)	0.25	0.3
Elastic stiffness, k_e (MN/m)	1	8
Plastic stiffness, k_p (MN/m)	0.1	-
Plastic-adhesive stiffness, k_{cp} (MN/m)	0.01	-
Tangential stiffness, k_t (MN/m)	1	8

Table 6.3: Interaction properties used in the simulations

Interactional property	Particle - Particle	Particle - Wall
Coefficient of restitution (-)	0.50	0.30
Coefficient of sliding friction (-)	0.15	0.0
Coefficient of rolling friction (-)	0.01	0.0
Interface energy (J/m^2)	2.00	0.0

The particles are generated within the die, ascribed the properties as given in Tables 6.1-6.3 and allowed to settle under gravity. The assembly is then consolidated with a piston at a constant strain rate of 1 s^{-1} to 10 kPa. Once the desired stress is achieved, the piston is unloaded with the same speed as that of the loading, similar to the simulations of Chapter 5.

As in the analysis of Chapter 5, a dynamic bin with dimensions of 5.2, 5.2 and 4.2 mm in x, y and z-directions, respectively was considered. The hydrostatic and deviatoric

stresses inside this dynamic bin are evaluated and the results are compared to the hardness value measured by the indenter (see Section 5.1.2).

6.2 Sensitivity analysis of indenter properties

6.2.1 Indenter stiffness

The simulations were carried out for a wide range of indenter stiffness. The result of hardness, hydrostatic and deviatoric stresses as functions of indenter stiffness is shown in Figure 6.1.

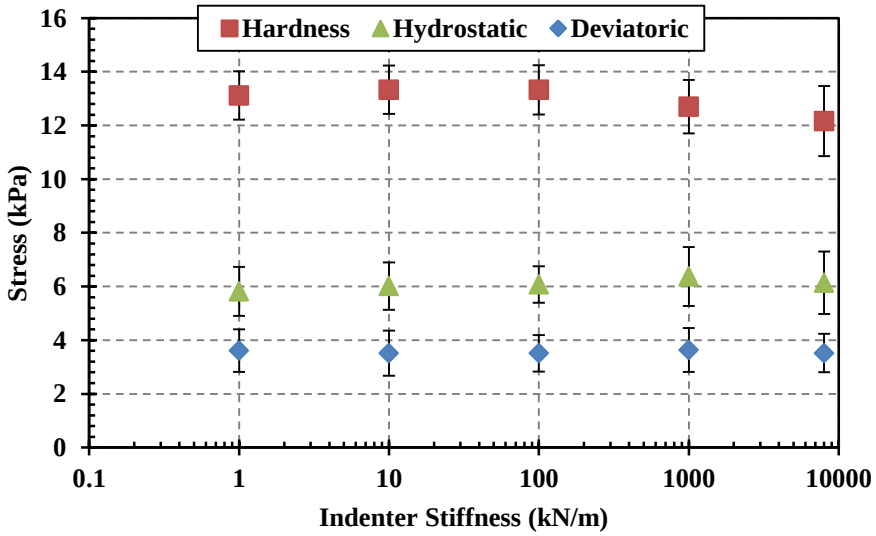

Figure 6.1: Hardness, hydrostatic and deviatoric stresses as functions of indenter stiffness

As it can be seen, there is hardly any effect of indenter stiffness in hardness, or hydrostatic and deviatoric stress measurement in the ball indentation method.

6.2.2 **Indenter shape**

The simulations were carried out with three different indenter shapes: cubic, cylindrical and spherical indenters. The spherical and cylindrical indenters had a diameter of 16 mm, while the cubic indenter had equal sides of 16 mm. Figure 6.2 shows hardness, hydrostatic and deviatoric stresses measured by the three different indenter shapes.

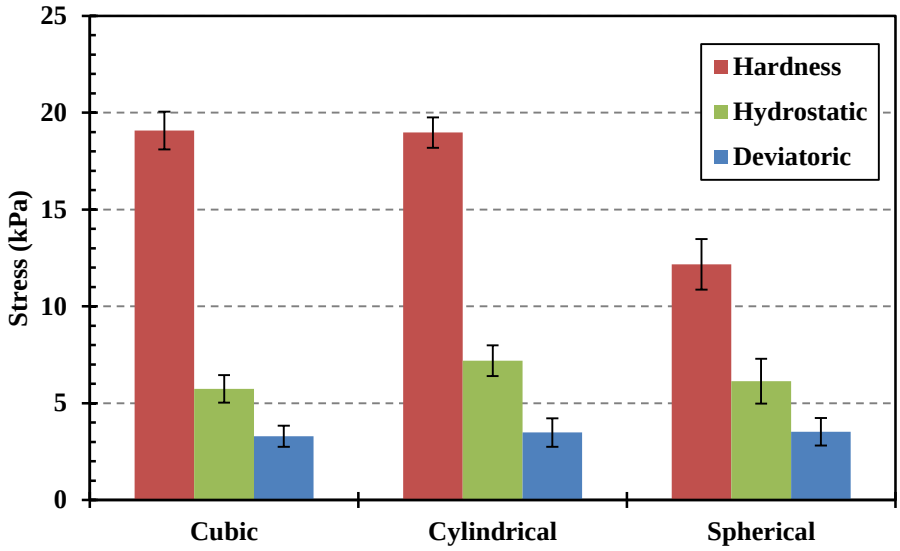

Figure 6.2: Hardness, hydrostatic and deviatoric stresses measured by the three different indenter shapes

The hardness measured by cubic and cylindrical indenters is higher to that measured by a spherical indenter. The internal stresses within the dynamic bin do not change significantly with indenter shape. In order to illustrate this behaviour qualitatively, Figure 6.3 shows the assembly at the same penetration depth using the three indenter shapes. The colour-scale of each particle in Figure 6.3 indicates its velocity, with blue particles having negligible velocity and red particles with large velocity. The colour

range for all the three cases is the same; minimum (blue) is 0.002 m/s and maximum (red) is 0.04 m/s.

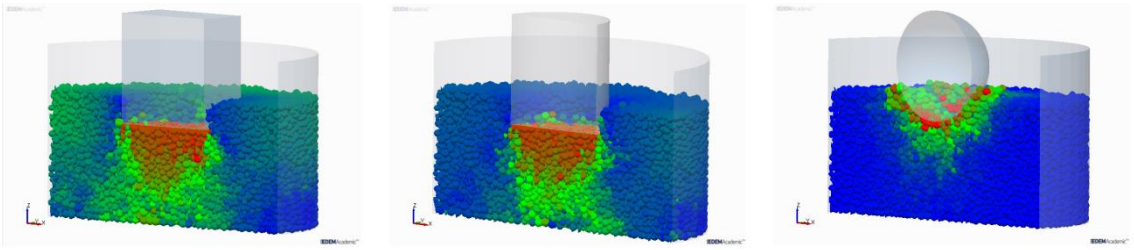

Figure 6.3: DEM simulation of indentation technique using (a) cubic, (b) cylindrical and (c) spherical indenters at penetration depth of 3.8 mm. For visualisation purposes, the assembly is clipped by a plane y-direction. The particles are coloured based on their magnitude of velocity (red, green and blue indicate high to low velocities)

As it can be seen, the particles close to the bottom base and surrounding wall show some velocity (i.e. particle movement) for cubic and cylindrical indenters, in contrast to the spherical case. This suggests that cylindrical and cubical indenters must be smaller for this bed height, or the bed height must be larger.

Close inspection of data on which Figure 6.3 is based indicated that there is an increase in solids fraction with cubic and cylindrical indenters relative to the spherical case. In order to investigate this behaviour quantitatively, the solids fraction in a bin with dimensions of 0.01, 0.01 and 0.012 in x, y and z-directions, respectively, which is located in the centre of the cylindrical die (see Figure 6.4) is evaluated as a function of penetration depth for the three indenter shapes.

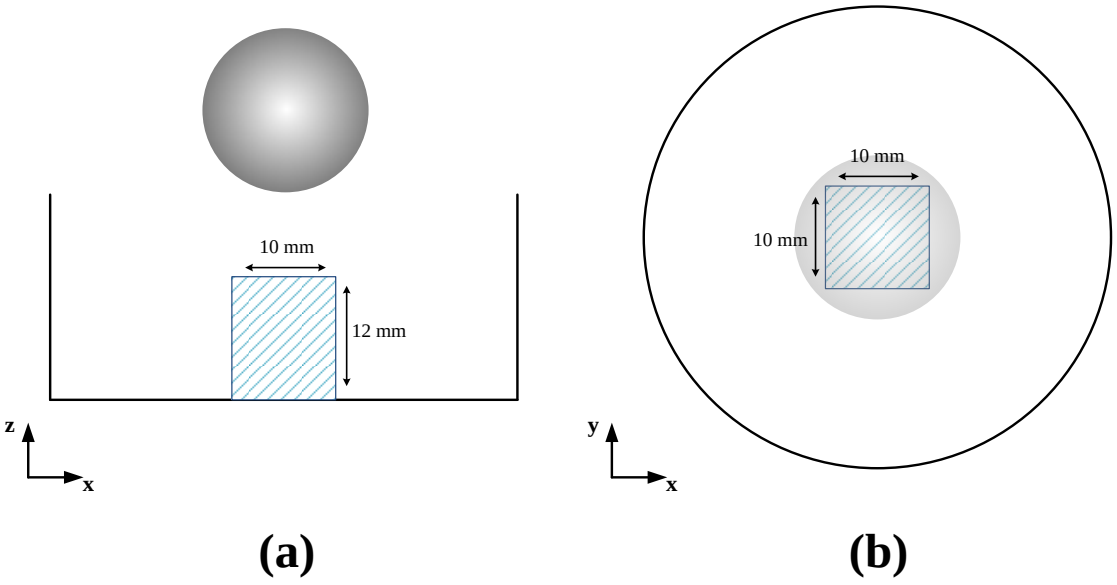

Figure 6.4: The cuboid bin used for solids fraction analysis: (a) side view (b) plan view

Figure 6.5 shows the solids fraction inside the cuboid bin as a function of penetration depth for the three indenter shapes.

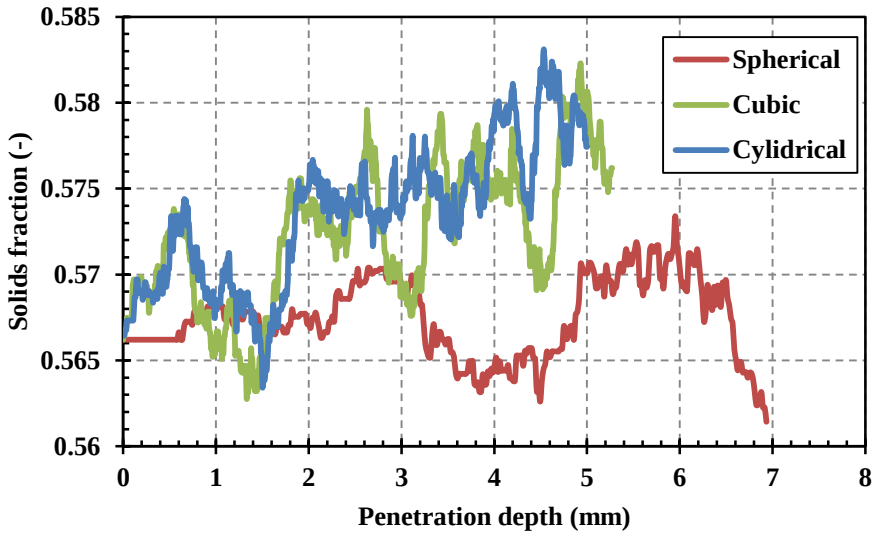

Figure 6.5: Solids fraction inside the cuboid bin as a function of penetration depth for three different indenter shapes

As it can be seen, the solids fraction is increased for cubic and cylindrical indenters relative to the spherical indenter, an indication of localised consolidation with cylindrical and cubic indenters. In fact, the curvature of a sphere results in a smoother transition from elastic to plastic behaviour and allows the powder to be sheared rather than being consolidated.

6.2.3 **Indenter friction**

The simulations were also conducted for a range of indenter coefficient of sliding friction between the particles and the spherical indenter (i.e. indenter friction). The results of hardness, hydrostatic and deviatoric stresses are shown in Figure 6.6.

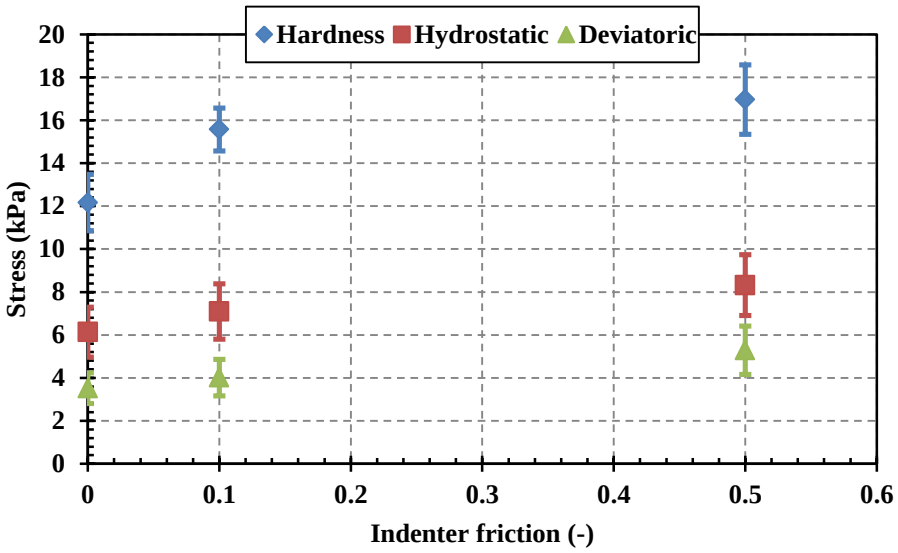

Figure 6.6: Hardness, hydrostatic and deviatoric stresses as functions of indenter friction

A general increasing trend in the stresses with indenter friction can be observed. This increase is notable when the coefficient of sliding friction is increased from zero to 0.1. Increasing the sliding friction of the indenter provides additional resistance to shearing

of the particles contacting the indenter, consequently the hardness, which is evaluated by the force acting on the indenter is increased.

6.3 Effects of single particle properties

6.3.1 Inter-particle friction

Figure 6.7 shows hardness, hydrostatic and deviatoric stresses as functions of inter-particle coefficient of sliding friction.

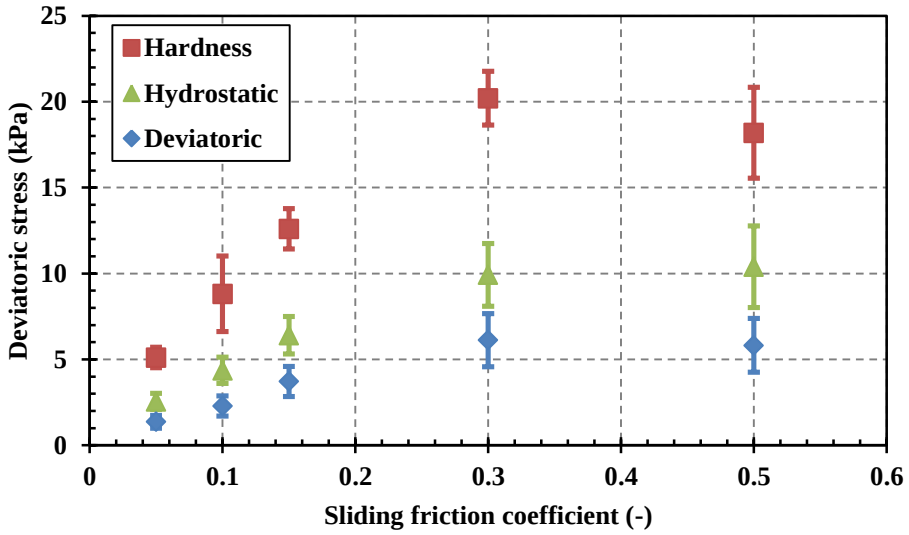

Figure 6.7: Hardness, hydrostatic and deviatoric stresses as functions of inter-particle coefficient of sliding friction

Increasing the inter-particle friction would increase the internal resistance to shear deformation, an observation which was expected. It can be observed that there is a limit for the sliding friction coefficient beyond which the stresses do not change (compare μ_s = 0.3 and 0.5 in Figure 6.7). This can be attributed to the fact that, within the

indentation process, the tangential force at the single particle does not become large enough to meet the Coulomb's criterion of sliding. In other words, for highly frictional contacts, contact sliding does not occur. The sliding is indeed a dominant factor in shear deformation of the assembly. It can be concluded from Figure 6.7 that when inter-particle coefficient of sliding friction is larger than 0.3, the contact sliding behaviour becomes similar.

6.3.2 **Inter-particle cohesion**

Figure 6.8 shows hardness, hydrostatic and deviatoric stresses as functions of inter-particle interface energy.

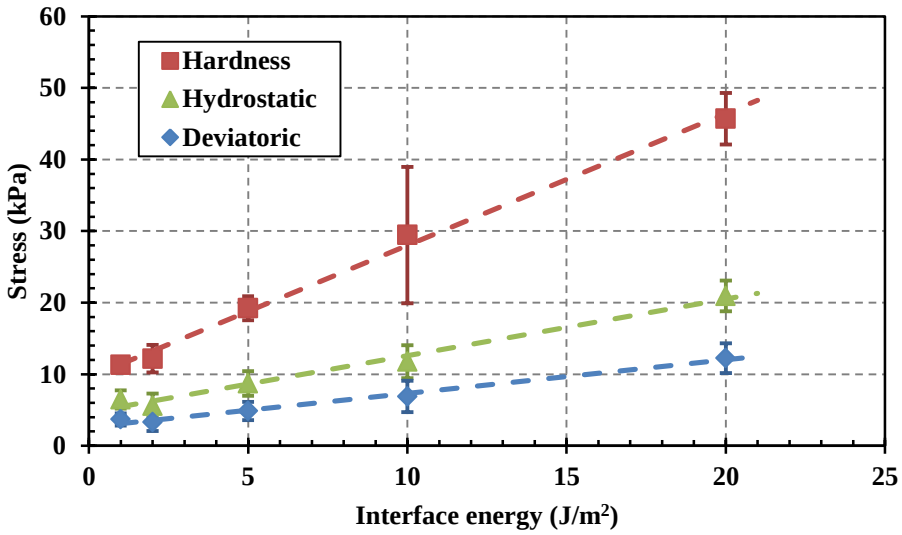

Figure 6.8: Hardness, hydrostatic and deviatoric stresses as functions of inter-particle interface energy

As it was expected, increasing the cohesion increases hardness and internal stresses, since the resistance to flow is increased

6.4 **Conclusions**

The ball indentation on a compacted assembly of cohesive spheres was simulated using DEM. The hardness and localised hydrostatic and deviatoric stresses were evaluated for various indenter and inter-particle properties. The hardness measurements were found to be independent of indenter stiffness. Indenter friction slightly increased the hardness, although its influence on the internal stresses was negligible. Cubic and cylindrical indenters measured significantly larger hardness value compared to the spherical indenter. It was shown that with cubic and cylindrical indenters, the powder bed is locally consolidated, hence the measured value of hardness is not representative of the bulk consolidation state. Increasing the inter-particle friction and cohesion resulted in higher hardness and internal stresses due the increase in resistance to shear deformation.

CHAPTER 7 Numerical Analysis of Strain Rate Sensitivity in Ball Indentation Method by DEM

In industrial processes such as mixing, blending, handling and storage reliable powder flow is important for product quality and a consistent production rate. Understanding the flow characteristics of the powder can avoid wastage, machinery maintenance problems and downtime in such processes. Strain rate is particularly of great interest since in the shear deformation of powder beds beyond the quasi-static regime the shear stress is dependent on the strain rate [82]. Extensive work has been reported on the rapid chute flow of large granules [84] but the intermediate regime has not been widely addressed. However, the industrial powder processes require the specification of an operational window in terms of strain rate for reliable and controllable operations. Tardos *et al.* [82] classified powder flow into three regimes based on the shear strain rate of the process. At low shear strain rates, the quasi-static regime can be identified, during which frictional forces between particles are predominant and the shear stress is independent of the strain rate. In the other extreme at very high shear strain rates, i.e. the dynamic regime, the flow is characterised by collisions between particles rather than the friction between them and hence the particle inertia is influential. There has been extensive work for this regime, in which it has been shown that the shear stress varies with the square of strain rate [85-87]. Between the quasi-static and inertial regimes lies the intermediate regime, where both collisional and frictional interactions between the

particles determine the flow characteristics [82]. Many of the flowability measurement techniques (see Section 2.4) evaluate the incipient flow at very low strain rates (i.e. the quasi-static regime), and hence cannot depict the strain rate sensitivity of powder flow. The only method by which the intermediate regime has been analysed is the Coutte device of Tardos *et al.* [82], where the powder is sheared between two concentric cylinders (with the axis being vertical). The inner cylinder is rotated at different rotational velocity forming a shear band in the gap. It was confirmed that during the quasi-static regime the stresses were independent of the strain rate. For the intermediate regime the dependency of the shear stress on the dimensionless strain rate γ^* (as given by Equation (7.1)) is with a power index less than 2.

$$\gamma^* = \gamma\left(\frac{d_p}{g}\right)^{1/2} \tag{7.1}$$

where γ is the shear strain rate, d_p is the mean particle diameter and g is the gravitational acceleration. For the dynamic regime, this dependency is to a power of 2 [88]. By increasing the strain rate, an increase in the fluctuations of the stresses was observed. It was shown that the width of the intermediate regime in terms of dimensionless shear rate is a function of assembly concentration [82]. At low particle concentration (high bed porosity), the width was relatively narrow, between dimensionless shear rates of 0.5 to 2 [82].

In two commercial developments, proprietary instruments also subject the powder to shear strains in the intermediate regime by a paddle penetrating whilst rotating in a powder bed (Freeman Powder Tester FT4 [89] and StableMicro Systems PowderFlow Analyser). However the complex paddle geometry provides a highly non-uniform strain

field, where the powder strain and strain rate increase from the centre to the cylindrical wall. Recently Hare *et al.* [54] have analysed the shear stress and strain field around a rotating impeller and have quantified their radial and axial variations. Their work shows that the shear stress is greatest in the vicinity of the front of the blades; the stresses reduce above the impeller and away from the impeller in the angular direction, providing a highly non-uniform strain field. Based on their work, the interpretation of paddle torque to elucidate the strain rate dependency of shear stresses using these commercial devices is difficult until systematic work on model materials with 'tuneable' and controlled bulk cohesion has been fully analysed.

Moreno-Atanasio *et al.* [90] simulated uniaxial unconfined compression of cohesive beds using the Distinct Element Method (DEM) for a range of strain rates. They also found that the unconfined yield stress (UYS) did not depend on strain rate for small values of strain rate (less than 2 s^{-1}), and only exhibited dependency for larger values, where a linear relationship between UYS and strain rate was reported. A power law fit with a power index of 1.2 showed the best fit for the simulations data. The threshold strain rate which defined the limiting quasi-static rate was found to be slightly dependent on the inter-particle cohesion, where by increasing the cohesion the threshold was increased slightly. It was also shown that by increasing the pre-consolidation stress, the sensitivity of UYS to the strain rate decreased in the intermediate and dynamic regimes, which was in-line with Tardos *et al.* [82] findings on assembly concentration. It should be noted that possible effects of aeration were not considered in the above analysis.

In the present chapter the strain rate sensitivity of the stresses in an assembly of cohesive spherical particles within the ball indentation process is investigated using DEM. Again, the effect of air drag in this analysis is ignored.

7.1 DEM simulations of the indentation process

The simulations properties are the same as the ones reported in Chapter 6 (see Section 6.1). The simplified version of the proposed contact model discussed in Chapter 4 is used (see Figure 4.20). The simulations are based on meeting the criteria defined in Chapter 5. The sample height and diameter are 20 and 45 mean particle diameters, respectively. The indentation process was simulated using a 16 mm indenter. The simulations are conducted using EDEM® software provided by DEM Solutions, Edinburgh, UK. Particle and geometry properties are summarised in Tables 6.1-6.3. The particles are generated within the die and allowed to settle under gravity. The assembly is then consolidated with a piston at a constant strain rate of 1 s^{-1} to 10 kPa. Once the desired stress is achieved, the piston is unloaded with the same speed as that of the loading, in a similar manner to the simulations of Chapters 5 and 6.

As in the analysis of Chapters 5 and 6, a dynamic bin with dimensions of 5.2, 5.2 and 4.2 mm in x, y and z-directions, respectively was considered. The hydrostatic and deviatoric stresses inside this dynamic bin are evaluated and the results are compared to the hardness value measured by the indenter (see Section 5.1.2).

7.2 Sensitivity of hardness, hydrostatic and deviatoric stresses to strain rate

Figures 7.1(a)-(d) show hardness, hydrostatic and deviatoric stresses inside the dynamic bin as functions of dimensionless penetration for dimensionless strain rates of 0.0115, 0.2297, 0.4594 and 2.2969, respectively.

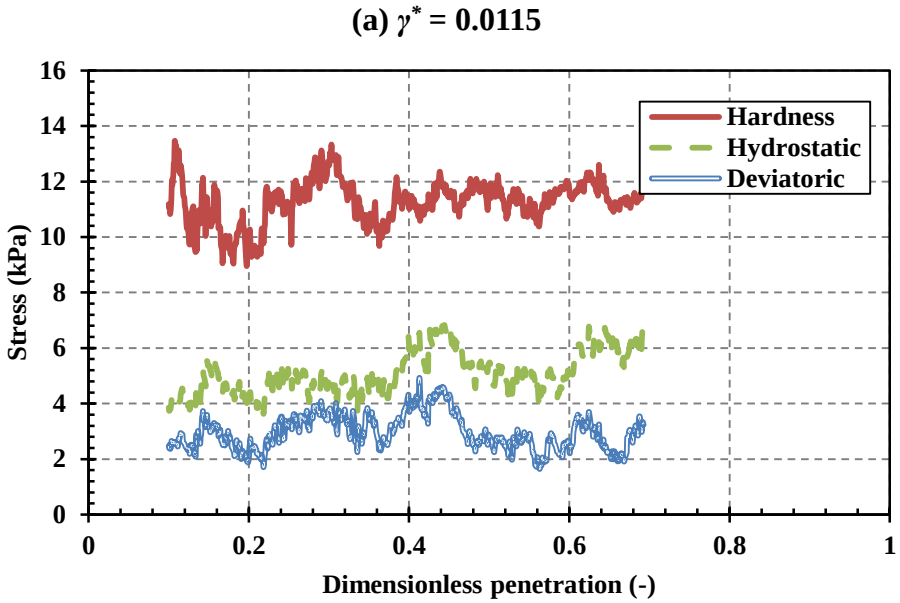

(b) γ* = 0.2297

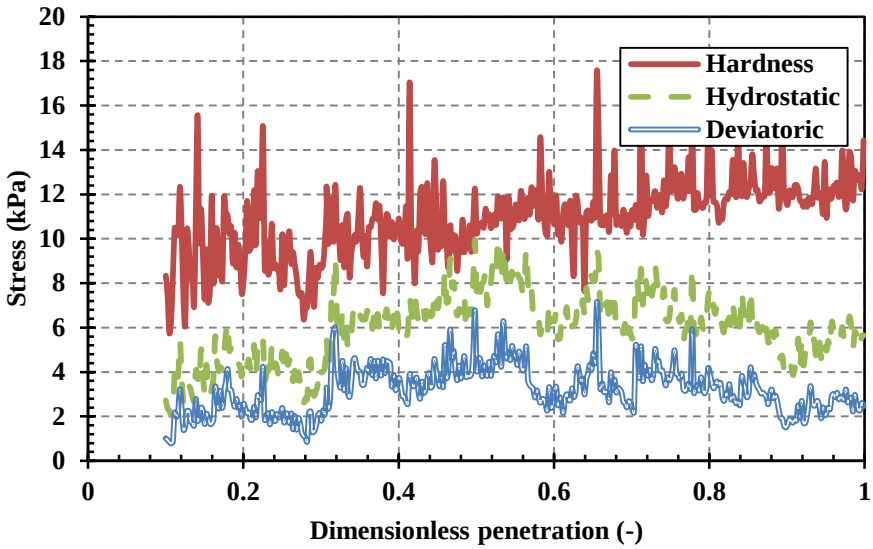

(c) γ* = 0.4594

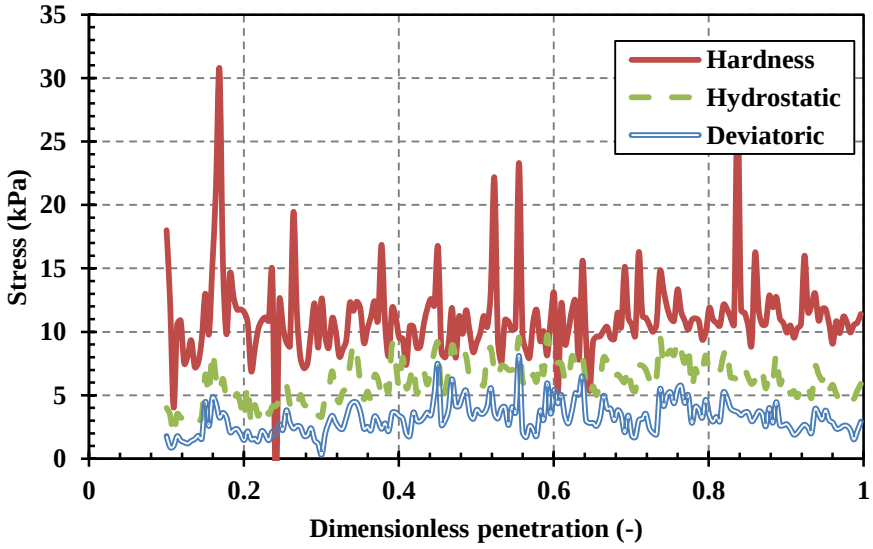

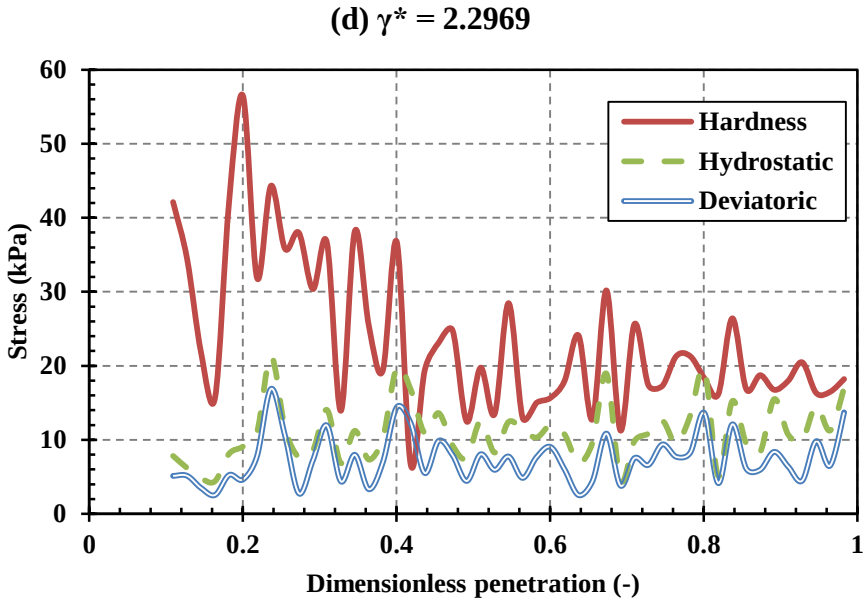

Figure 7.1: Hardness, hydrostatic and deviatoric stresses inside the dynamic bin as functions of dimensionless penetration for a number of dimensionless strain rates in the range 0.0115-2.2969

As it can be seen from Figures 7.1(a)-(d), by increasing the strain rate the fluctuations become more significant. This is in line with the finding of Tardos *et al.* [82], who showed that by increasing the strain rate large fluctuations appeared and a "liquid-like" viscous character was manifested by the bulk powder. With higher strain rates, a larger average value of hardness is evaluated, although the fluctuations are influential in determining this average. In order to facilitate further observations, the hardness, hydrostatic and deviatoric stresses inside the dynamic bin under the indenter are shown in Figures 7.2(a)-(c), respectively, as a function of dimensionless penetration for the four dimensionless strain rates.

(a) Hardness

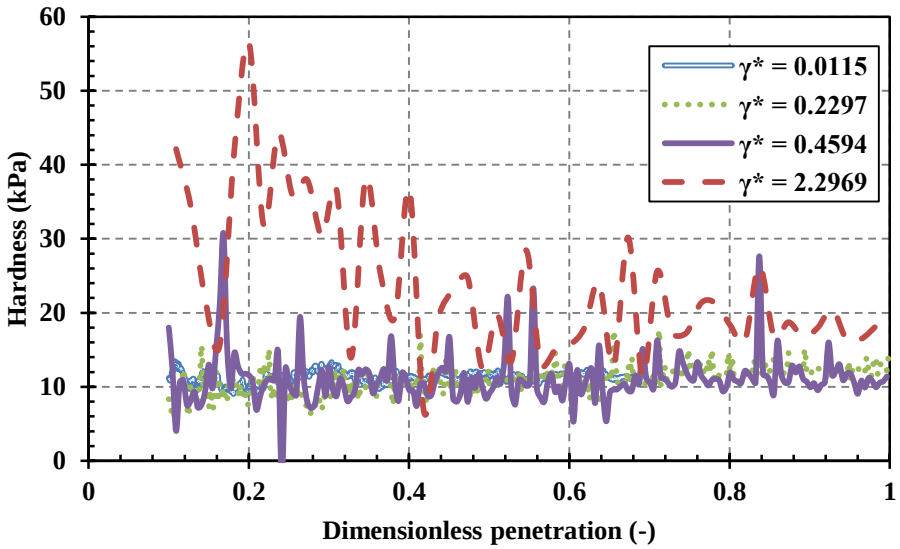

(b) Hydrostatic stress

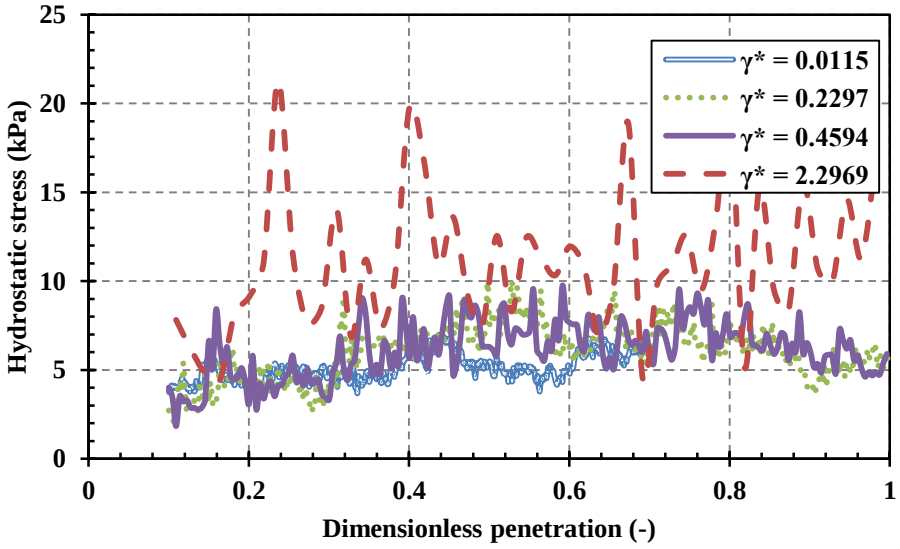

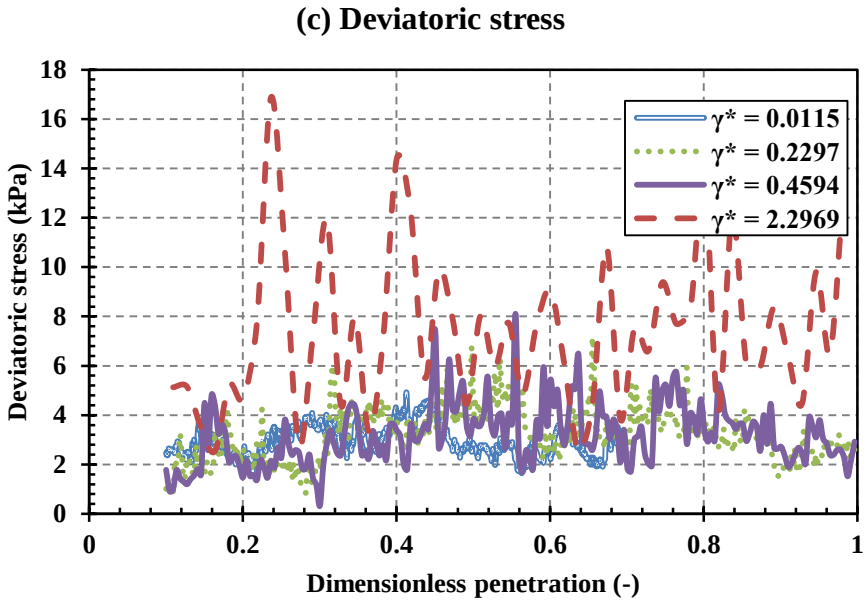

Figure 7.2: Hardness, hydrostatic and deviatoric stresses inside the dynamic bin as functions of dimensionless penetration for four of dimensionless strain rates in the range 0.0115-2.2969

As it can be seen from Figures 7.2(a)-(c), by increasing the strain rate above a threshold limit, the stresses in the system increase substantially. In order to define this threshold in terms of dimensionless strain rate, a wide range of indentation speeds were tested. The hardness, hydrostatic and deviatoric stresses inside the dynamic bin are plotted in Figure 7.3, as functions of γ^*, with the error bars indicating the standard deviation of the fluctuations.

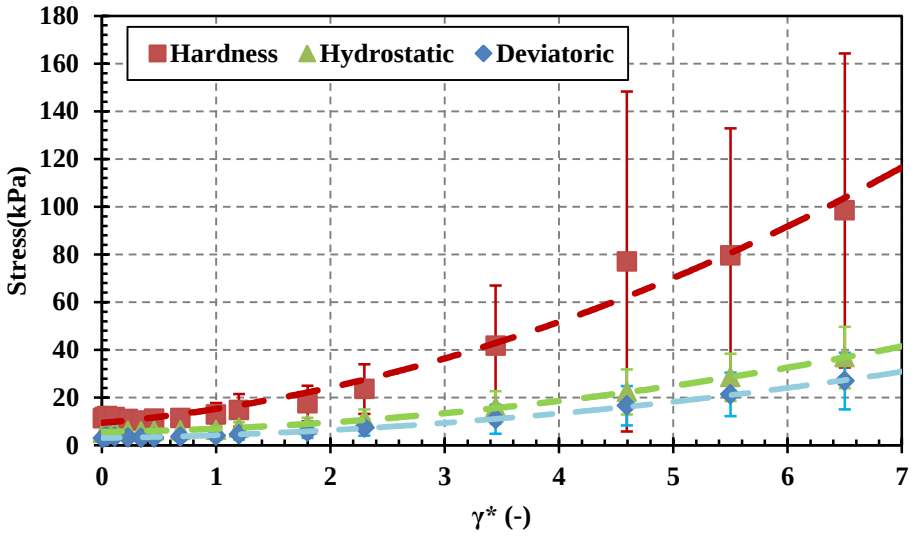

Figure 7.3: Hardness, hydrostatic and deviatoric stresses inside the dynamic bin as functions of dimensionless strain rate with the error bars indicating the standard deviation of the fluctuations

As it can be seen from Figure 7.3, the stresses show independency to the strain rate for small indenter speeds up to a dimensionless strain rate of about 1, beyond which the stresses start increasing with increasing strain rate. The error bars also decrease in width with the lowering of the strain rate, in line with Tardos *et al.*'s [82] work, where it was found that the dynamic and quasi-static regimes reach asymptotically to the limits of large and small fluctuations, respectively.

Figure 7.4 shows hardness, hydrostatic and deviatoric stresses inside the dynamic bin as functions of γ^* for values of $\gamma^* < 1$, with the error bars indicating the standard deviation of the fluctuations.

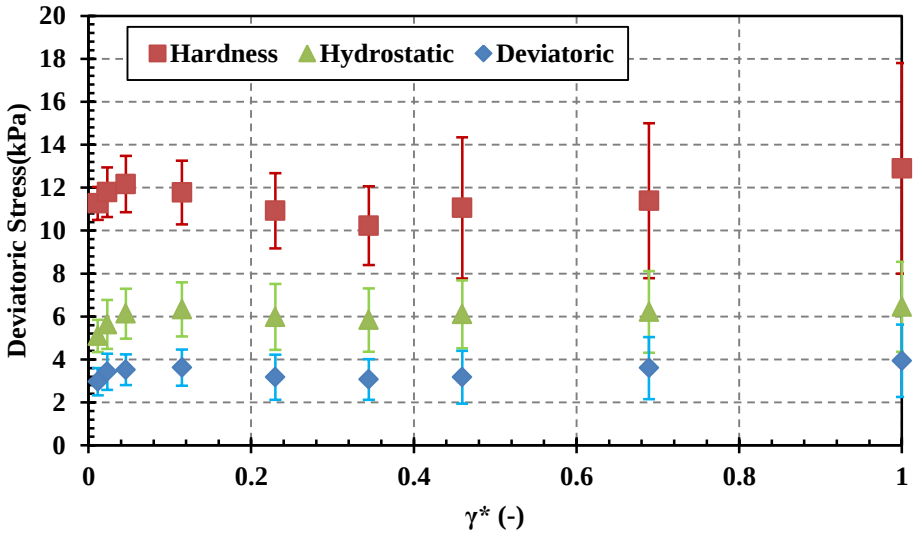

Figure 7.4: Hardness, hydrostatic and deviatoric stresses inside the dynamic bin as functions of dimensionless penetration

As it can be seen, the stresses are relatively independent of the strain rate for this range, though the fluctuations increase with γ^*. It is noteworthy that the ratio between the internal stresses and hardness is constant when $\gamma^* < 1$ (see Figure 7.4), but changes with the strain rate above this threshold (see Figure 7.3), implying that the flow stress, as expressed by the indentation hardness, becomes strain rate dependent at high strain rates.

7.3 Effects of integration time-step

The strain rate dependency is a matter of particle inertia, giving rise to different force transmission fabric, and should hence be independent of the integration time-step. In order to check this, the integration time-step was varied and the stress profile analysed. The integration time-step is calculated based on a mass-spring system which is given by.

$$\Delta t = 0.2 t_{crit} = \sqrt{\frac{m^*}{k^*}} \tag{7.2}$$

where t_{crit} is the critical time-step for a mass-spring system, m^* is the equivalent mass of the smallest particle and k^* is the largest equivalent stiffness in the system (see Section 4.4).

In order to investigate the dependency of the simulation results on the time-step, the simulation of the indentation process with the dimensionless strain rate of 2.2969 (i.e. large strain rate) was performed using different time-steps. The time-step is calculated as follow,

$$\Delta t_d = \zeta . \Delta t \tag{7.3}$$

where ζ is the time-step factor and Δt is the time-step evaluated based on mass-spring theory using Equation (7.2). The average values and the standard deviation of hardness, deviatoric and hydrostatic stresses are plotted in Figure 7.5 as a function of time-step factor.

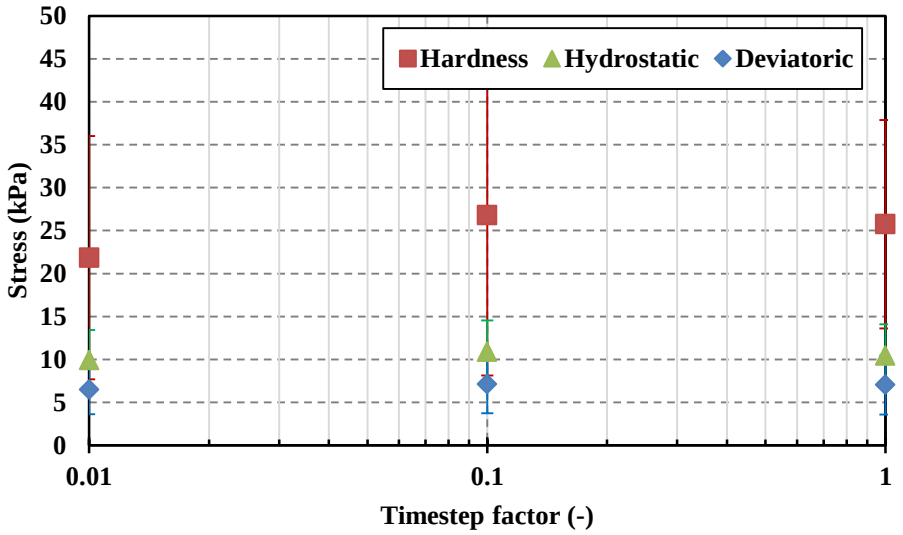

Figure 7.5: Hardness, hydrostatic and deviatoric stresses inside the dynamic bin as functions of time-step factor

The results of the hydrostatic and deviatoric stresses show independency with the time-step for the range investigated here. However, the average value of hardness is slightly smaller for the time-step factor of 0.01 as compared to 0.10 and 1.00. This difference is still negligible relative to the magnitude of the deviations in the system. It can therefore be concluded that the influence of strain rate on the stresses occurring in a bed, subjected to ball indentation, is not an artefact of time-step.

7.4 Conclusions

The hardness, deviatoric and hydrostatic stresses within a bed exposed to ball indentation have been analysed as a function of the indentation strain rate. These stresses are almost constant up to a dimensionless strain rate of 1, though fluctuations begin to increase from $\gamma^* = 0.5$. However, when γ^* is greater than 1, these stresses start increasing with γ^*, with the increase in hardness being the most substantial. The

information obtained here corroborate the trend already reported in the literature and confirm that the ball indentation technique can be used to analyse powder flowability in a wide range of shear rates in a quick and easy way, with the added advantage that only a small quantity of powder is required.

CHAPTER 8 Conclusions and Recommended Future Work

8.1 Conclusions

The overall aim of this PhD was to further the understanding of the ball indentation method using numerical analysis by DEM.

The ball indentation method has the capability of measuring flowability of small quantities of powders at low consolidation stresses. With the aid of DEM simulations, the particle interactions at the microscopic level can be analysed for various particle properties such as size, shape, stiffness and adhesion. In the literature, there are a number of contact models developed for various contacts such as elastic, elasto-plastic, elastic-adhesive and elasto-plastic and adhesive contacts, most of which involve complex mathematical modelling which leads to an increase in the computational cost of the models when impemeneted as a computer code. A new linear elasto-plastic and adhesive contact model for spherical particles was proposed in this work. Plastic deformation of contacts during loading and pure elastic unloading, accompanied by adhesion are considered, for which the pull-off force increases with plastic deformation. Considering the collision of a spherical cohesive body with a rigid flat target, the impact velocity that provides contact breakage in the proposed model was found to be very similar to that of Thornton and Ning's model. The response of coefficient of restitution as a function of impact velocity was also in good agreement with the work of Thornton

and Ning. Sensitivity analyses of the model parameters on work of compaction reveal that by increasing the stiffness ratio (k_e/k_p) the normalised plastic work increases and the normalised elastic work decreases. By increasing the interface energy, the plastic work increases, however the elastic work does not change. This highlights the flexibility of the model in representing a wide range of particulate materials. The linear nature of the model leads to time efficient simulations whilst still capturing the complex material behaviour.

The ball indentation on a compacted assembly of cohesive spheres was simulated using DEM. The hardness of the compacted assembly was evaluated for a range of sample quantities. It was found that a minimum bed height of 20 particle diameters is required in order to achieve reliable hardness values. With small sample sizes, for which the surrounding walls and base of the die constrain the bed deformation, an increase in the resistance of the bed, i.e. an increase in hardness, was observed. It was necessary to have a sufficiently large clearance between the edge of the indentation zone and the die wall, such that the plastic flow of the powder was not constrained by the wall. The penetration depth was normalised with respect to the indenter radius in order to allow the effect of different indenter sizes to be analysed and compared. The penetration depth should be sufficiently large to cause notable bed shear deformation. It was found that this minimum penetration depth was approximately equal to 10% of the indenter radius. A sensitivity analysis of indenter size revealed that indenters with diameters smaller than 16 particle diameters exhibit fluctuations in hardness measurements, whereas indenters with a diameter of up to 22 particle diameters result in stable hardness values, providing the minimum sample criteria were met. As the indenter size decreases, it

approaches the size of bed particles. Therefore, rearrangements at the single particle level influence the force on the indenter throughout the indentation process, resulting in fluctuations in hardness. With very large indenters comparable in size to the die, the measurement of hardness may be affected by the wall.

The hardness and localised hydrostatic and deviatoric stresses were also evaluated for various indenter and inter-particle properties. The hardness measurements were found to be independent of indenter stiffness. An increase in indenter friction slightly increased the hardness, although its influence on the internal stresses was negligible. Cubic and cylindrical indenters measured significantly larger hardness values compared to the spherical indenter. It was shown that with cubic and cylindrical indenters, the powder bed is locally consolidated, hence the measured value of hardness was not representative of the bulk consolidation state. Increasing the inter-particle friction or cohesion resulted in greater hardness values and internal stresses due to the increase in resistance to shear deformation.

The hardness, deviatoric and hydrostatic stresses within a bed exposed to ball indentation were analysed as a function of the indentation strain rate. These stresses were almost constant up to a dimensionless strain rate (γ^*) of 1, though fluctuations began to increase from $\gamma^* = 0.5$. However, when γ^* was greater than 1, these stresses started increasing with γ^*, with the increase in hardness being the most substantial. The information obtained corroborated the trend already reported in the literature and confirmed that the ball indentation technique can be used to analyse powder flowability

in a wide range of shear rates in a quick and easy way, with the added advantage that only a small quantity of powder is required.

8.2 **Recommended Future Work**

Other flowability measurement methods can be simulated with DEM in order to provide comparison with the ball indentation technique. Sensitivity of hardness and internal stresses during the indentation process to particle properties can be investigated for a wider range of properties such as shape, stiffness, and size distribution. The comparison of various techniques and sensitivity analysis of single particle properties can facilitate the development of a model for determination of the constraint factor based on single particle properties.

The proposed contact model was validated by comparison with the well-established model of Thornton and Ning for the case of a particle impacting a flat target at different impact velocities. The proposed contact model can be further validated by comparison with experimental results, both at single particle and bulk scales.

References

[1] J. K. Prescott and R. A. Barnum, "On Powder Flowability," *Pharmaceutical technology,* vol. 24, pp. 60-85, 2000.

[2] A. Fassihi and I. Kanfer, "Effect of Compressibility and Powder Flow Properties on Tablet Weight Variation," *Drug Development and Industrial Pharmacy,* vol. 12, pp. 1947-1966, 1986.

[3] D. Schulze, *Powders and Bulk Solids : Behavior, Characterization, Storage and Flow*. Berlin, Heidelberg: Springer-Verlag Berlin Heidelberg, 2007.

[4] A. Hassanpour and M. Ghadiri, "Characterisation of Flowability of Loosely Compacted Cohesive Powders by Indentation," *Particle & Particle Systems Characterization,* vol. 24, pp. 117-123, 2007.

[5] C. Wang, A. Hassanpour, and M. Ghadiri, "Characterisation of Flowability of Cohesive Powders by Testing Small Quantities of Weak Compacts," *Particuology,* vol. 6, pp. 282-285, 2008.

[6] M. Ghadiri and A. Hassanpour, "Assessing Flowability of Cohesive Powders from a Small Sample Quantity," ed. University of Leeds: EPSRC and Sellafield Ltd, 2009.

[7] U. Zafar, "Characterisation of Flowability of Cohesive Powders by Indentation," PhD, School of Process, Environmental and Materials Engineering, University of Leeds, Leeds, 2013.

[8] J. Schwedes, "Review on Testers for Measuring Flow Properties of Bulk Solids," *Granular Matter,* vol. 5, pp. 1-43, 2003.

[9] A. W. Jenike, *Storage and Flow of Solids*. Salt Lake City, Utah :: University of Utah, 1964.

[10] D. Schulze, "A New Ring Shear Tester for Flowability and Time Consolidation Measurements," in *Proc. 1st International Particle Technology Forum*, 1994, pp. 11-16.

[11] M. D. Ashton, D. C. H. Cheng, R. Farley, and F. H. H. Valentin, "Some Investigations into the Strength and Flow Properties of Powders," *Rheologica Acta,* vol. 4, pp. 206-218, 1965.

[12] A. Castellanos, J. Valverde, and M. Quintanilla, "The Sevilla Powder Tester: A Tool for Characterizing the Physical Properties of Fine Cohesive Powders at Very Small Consolidations," *Kona,* vol. 22, pp. 66-81, 2004.

[13] R. L. Carr, "Particle Behavior Storage and Flow," *Mechanical Engineering,* vol. 91, pp. 43-&, 1969.

[14] Y. B. Jiang, S. Matsusaka, H. Masuda, and T. Yokoyama, "Evaluation of Flowability of Composite Particles and Powder Mixtures by a Vibrating Capillary Method," *Journal of Chemical Engineering of Japan,* vol. 39, pp. 14-21, 2006.

[15] G. Mojtaba, "Hardness, Stiffness, and Toughness of Particles," in *Powder Technology Handbook, Third Edition*, ed: CRC Press, 2006.

[16] D. Tabor, *The Hardness of Metals*: Clarendon Press, 1951.

[17] J. Harris and H. Stöcker, *Handbook of Mathematics and Computational Science*. New York: Springer, 1998.

[18] G. V. Kozlov, V. D. Serdyuk, and V. A. Beloshenko, "The Plastic Constraint Factor and Mechanical Properties of a High-Density Polyethylene on Impact Loading," *Mechanics of Composite Materials,* vol. 30, pp. 506-509, 1995.
[19] R. Hill, *The Mathematical Theory of Plasticity* vol. 11: Oxford University Press, USA, 1998.
[20] K. L. Johnson, *Contact Mechanics*: Cambridge University Press, 1985.
[21] Z. Zatloukal and Z. Šklubalová, "Indentation Test for Free-Flowable Powder Excipients," *Pharmaceutical Development and Technology,* vol. 13, pp. 85-92, 2008.
[22] P. A. Cundall and O. D. L. Strack, "A Discrete Numerical Model for Granular Assemblies," *Géotechnique,* vol. 29, pp. 47-65, 1979.
[23] H. P. Zhu, Z. Y. Zhou, R. Y. Yang, and A. B. Yu, "Discrete Particle Simulation of Particulate Systems: Theoretical Developments," *Chemical Engineering Science,* vol. 62, pp. 3378-3396, 2007.
[24] H. P. Zhu, Z. Y. Zhou, R. Y. Yang, and A. B. Yu, "Discrete Particle Simulation of Particulate Systems: A Review of Major Applications and Findings," *Chemical Engineering Science,* vol. 63, pp. 5728-5770, 2008.
[25] Z. Ning and M. Ghadiri, "Distinct Element Analysis of Attrition of Granular Solids under Shear Deformation," *Chemical Engineering Science,* vol. 61, pp. 5991-6001, 2006.
[26] DEM-Solutions, "Edem User Manual," DEM-Solutions, Ed., ed: DEM-Solutions, 2009.
[27] J. Visser, "Van Der Waals and Other Cohesive Forces Affecting Powder Fluidization," *Powder Technology,* vol. 58, pp. 1-10, 1989.
[28] H. C. Hamaker, "The London—Van Der Waals Attraction between Spherical Particles," *Physica,* vol. 4, pp. 1058-1072, 1937.
[29] J. P. K. Seville, C. D. Willett, and P. C. Knight, "Interparticle Forces in Fluidisation: A Review," *Powder Technology,* vol. 113, pp. 261-268, 2000.
[30] H. Hertz, *Crellés J.,* vol. 92, p. 156, 1882.
[31] C. Thornton and Z. Ning, "A Theoretical Model for the Stick/Bounce Behaviour of Adhesive, Elastic-Plastic Spheres," *Powder Technology,* vol. 99, pp. 154-162, 1998.
[32] R. D. Mindlin and H. Deresiewicz, "Elastic Spheres in Contact under Varying Oblique Forces," *Journal of Applied Mechanics,* vol. 20, pp. 327-344, 1953.
[33] J. S. Courtney-Pratt and E. Eisner, "The Effect of a Tangential Force on the Contact of Metallic Bodies," *Proceedings of the Royal Society of London. Series A. Mathematical and Physical Sciences,* vol. 238, pp. 529-550, 1957.
[34] R. D. Mindlin, *J. Ap. Mech.,* p. 259, 1949.
[35] A. Di Renzo and F. P. Di Maio, "Comparison of Contact-Force Models for the Simulation of Collisions in Dem-Based Granular Flow Codes," *Chemical Engineering Science,* vol. 59, pp. 525-541, 2004.
[36] A. H. Kharaz, D. A. Gorham, and A. D. Salman, "An Experimental Study of the Elastic Rebound of Spheres," *Powder Technology,* vol. 120, pp. 281-291, 2001.
[37] A. Di Renzo and F. P. Di Maio, "An Improved Integral Non-Linear Model for the Contact of Particles in Distinct Element Simulations," *Chemical Engineering Science,* vol. 60, pp. 1303-1312, 2005.

[38] C. Thornton, "Coefficient of Restitution for Collinear Collisions of Elastic-Perfectly Plastic Spheres," *Journal of Applied Mechanics, Transactions ASME,* vol. 64, pp. 383-386, 1997.

[39] L. Vu-Quoc and X. Zhang, "An Elastoplastic Contact Force-Displacement Model in the Normal Direction: Displacement-Driven Version," *Proceedings of the Royal Society of London Series a-Mathematical Physical and Engineering Sciences,* vol. 455, pp. 4013-4044, 1999.

[40] L. Vu-Quoc, X. Zhang, and L. Lesburg, "A Normal Force-Displacement Model for Contacting Spheres Accounting for Plastic Deformation: Force-Driven Formulation," *Journal of Applied Mechanics-Transactions of the Asme,* vol. 67, pp. 363-371, 2000.

[41] O. R. Walton and R. L. Braun, "Viscosity, Granular-Temperature, and Stress Calculations for Shearing Assemblies of Inelastic, Frictional Disks," *Journal of Rheology,* vol. 30, pp. 949-980, 1986.

[42] C. E. Smith and P. P. Liu, "Coefficients of Restitution," *Journal of Applied Mechanics-Transactions of the Asme,* vol. 59, pp. 963-969, 1992.

[43] L. Vu-Quoc, X. Zhang, and L. Lesburg, "Normal and Tangential Force–Displacement Relations for Frictional Elasto-Plastic Contact of Spheres," *International Journal of Solids and Structures,* vol. 38, pp. 6455-6489, 2001.

[44] Z. Ning, "Elasto-Plastic Impact of Fine Particles and Fragmentation of Small Agglomerates," Doctor of Philosophy, The University of Aston, Birmingham, 1995.

[45] K. L. Johnson, K. Kendall, and A. D. Roberts, "Surface Energy and the Contact of Elastic Solids," *Proceedings of the Royal Society of London. A. Mathematical and Physical Sciences,* vol. 324, pp. 301-313, 1971.

[46] C. Thornton and K. K. Yin, "Impact of Elastic Spheres with and without Adhesion," *Powder Technology,* vol. 65, pp. 153-166, 1991.

[47] A. R. Savkoor and G. A. D. Briggs, "Effect of Tangential Force on Contact of Elastic Solids in Adhesion," *Proceedings of the Royal Society of London Series a-Mathematical Physical and Engineering Sciences,* vol. 356, pp. 103-114, 1977.

[48] B. J. Briscoe and S. L. Kremnitzer, "Study of the Friction and Adhesion of Polyethylene-Terephthalate Monofilaments," *Journal of Physics D-Applied Physics,* vol. 12, pp. 505-&, 1979.

[49] B. V. Derjaguin, V. M. Muller, and Y. P. Toporov, "Effect of Contact Deformations on the Adhesion of Particles," *Journal of Colloid and Interface Science,* vol. 53, pp. 314-326, 1975.

[50] M. D. Pashley, "Further Consideration of the Dmt Model for Elastic Contact," *Colloids and Surfaces,* vol. 12, pp. 69-77, 1984.

[51] V. M. Muller, V. S. Yushchenko, and B. V. Derjaguin, "On the Influence of Molecular Forces on the Deformation of an Elastic Sphere and Its Sticking to a Rigid Plane," *Journal of Colloid and Interface Science,* vol. 77, pp. 91-101, 1980.

[52] H. G. Matuttis and A. Schinner, "Particle Simulation of Cohesive Granular Materials," *International Journal of Modern Physics C,* vol. 12, pp. 1011-1021, 2001.

[53] A. Hassanpour, M. Pasha, L. Susana, N. Rahmanian, A. C. Santomaso, and M. Ghadiri, "Analysis of Seeded Granulation in High Shear Granulators by Discrete Element Method," *Powder Technology*.

[54] C. Hare, M. Ghadiri, and R. Dennehy, "Prediction of Attrition in Agitated Particle Beds," *Chemical Engineering Science,* vol. 66, pp. 4757-4770, 2011.

[55] J. Tomas, "Adhesion of Ultrafine Particles—a Micromechanical Approach," *Chemical Engineering Science,* vol. 62, pp. 1997-2010, 2007.

[56] A. Hassanpour, C. C. Kwan, B. H. Ng, N. Rahmanian, Y. L. Ding, S. J. Antony, *et al.*, "Effect of Granulation Scale-up on the Strength of Granules," *Powder Technology,* vol. 189, pp. 304-312, 2009.

[57] S. Luding, "Cohesive, Frictional Powders: Contact Models for Tension," *Granular Matter,* vol. 10, pp. 235-246, 2008.

[58] S. Luding, Personal Communication, in International Symposium on Discrete Element Modelling of Particulate Media, University of Birmingham,30/03/2012

[59] S. Luding, K. Manetsberger, and J. Müllers, "A Discrete Model for Long Time Sintering," *Journal of the Mechanics and Physics of Solids,* vol. 53, pp. 455-491, 2005.

[60] J. F. Favier, M. H. Abbaspour-Fard, M. Kremmer, and A. O. Raji, "Shape Representation of Axisymmetrical, Non-Spherical Particles in Discrete Element Simulation Using Multi-Element Model Particles," *Engineering Computations,* vol. 16, pp. 467-480, 1999.

[61] J. Cordelair and P. Greil, "Discrete Element Modeling of Solid Formation During Electrophoretic Deposition," *Journal of Materials Science,* vol. 39, pp. 1017-1021, 2004.

[62] J. M. Ting, L. Meachum, and J. D. Rowell, "Effect of Particle Shape on the Strength and Deformation Mechanisms of Ellipse-Shaped Granular Assemblages," *Engineering Computations,* vol. 12, pp. 99-108, 1995.

[63] P. W. Cleary, "Dem Prediction of Industrial and Geophysical Particle Flows," *Particuology,* vol. 8, pp. 106-118, 2010.

[64] J. K. Morgan, "Particle Dynamics Simulations of Rate- and State-Dependent Frictional Sliding of Granular Fault Gouge," *Pure and Applied Geophysics,* vol. 161, pp. 1877-1891, 2004.

[65] T. T. Ng and R. Dobry, "A Non-Linear Numerical Model for Soil Mechanics," *International Journal for Numerical and Analytical Methods in Geomechanics,* vol. 16, pp. 247-263, 1992.

[66] K. Iwashita and M. Oda, "Rolling Resistance at Contacts in Simulation of Shear Band Development by Dem," *Journal of Engineering Mechanics-Asce,* vol. 124, pp. 285-292, 1998.

[67] J. F. Favier, M. H. Abbaspour-Fard, and M. Kremmer, "Modeling Nonspherical Particles Using Multisphere Discrete Elements," *Journal of Engineering Mechanics-Asce,* vol. 127, pp. 971-977, 2001.

[68] W. R. Ketterhagen, M. T. A. Ende, and B. C. Hancock, "Process Modeling in the Pharmaceutical Industry Using the Discrete Element Method," *Journal of Pharmaceutical Sciences,* vol. 98, pp. 442-470, 2009.

[69] M. Kodam, R. Bharadwaj, J. Curtis, B. Hancock, and C. Wassgren, "Force Model Considerations for Glued-Sphere Discrete Element Method Simulations," *Chemical Engineering Science,* vol. 64, pp. 3466-3475, 2009.

[70] H. Kruggel-Emden, S. Rickelt, S. Wirtz, and V. Scherer, "A Study on the Validity of the Multi-Sphere Discrete Element Method," *Powder Technology,* vol. 188, pp. 153-165, 2008.

[71] E. Azema, F. Radjai, and G. Saussine, "Quasistatic Behavior and Force Transmission in Packing of Irregular Polyhedral Particles," in *Powders and Grains 2009*. vol. 1145, M. Nakagawa and S. Luding, Eds., ed, 2009, pp. 273-276.

[72] C. Hogue, "Shape Representation and Contact Detection for Discrete Element Simulations of Arbitrary Geometries," *Engineering Computations,* vol. 15, pp. 374-+, 1998.

[73] K. C. Smith, T. S. Fisher, and M. Alam, "Quasi-Static Compaction of Polyhedra by the Discrete Element Method," in *Powders and Grains 2009*. vol. 1145, M. Nakagawa and S. Luding, Eds., ed, 2009, pp. 90-93.

[74] L. Pournin, M. Tsukahara, and T. M. Liebling, "Particle Shape Versus Friction in Granular Jamming," in *Powders and Grains 2009*. vol. 1145, M. Nakagawa and S. Luding, Eds., ed, 2009, pp. 499-502.

[75] F. Alonso-Marroquin, S.-A. Galindo-Torres, A. Tordesillas, and Y. Wang, "New Perspectives for Discrete Element Modeling: Merging Computational Geometry and Molecular Dynamics," in *Powders and Grains 2009*. vol. 1145, M. Nakagawa and S. Luding, Eds., ed, 2009, pp. 825-828.

[76] G. W. Delaney and P. W. Cleary, "Fundamental Relations between Particle Shape and the Properties of Granular Packings," in *Powders and Grains 2009*. vol. 1145, M. Nakagawa and S. Luding, Eds., ed, 2009, pp. 837-840.

[77] X. Jia, M. Gan, R. A. Williams, and D. Rhodes, "Validation of a Digital Packing Algorithm in Predicting Powder Packing Densities," *Powder Technology,* vol. 174, pp. 10-13, 2007.

[78] C. Thornton, Personal Communication, in International Symposium on Discrete Element Modelling of Particulate Media, University of Birmingham,30/03/2012

[79] P. Digitizer, "Plot Digitizer," 2.0 ed: GNU General Public License version 2.0 (GPLv2), 2012.

[80] S. Wall, W. John, H. C. Wang, and S. L. Goren, "Measurements of Kinetic-Energy Loss for Particles Impacting Surfaces," *Aerosol Science and Technology,* vol. 12, pp. 926-946, 1990.

[81] A. H. Kharaz and D. A. Gorham, "A Study of the Restitution Coefficient in Elastic-Plastic Impact," *Philosophical Magazine Letters,* vol. 80, pp. 549-559, 2000.

[82] G. I. Tardos, S. McNamara, and I. Talu, "Slow and Intermediate Flow of a Frictional Bulk Powder in the Couette Geometry," *Powder Technology,* vol. 131, pp. 23-39, 2003.

[83] K. Bagi, "Stress and Strain in Granular Assemblies," *Mechanics of Materials,* vol. 22, pp. 165-177, 1996.

[84] S. B. Savage, "Gravity Flow of Cohesionless Granular Materials in Chutes and Channels," *Journal of Fluid Mechanics,* vol. 92, pp. 53-96, 1979.

[85] S. B. Savage and M. Sayed, "Stresses Developed by Dry Cohesionless Granular Materials Sheared in an Annular Shear Cell," *Journal of Fluid Mechanics,* vol. 142, pp. 391-430, 1984.

[86] R. A. Bagnold, "Experiments on a Gravity-Free Dispersion of Large Solid Spheres in a Newtonian Fluid under Shear," *Proceedings of the Royal Society of London. Series A. Mathematical and Physical Sciences,* vol. 225, pp. 49-63, 1954.

[87] C. S. Campbell and C. E. Brennen, "Computer Simulation of Granular Shear Flows," *Journal of Fluid Mechanics,* vol. 151, pp. 167-188, 1985.

[88] S. B. Savage and S. McKeown, "Shear Stresses Developed During Rapid Shear of Concentrated Suspensions of Large Spherical-Particles between Concentric Cylinders," *Journal of Fluid Mechanics,* vol. 127, pp. 453-472, 1983.

[89] R. Freeman, "Measuring the Flow Properties of Consolidated, Conditioned and Aerated Powders — a Comparative Study Using a Powder Rheometer and a Rotational Shear Cell," *Powder Technology,* vol. 174, pp. 25-33, 2007.

[90] R. Moreno-Atanasio, S. J. Antony, and M. Ghadiri, "Analysis of Flowability of Cohesive Powders Using Distinct Element Method," *Powder Technology,* vol. 158, pp. 51-57, 2005.

Appendix I: Derivation of Work of Adhesion and Pull-off Force of the Proposed Contact Model

The work of adhesion, W_{ad}, is the area under the unloading response from α_{fp} to α_p which consists of a trapezium from α_{fp} to α_{cp} and a triangle from α_{cp} to α_p. Hence,

$$\begin{aligned}|W_{ad}| &= \frac{1}{2}\left(\alpha_{cp}-\alpha_{fp}\right)\left(\left[\frac{5}{9}+\frac{9}{9}\right]f_{cp}\right)+\frac{1}{2}\left(\alpha_p-\alpha_{cp}\right)\left(\frac{9}{9}f_{cp}\right)\\ &= \frac{5}{18}f_{cp}\alpha_{cp}-\frac{14}{18}f_{cp}\alpha_{fp}+\frac{9}{18}f_{cp}\alpha_p\end{aligned} \tag{A1.1}$$

At overlap α_{cp} we have:

$$\begin{aligned}-f_{cp} &= k_e\alpha_{cp}-k_e\alpha_p\\ \Rightarrow f_{cp} &= k_e\alpha_p-k_e\alpha_{cp}\end{aligned} \tag{A1.2}$$

Substituting Equation (A1.2) in (A1.1) and factorising $k_e/18$ gives,

$$|W_{ad}| = \frac{k_e}{18}\left(-5\alpha_{cp}^2+\left(-4\alpha_p+14\alpha_{fp}\right)\alpha_{cp}+9\alpha_p^2-14\alpha_p\alpha_{fp}\right) \tag{A1.3}$$

At overlap α_{fp} we have:

$$\begin{aligned}-\frac{5}{9}f_{cp} &= -k_e\alpha_{fp}+2k_e\alpha_{cp}-k_e\alpha_p\\ \Rightarrow \alpha_{fp} &= \left(2\alpha_{cp}-\alpha_p+\frac{5}{9k_e}f_{cp}\right)\end{aligned} \tag{A1.4}$$

Substituting Equation (A1.2) in (A1.4) gives,

$$\alpha_{fp} = \frac{13}{9}\alpha_{cp}-\frac{4}{9}\alpha_p \tag{A1.5}$$

Substituting Equation (A1.5) in (A1.3) and factorising 137/9 gives,

$$|W_{ad}| = \frac{137}{162} k_e \left(\alpha_{cp}^2 - 2\alpha_p \alpha_{cp} + \alpha_p^2 \right) \tag{A1.6}$$

The work of adhesion, W_{ad}, can also be evaluated by $A_p\Gamma$, where A_p is the plastic contact area given by Equation and Γ is the energy density (see Section 4.1.1).

$$A_p = \pi \left(2R^* \alpha_{pd} - \alpha_{pd}^2 \right) \tag{A1.7}$$

where α_{pd} is the plastic deformation given by (see Section 4.1.1),

$$\alpha_{pd} = \alpha_p - \alpha_0 \tag{A1.8}$$

Substituting Equation (A1.8) in (A1.7) gives,

$$A_p = \pi \left(2R^* \alpha_p - 2R^* \alpha_0 - \alpha_p^2 - \alpha_0^2 + 2\alpha_p \alpha_0 \right) \tag{A1.9}$$

Hence the work of adhesion is,

$$|W_{ad}| = 2\pi\Gamma R^* \alpha_p - 2\pi\Gamma R^* \alpha_0 - \pi\Gamma \alpha_p^2 - \pi\Gamma \alpha_0^2 + 2\pi\Gamma \alpha_p \alpha_0 \tag{A1.10}$$

Equating the right hand sides of Equation (A1.6) and (A1.10) gives,

$$\alpha_{cp}^2 - 2\alpha_p \alpha_{cp} + C = 0 \tag{A1.11}$$

where C is given by,

$$C = \frac{162}{137 k_e} \left(\left(\frac{137}{162} k_e + \pi\Gamma \right) \alpha_p^2 - 2\pi\Gamma \left(R^* + \alpha_0 \right) \alpha_p + \pi\Gamma \alpha_0^2 + 2\pi\Gamma R^* \alpha_0 \right) \tag{A1.12}$$

Equation (A1.11) is a quadric equation; therefore there are two possible solutions:

$$\alpha_{cp} = \begin{cases} \alpha_p - \sqrt{\alpha_p^2 - C} \\ \\ \alpha_p + \sqrt{\alpha_p^2 - C} \end{cases} \tag{A1.13}$$

In order to verify which of the two solutions, given by Equation (A1.13), is suitable, the elastic and plastic forces as functions of α_{cp} is plotted using both the solutions in Figure A1.1.

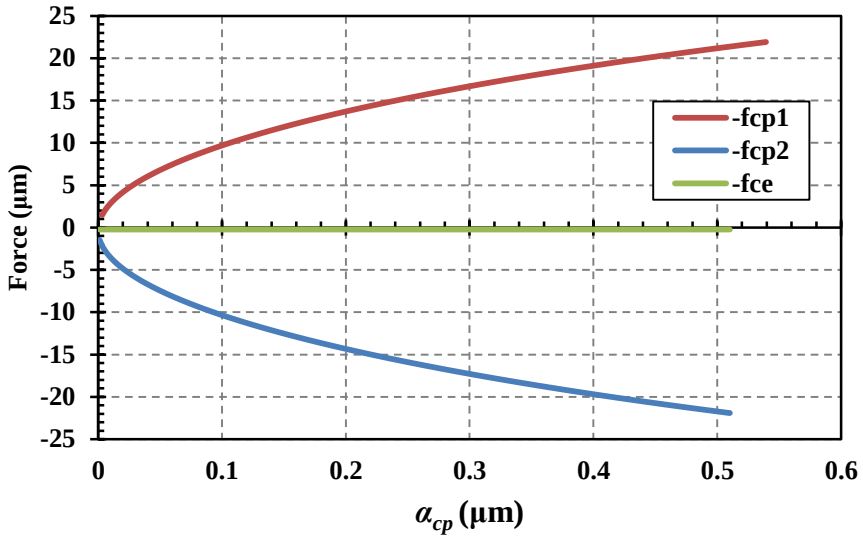

Figure A1.1: Plastic and elastic pull-off forces as functions of α_{cp} using the solutions provided in Equation (A1.13), where f_{cp1} and f_{cp2} are evaluated using the first and second solutions, respectively.

For the responses in Figure A1.1, k_e = 1500 N/m, k_p = 210 N/m, Γ = 0.02 J/m^2 and R^* = 2.45 μm. The selection of these values is described in 4.1.1. As it can be seen, using the first solution of Equation (A1.13) provides a positive value of $-f_{cp}$. Hence the second solution of Equation (A1.13) is the correct one,

$$\alpha_{cp} = \alpha_p - \sqrt{\alpha_p^2 - C} \tag{A1.14}$$

Appendix II: Derivation of Impact, Rebound and Critical Sticking Velocities in the Proposed Contact Model

In this section, the equations for the impact, rebound and sticking velocities are derived based on applying an energy balance during contact loading and unloading. Figure A2.1 shows schematically the force-overlap response of the proposed model. Different areas under the response, which correspond to different energies, are shaded and coloured.

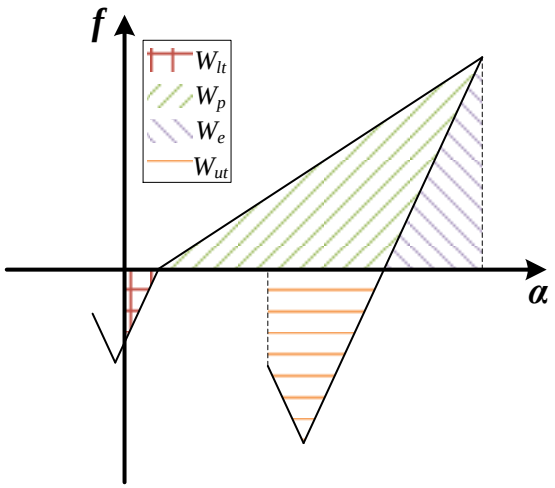

Figure A2.1: Schematic force-overlap response of the proposed model

In Figure A2.1 W_{lt}, W_p, W_e and W_{ut} correspond to the initial loading tensile work, plastic work, elastic work and unloading tensile work, respectively. The impact energy balance from the initial velocity to the point where the sphere is brought to rest, E_i, is,

$$E_i = \frac{1}{2} m v_i^2 = W_p + W_e - |W_{lt}| \tag{A2.1}$$

where v_i is the impact velocity. W_p is the triangular area under the curve between α_0 and α_p. W_e is the triangular area under the curve between α_p and α_{max}. Hence $W_p + W_e$ is the triangulate area between α_0 and α_{max},

$$W_p + W_e = \frac{1}{2} F_{\max} \left(\alpha_{\max} - \alpha_0 \right) \tag{A2.2}$$

At α_{max} we have,

$$F_{\max} = k_p \left(\alpha_{\max} - \alpha_0 \right) \tag{A2.3}$$

Substituting Equation (A2.3) in (A2.2) gives,

$$W_p + W_e = \frac{1}{2} k_p \left(\alpha_{\max} - \alpha_0 \right) \left(\alpha_{\max} - \alpha_0 \right) = \frac{1}{2} k_p \left(\alpha_{\max} - \alpha_0 \right)^2 \tag{A2.4}$$

W_{lt} is the negative triangular area under the curve between $\alpha = 0$ and α_0, hence,

$$|W_{lt}| = \frac{1}{2} \frac{8}{9} f_{ce} \alpha_0 \tag{A2.5}$$

At α_0 we have,

$$\begin{aligned} & k_e \alpha_0 - \frac{8}{9} f_{ce} = 0 \\ & \Rightarrow \frac{8}{9} f_{ce} = k_e \alpha_0 \end{aligned} \tag{A2.6}$$

Substituting Equation (A2.6) in (A2.5) gives,

$$|W_{lt}| = \frac{1}{2} k_e \alpha_0^2 \tag{A2.7}$$

Substituting Equations (A2.4) and (A2.7) in (A2.1) gives,

$$v_i = \left(\frac{k_p \left(\alpha_{\max} - \alpha_0 \right)^2 - k_e \alpha_0^2}{m} \right)^{1/2} \tag{A2.8}$$

The critical sticking velocity, v_s, is the maximum impact velocity by which, the contact does not break. Hence,

$$W_e = |W_{ut}| \quad \rightarrow \quad v_i = v_s \tag{A2.9}$$

For impact velocities larger than v_s, the unloading leads to detachment of the contact. The rebound velocity, v_r, can be derived based on the following energy balance,

$$E_r = \frac{1}{2} m v_r^2 = W_e - |W_{ut}| \tag{A2.10}$$

W_e is the triangular area under the curve between α_p and α_{max}, hence,

$$W_e = \frac{1}{2} F_{\max} \left(\alpha_{\max} - \alpha_p \right) \tag{A2.11}$$

Substituting Equation (A2.3) in (A2.11) gives,

$$W_e = \frac{1}{2} k_e \left(\alpha_{\max} - \alpha_0 \right) \left(\alpha_{\max} - \alpha_p \right) \tag{A2.12}$$

W_{ut} is the negative area under the curve between α_p and α_{fp}, hence,

$$|W_{ut}| = |A_{cp-fp}| + |A_{c0-cp}| + |A_{p-c0}| \tag{A2.13}$$

where $A_{cp\text{-}fp}$ is the negative trapezial area between α_{cp} and α_{fp}, $A_{c0\text{-}cp}$ is the negative trapezial area between α_{c0} and α_{cp}, and $A_{p\text{-}c0}$ is the negative triangular area between α_p and α_{c0}. Hence,

$$\begin{aligned} |W_{ut}| &= \frac{1}{2}\left[\left(\frac{5}{9} f_{cp} + f_{cp} \right) \left(\alpha_{cp} - \alpha_{fp} \right) + \left(\frac{8}{9} f_{cp} + f_{cp} \right) \left(\alpha_{co} - \alpha_{cp} \right) + \left(\frac{8}{9} f_{cp} \right) \left(\alpha_p - \alpha_{c0} \right) \right] \\ &= \frac{1}{2}\left(-\frac{3}{9} f_{cp}\alpha_{cp} - \frac{14}{9} f_{cp}\alpha_{fp} + \frac{9}{9} f_{cp}\alpha_{c0} + \frac{8}{9} f_{cp}\alpha_p \right) \\ &= \frac{1}{2} \frac{f_{cp}}{9} \left(-3\alpha_{cp} - 14\alpha_{fp} + 9\alpha_{c0} + 8\alpha_p \right) \end{aligned} \tag{A2.14}$$

Substituting Equation (A2.12) and (A2.14) in (A2.10) gives,

$$v_r = \left(\frac{k_p \left(\alpha_{\max} - \alpha_0\right)\left(\alpha_{\max} - \alpha_p\right) - \frac{f_{cp}}{9}\left(-3\alpha_{cp} - 14\alpha_{fp} + 9\alpha_{c0} + 8\alpha_p\right)}{m} \right)^{1/2} \qquad \text{(A2.15)}$$

Appendix III: Derivation of Impact and Rebound Velocities in the Proposed Simplified Contact Model and Luding's Model

In this section, the equations for the impact, rebound and sticking velocities are derived based on applying an energy balance during contact loading and unloading for the simplified version of the proposed model and the model of Luding. Figure A3.1 shows schematically the force-overlap response of the two models. Different areas under the response, which correspond to different energies, are shaded and coloured.

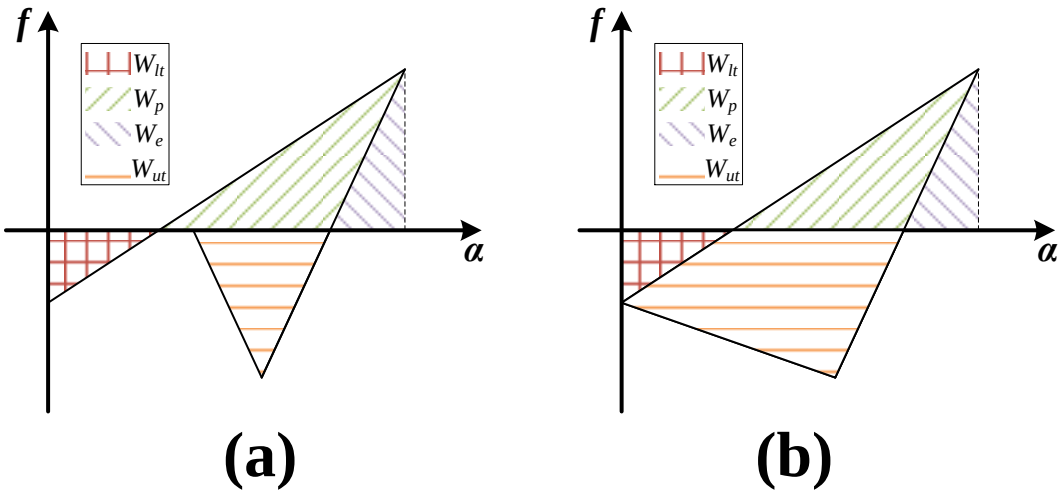

Figure A3.1: Schematic force-overlap response of (a) the simplified version of the proposed model and (b) Luding's model

In Figure A3.1 W_{lt}, W_p, W_e and W_{ut} correspond to the initial loading tensile work, plastic work, elastic work and unloading tensile work, respectively. The impact energy for both of the models is identical since the loading path is the same. Hence,

$$E_i = \frac{1}{2} m v_i^2 = W_e + W_p - |W_{lt}| \tag{A3.1}$$

where $W_e + W_p$ form a triangle from α_0 to α_{max} with a height of F_{max}, thus:

$$W_p + W_e = \frac{1}{2} F_{\max} \left(\alpha_{\max} - \alpha_0 \right) \tag{A3.2}$$

where the maximum contact force, F_{max}, is given by,

$$F_{\max} = k_p \alpha_{\max} - \frac{8}{9} f_{ce} = k_p \alpha_{\max} - k_p \alpha_0 = k_p \left(\alpha_{\max} - \alpha_0 \right) \tag{A3.3}$$

Substituting Equation (A3.3) in (A3.2) gives,

$$W_p + W_e = \frac{1}{2} k_p \left(\alpha_{\max} - \alpha_0 \right)^2 \tag{A3.4}$$

W_{lt} is the initial negative tensile work from $\alpha = 0$ to α_0 which is given by,

$$|W_{lt}| = \frac{1}{2} \frac{8}{9} f_{ce} \alpha_0 = \frac{1}{2} k_p \alpha_0 \alpha_0 = \frac{1}{2} k_p \alpha_0^2 \tag{A3.5}$$

Substituting Equation (A3.4) and (A3.5) in (A3.1) gives,

$$v_i = \left(\frac{k_p}{m} \left(\alpha_{\max} - \alpha_0 \right)^2 - \frac{k_p}{m} \alpha_0^2 \right)^{1/2} = \left(\frac{k_p}{m} \left(\alpha_{\max}^2 - 2\alpha_0 \alpha_{\max} \right) \right)^{1/2} \tag{A3.6}$$

The rebound kinetic energy is different for the two model since the work of adhesion is different. The rebound kinetic energy is subtraction of work of adhesion from the elastic strain energy W_e. If this subtraction results in a negative value i.e. if W_e is smaller than work of adhesion the contact does not break and therefore the rebound kinetic energy is zero. The elastic strain energy W_e is the same for both the models which is given by,

$$W_e = \frac{1}{2} F_{\max} \left(\alpha_{\max} - \alpha_p \right) \tag{A3.7}$$

The work of adhesion in the simplified version of the proposed model is $|W_{ut}|$,

$$W_{ad} = |W_{ut}| = \frac{1}{2} f_{cp} \left(\alpha_p - \alpha_{fp} \right) \tag{A3.8}$$

Therefore the rebound velocity is given by,

$$v_r = \left(\frac{2}{m} E_r \right)^{1/2} = \left(\frac{2}{m} \left(W_e - W_{ad} \right) \right)^{1/2} = \left(\frac{F_{\max}}{m} \left(\alpha_{\max} - \alpha_p \right) - \frac{f_{cp}}{m} \left(\alpha_p - \alpha_{fp} \right) \right)^{1/2} \tag{A3.9}$$

The work of adhesion in Luding's model is $|W_{lt}| + |W_{ut}|$ that forms a shape which consists of a trapezium and a triangle. The trapezium has a height of $8/9 f_{ce}$ and bases of α_p and α_{fe}, where α_{fe} is the overlap at which the unloading contact force is equal to $-8/9 f_{ce}$. The triangle has a height of $f_{cp} - 8/9 f_{ce}$ and a base of α_{fe}. Therefore the work of adhesion in Luding's model can be derived as follows,

$$\begin{aligned} W_{ad} &= \frac{1}{2}\frac{8}{9} f_{ce} \left(\alpha_p + \alpha_{fe} \right) + \frac{1}{2} \alpha_{fe} \left(f_{cp} - \frac{8}{9} f_{ce} \right) \\ \therefore W_{ad} &= \frac{1}{2}\frac{8}{9} f_{ce} \alpha_p + \frac{1}{2}\frac{8}{9} f_{ce} \alpha_{fe} + \frac{1}{2} f_{cp} \alpha_{fe} - \frac{1}{2}\frac{8}{9} f_{ce} \alpha_{fe} \\ \therefore W_{ad} &= \frac{1}{2}\frac{8}{9} f_{ce} \alpha_p + \frac{1}{2} f_{cp} \alpha_{fe} \end{aligned} \tag{A3.10}$$

Therefore the rebound velocity of Luding's model is given by,

$$v_r = \left(\frac{2}{m} E_r \right)^{1/2} = \left(\frac{2}{m} \left(W_e - W_{ad} \right) \right)^{1/2} = \left(\frac{F_{\max}}{m} \left(\alpha_{\max} - \alpha_p \right) - \frac{8}{9m} f_{ce} \alpha_p - \frac{f_{cp}}{m} \alpha_{fe} \right)^{1/2}$$

(A3.11)

Appendix IV: Implementation of Stress Calculations in EDEM® Software

The aim is to implement calculations of stress tensor for individual particles and arbitrary measurement volume based on Equations (A4.1) and (A4.2), respectively.

$$\sigma_{ij} = -\frac{1}{V_p}\sum_{N_c}\left|x_i^c - x_i^p\right| n_i F_j \tag{A4.1}$$

$$\sigma_{ij} = -\frac{1}{V}\sum_{N_p}\sum_{N_c}\left|x_i^c - x_i^p\right| n_i F_j \tag{A4.2}$$

where σ_{ij} is the ij-component of stress tensor, V is the volume of the measurement space, N_p is number of particles in the bin, N_c is the number of contacts around particle p, x_i^c, x_i^p and n_i are the i-components of contact location, particle centre and normal vector directed from a particle centroid to its contact, respectively, and F_j is the j-component of the contact force [83].

In EDEM® software, custom particle properties can be implemented. The data for such properties will be available in the analyst part of the software. The minimum, maximum and average values of the properties amongst the whole population of the particles or particles within a desired measurement volume in the simulation can be extracted. Additionally the "total value", which is the summation of the values of the properties, can be extracted again for the whole population of particles or the particles within a

measurement volume. For each of the custom properties, it is possible to define number of elements. For this case, 9 elements are required to represent the stress tensor. In the software two custom properties were defined, "Particle Stress" and "Bin Stress", representing the stress tensor for individual particles and the measurement volume, respectively. In EDEM® software only one-dimensional arrays are allowed for custom properties, hence the two custom properties are considered to be vectors with 9 elements. The indexing of these vectors is shown in

$$\sigma_{ij} = \begin{bmatrix} \sigma_{xx} & \sigma_{xy} & \sigma_{xz} \\ \sigma_{yx} & \sigma_{yy} & \sigma_{yz} \\ \sigma_{zx} & \sigma_{zy} & \sigma_{zz} \end{bmatrix} \rightarrow \text{Custom Property} = \begin{bmatrix} \sigma_{xx} & \sigma_{xy} & \sigma_{xz} & \sigma_{yx} & \sigma_{yy} & \sigma_{yz} & \sigma_{zx} & \sigma_{zy} & \sigma_{zz} \end{bmatrix} \tag{A4.3}$$

In Equation (A4.2) the summation $\sum_{N_p}$ can be performed as a post-analysis process for which the "total value" of $\sum_{N_c} \left| x_i^c - x_i^p \right| n_i F_j$ can be extracted for a measurement volume. The division by the volume of the measurement volume can also be performed in the post-analysis since the volume is arbitrary. This shows that only $\sum_{N_c} \left| x_i^c - x_i^p \right| n_i F_j$ is needed to be evaluated. This was implemented in EDEM® software as a subroutine and the value was assigned to "Bin Stress",

$$\text{Bin Stress}_{ij} = \sum_{N_c} \left| x_i^c - x_i^p \right| n_i F_j \tag{A4.4}$$

For evaluation of particle stress tensor the value of "Bin Stress" is divided the volume of the particle,

$$\text{Particle Stress}_{ij} = \frac{1}{V_p} \sum_{N_c} \left| x_i^c - x_i^p \right| n_i F_j \tag{A4.5}$$

Figure A4.1 shows the available options for two custom particle properties in EDEM® software.

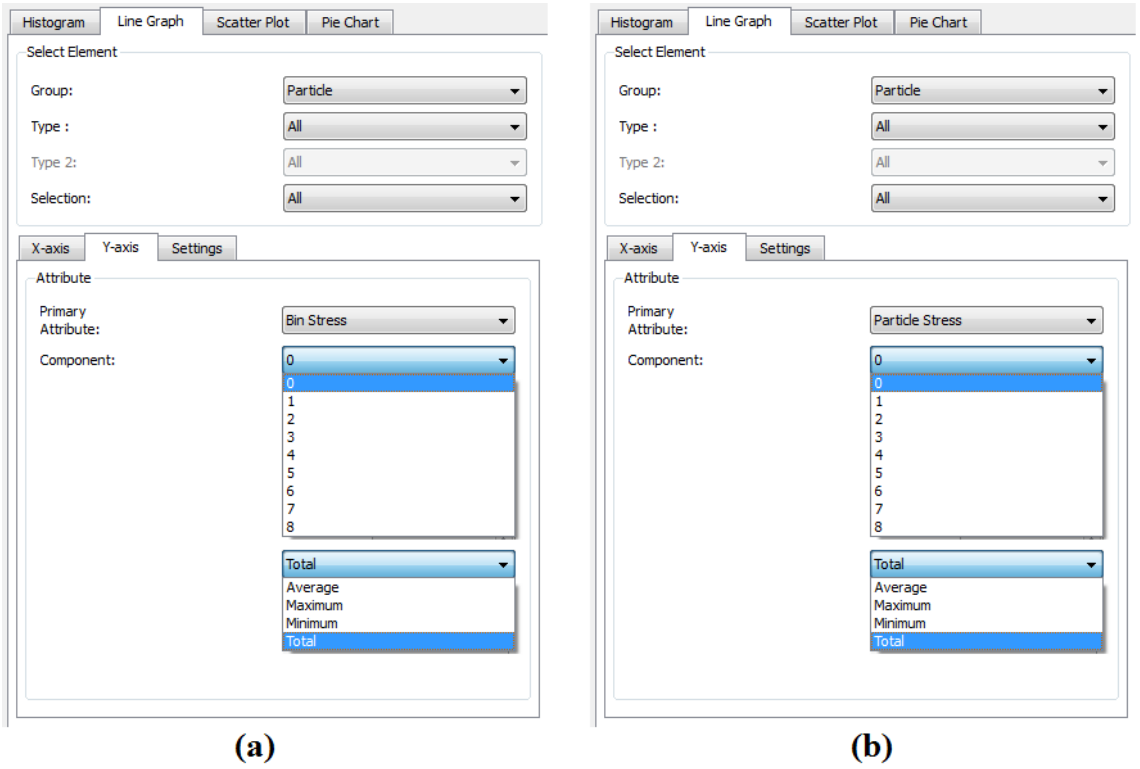

Figure A4.1: Data extraction from the two added attributes in EDEM® software: (a) Bin Stress, (b) Particle Stress